Università degli Studi di Modena e Reggio Emilia

PhD Programme in Clinical and Experimental Medicine

XXXV cycle

Electrolyte-Gated Organic Transistor-based Biosensors for Detection of Multiple Sclerosis Biomarkers in Plasma

Kateryna Solodka

Supervisor

Prof. Marcello Pinti

Coordinator

Prof. Marco Vinceti

“No thief, however skilful, can rob one of knowledge, and that is why knowledge is the best and safest treasure to acquire.”

L. Frank Baum

Abstract

Multiple sclerosis (MS) is a chronic progressive inflammatory demyelinating disorder of the central nervous system. Although the aetiology of MS is not fully understood yet, it is generally defined to be an autoimmune disease, where both genetic and environmental factors play a key role. The identification of reliable biomarkers and the development of assays for their quantification is currently an unmet need for the early and accurate diagnosis and monitoring of MS. Recently, electronic-based immunosensors, such as electrolyte-gated organic transistors (EGOTs), have emerged as a promising alternative platform for the ultra-sensitive and label-free detection of biological analytes. The intrinsic characteristics of these devices, such as high amplification or low cost of production, place them as the ideal candidates for point-of-care applications.

The aim of this thesis was to develop novel immunosensors exploiting different EGOT architectures for the detection of biomarkers of MS. In particular, two candidate MS biomarkers were investigated: neurofilament light chain (NF-L) and mitochondrial DNA (mtDNA). The EGOTs were endowed with biorecognition capability by functionalizing the gold gate electrode. Several functionalization strategies were investigated, i.e., the immobilization of the biorecognition element via cys-tagged protein-G, or through the formation of a self-assembled monolayer, exploring the biotin-avidin interaction. The functionalization strategies were further validated by cyclic voltammetry, surface plasmon resonance (SPR), fiber optic SPR, and surface plasmon-enhanced fluorescence.

In the first part of the thesis, an EGOT-based biosensor was developed for the detection of NF-L. The biosensor demonstrated to selectively detect NF-L in a buffered solution, with an estimated limit of detection of 30 fM. In the second part of the thesis, an EGOT-based biosensor was developed to monitor the hybridization of mtDNA, proving to recognize the complementary mtDNA strand in a wide dynamic range of concentrations, and successfully discriminate it from a non-complementary sequence. The last part of the thesis was focused on the development of EGOT-based biosensors for the detection of NF-L in plasma. The developed biosensor presented optimal operability, even in such a complex medium as plasma, and proved to selectively discriminate NF-L from other proteins present in plasma.

The rapid, selective, reproducible, and label-free response provided by the EGOT-based biosensors indicates their potential as a promising alternative strategy for the detection of MS biomarkers.

Riassunto

La sclerosi multipla (SM) è una malattia infiammatoria demielinizzante cronica progressiva del sistema nervoso centrale. La causa di questa patologia non è ancora chiara, anche se si presume un'origine autoimmune, dove la genetica e i fattori ambientali giocano un ruolo importante. Attualmente, l'identificazione di biomarcatori attendibili e lo sviluppo di tecniche per la loro quantificazione è di urgente bisogno per una pronta e accurata diagnosi e monitoraggio della SM. Gli immunosensori basati su elettronica organica, come i transistor organici modulati mediante elettrolita (EGOT), hanno recentemente preso piede come un'alternativa promettente per la rilevazione ultra-sensibile e *label-free* di analiti biologici. Le caratteristiche intrinseche di questi dispositivi, come alta amplificazione, biocompatibilità, e bassi costi di produzione, li rendono candidati ideali per applicazioni cliniche.

Lo scopo di questa tesi è lo sviluppo di immunosensori, basati su un'architettura EGOT, per la rilevazione di biomarcatori promettenti per la SM, come il neurofilamento *light chain* (NF-L) e il DNA mitocondriale (mtDNA). Con lo scopo di rendere capace l'EGOT di riconoscere selettivamente il target analitico, l'elettrodo gate di oro è stato usato come elemento sensibile. Diverse strategie fi funzionalizzazione sono state studiate, come l'immobilizzazione d'anticorpi specifici con orientamento controllato attraverso la proteina-G, o l'immobilizzazione sfruttando l'interazione biotina-avidina. Le strategie di funzionalizzazione sono state ottimizzate e validate mediante tecniche elettrochimiche e spettroscopiche.

Nella prima parte della tesi, è stato sviluppato un biosensore EGOT per la rilevazione di NF-L. Il biosensore ha dimostrato di rilevare selettivamente NF-L, anche in presenza di molecole potenzialmente interferenti, con un limite di rilevazione stimato di 30 fM. In aggiunta, un secondo biosensore EGOT è stato sviluppato per monitorare l'ibridizzazione dal mtDNA, dimostrando di riconoscere il filamento di mtDNA complementare presente nella soluzione in un ampio intervallo di concentrazioni, discriminandolo tra filamenti non complementari. L'ultima parte della tesi è basata nello sviluppo di biosensori EGOT per la rivelazione di NF-L in plasma. Il biosensore ha mostrato una ottima operabilità nel plasma e ha dimostrato di discriminare selettivamente molecole di NF-L tra altre proteine presenti nella soluzione.

In conclusione, la risposta rapida, selettiva, riproducibile, e *label-free*, dei biosensori EGOFET, indica il potenziale di questi dispositivi come una strategia alternativa promettente per la rivelazione di biomarcatori di SM.

Keywords

Organic electronics

Biosensor

Transistor

Multiple sclerosis

Biomarkers

Acknowledgements

I would like to express my deepest gratitude to many people for their help and support during my studies at UNIMORE; without them, the work carried out in this thesis would not have been possible.

To begin, I would like to sincerely thank my supervisor **Prof. Marcello Pinti**, for presenting me the opportunity of joining the BORGES Training Network for my PhD studies, and for his help and supervision during these past years. I am equally grateful to **Prof. Carlo Augusto Bortolotti,** for his continuous supervision, guidance and advice. I would like to thank as well **Prof. Fabio Biscarini**, for allowing me to join his research group at the *Laboratorio di Elettronica Organica* (LEO).

I am very grateful to all my colleagues from the **LEO laboratory**, especially to **Marcello**, **Matteo**, and **Alessandro**, for introducing me to the world of organic electronics and teaching me all the related skills, and for their insightful comments and scientific discussions; and to **Chiara**, for making me feel very welcome in Italy and in Sweden.

A special thanks to **Pamela**, who has been by my side since the very beginning of this journey, for being an amazing friend, and for all the adventures, laughs and good times spend together.

I wish to thank **Prof. Wolfgang Knoll** and **Prof. Jakub Dostálek**, from the Austrian Institute of Technology, and **Prof. Daniel Simon**, from the University of Linköping, for kindly hosting me during my secondments. Joining the BST and LOE groups was a wonderful experience, and I am very thankful to all the people who warmly welcomed me and guided me during those months.

To all my colleagues from the **BORGES** team, for all the fun and good moments shared together. To **Roger** and **Bernhard**, for being amazing hosts during my secondments, and to **Larissa**, for her friendship and the sailing lessons.

I would like also to thank **Anna De Gaetano**, for her kindness and guidance in the biological world.

I would like to extend my gratitude to **Chiara Cavazzoni**, for being extremely helpful with all the paperwork.

I am deeply grateful for having had the opportunity of being part of a **Marie Curie Skłodowska European Training Network**. I also wish to acknowledge **Prof. Anna Vittoria Mattioli** and the ***Istituto Nazionale per le Ricerche Cardiovasculari***, for the additional funding.

I am heartily thankful to all the wonderful people I met in Italy, especially to my good friends **Sofia**, **Tomás**, and **Manon**, for all the great times we shared, and for making Italy to feel like home.

To all my friends in Spain, and especially to **Desireé**, for her friendship and support, regardless the distance.

To my beloved **family**, and especially to my wonderful **mum** and **dad**, for their unconditional love and support, and for always believing in me.

Last, but not least, to **Giustino**, for being so caring and supportive, and for always being there for me.

Table of contents

Chapter 1.
Multiple sclerosis

In this chapter, a general description of the pathology of multiple sclerosis is provided. The characteristic features of the disease are detailed, including the epidemiology and presentation forms of the disease, as well as biomarkers and the gold standards for their detection.

1.1. Epidemiology and risk factors

Multiple sclerosis (MS) is a chronic inflammatory and neurodegenerative disorder of the central nervous system (CNS) characterized by progressive axonal demyelination[1]. The disease presents an increasing global incidence, with a reported estimation of 2.8 million people affected by the disease in 2020. The high prevalence of MS situates it as the major cause of non-traumatic neurologic disability in young adults[2]. The disease presents low incidence in childhood and elderhood, exhibiting the major incidence peak in the early adulthood, between 25 and 35 years[2]. MS is characterized by an unequal gender incidence, being more frequent in women than in men, with an approximate ratio of 3:1[3].

The frequency of the disease is unevenly distributed throughout the world, varying significantly among continents. The incidence is low in tropical and subtropical geographical areas, and gradually increases as the distance from the equator increases (Figure 1.1). The link between latitude and MS prevalence has been reported in several studies[4,5]. The basis of this peculiar distribution is not fully known; however, sunlight exposure is believed to have an important contribution: people living in countries at higher latitudes receive lower levels of sunlight, and therefore may present lower levels of vitamin D[4,5].

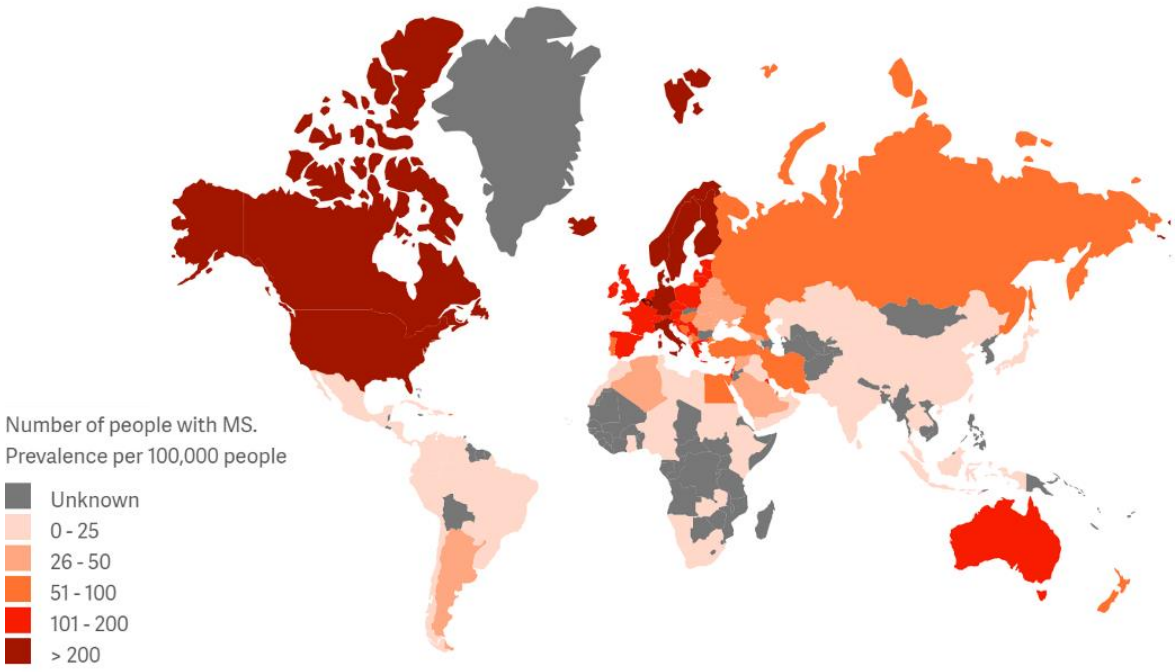

Figure 1.1. Worldwide distribution and prevalence of multiple sclerosis[2].

To date, the aetiology of MS remains unknown, although an autoimmune origin is well established. MS is a complex, multifactorial disease, where both genetic susceptibility and environmental factors play a key role for disease initiation. The risk of MS development is significantly higher in subjects with relatives affected by this pathology and shows a strong dependence on the degree of genetic proximity[6]. For identical twins, the risk of developing MS increases up to 25% if one twin is affected[7]. The first description of genetic risk factors dates back to the 1970s, when the association between MS and human leukocyte antigen alleles from the major histocompatibility complex was identified[8–11]. To date, more than 200 genetic risk variants have been identified[12]. However, the genetic risk alone cannot explain the geographical distribution of MS prevalence. In this regard, migration studies have revealed interesting findings: the risk of developing MS decreases in migrants who move from high- to low-risk areas, but does not increase among migrants from low- to high-risk, who tend to maintain the risk of the country of provenance. However, if the migration from a low- to a high-risk country occurs earlier in childhood, MS risk increases up to the same level of the host country[13,14]. These data suggest a strong correlation between the disease development and environmental triggers. Among these, Epstein-Barr virus seropositivity, infectious mononucleosis, and cigarette smoking, as well as low sunlight exposure and vitamin D deficiency, are well established risk factors for MS development[14–17].

1.2. Pathogenesis of multiple sclerosis, clinical presentation and disease course

The pathogenesis of MS is not completely understood. It is believed that the disease initiates with an increased migration of autoreactive lymphocytes across the blood brain barrier, generating an aberrant autoimmune response against CNS autoantigens[18]. However, the mechanisms by which these cells are activated and how they access the CNS remains elusive.

The pathological hallmark of MS consists in the formation of sclerotic plaques or lesions, disseminated throughout the white and grey matter within the brain, spinal cord, and optical nerves. The process of plaque formation involves inflammation, continuous demyelination and remyelination, oligodendrocyte depletion, astrocytosis, and neuronal and axonal degeneration[18–21]. Myelin has a protective role, acting like the insulating layer of an electric wire, the nerve. The loss of myelin (demyelination) results in a disruption of the electrical

signal, which derives in the typical MS symptoms: vision impairment, weak limbs, tingling sensations, dizziness, and weakness[22–24]. The progression of MS depends on the accumulated axonal loss. However, the mechanisms of progression are poorly understood, as the disease course vary significantly among patients, presenting periods of relapse and remission in some cases, or evolving to a chronic pattern in others[18].

Along the years, the definition of the different clinical courses of MS has been characterized by a lack of consensus among the clinical community. Therefore, for the purpose of clarity and consistency, and to improve the homogeneity of the clinical trials and the communication among clinicians and patients, a series of standardized definitions has been described by a committee of international MS experts. In this report, an accurate description of the different MS clinical courses provided[25]. Accordingly, MS disease course can be divided in four clinical patterns:

- *Clinically isolated syndrome (CIS).* CIS is defined as the first clinical demonstration of a disease presenting inflammatory demyelinating features that could be MS, but that have not completed yet other criteria to be recognized as MS. Patients with CIS usually experience monofocal symptoms, lasting for days or weeks[25,26].

- *Radiologically isolated syndrome (RIS).* RIS identifies patients presenting resonance imaging abnormalities, highly suggestive of demyelination, in the absence of clinical signs or symptoms[27]. Although RIS is not considered as a distinct MS subtype per se, since clinical evidence is lacking, its finding raises the awareness of MS[25].

- *Relapsing remitting MS (RRMS).* RRMS is the most common MS phenotype, found in about 85% of MS patients, and often preceded by the CIS phenotype. It is characterized by presenting episodes of neurological worsening (relapses), alternated with periods of variable recovery and clinical stability (remissions), with no apparent progression of the disease. The frequency of the relapsing phases is variable, but generally does not exceed 1.5 per year[28,29]. Over the years, many potential relapse triggers have been investigated, however, no specific factors have been identified yet. A correlation between infections with an increased relapse rate, prolonged relapse duration, and increased accumulation of disability has been reported[30,31]. Contrarily, a decrease in relapse rate has been observed during pregnancy, increasing after partum[32,33].

- *Secondary progressive MS (SPMS).* Following a RR course, after 10-15 years the disease course often evolves into a progressive pattern. To date, there is no specific criteria to define the conversion from the RR form to the SP stage. The transition to SPMS is described as a gradual process, and the diagnosis is generally established retrospectively[25,28].

- *Primary progressive MS (PPMS).* PPMS is characterized by the absence of an initial RR phase. The disease presents a progressive course, with a steady worsening of the neurological function from the onset[28]. Since 2013, PPMS is no longer considered as a MS phenotype, since increasing evidence suggests that the absence of a RR phase in PPMS patients is the result of clinically silent CNS lesions[25,34].

1.3. Diagnosis and biomarkers

The diagnosis of MS is challenging, due to the lack of a pathognomonic clinical marker or a diagnostic test. The high variability of MS, in terms of disease presentation and clinical course, is an additional difficulty for the diagnosis. Furthermore, some features of MS are common to other demyelinating disorders, increasing the probability of a misdiagnosis.

Currently, similarly to other neurological disorders, the diagnosis of MS relies mainly on the clinical history of the patient. Over the years, the McDonald criteria have been proposed as a guideline for the diagnosis of MS. According to the McDonald criteria, the key requirement for MS diagnosis is the demonstration of MS lesions, and their dissemination in time and space[35]. In other words, evidence of damage occurred at different dates (dissemination in time, DIT) and in different parts of the CNS (dissemination in space, DIS), must be provided. To date, the most extensive tool for the detection of MS lesions is magnetic resonance imaging (MRI)[36]. The use of brain and spinal cord MRI is recommendable in patients suspected of having MS, as it not only provides evidence of the presence of MS lesions, but can be also used to prove DIS and DIT[35,36].

In addition to the demonstration of MS lesions and their DIS and DIT, the differential diagnosis of MS requires the exclusion of other alternative diagnosis[35]. In this regard, the analysis of cerebrospinal fluid (CSF) is a valuable tool to support the diagnosis of MS[18,37]. Moreover, the evaluation of CSF markers of inflammation and neurodegeneration can provide additional

information regarding the inflammation and immunological status of the patient[37,38]. However, obtaining CSF samples (by lumbar puncture) is an invasive method, which cannot be employed for repeated routinary testing. Therefore, nowadays, the demonstration of MS biomarkers susceptible of being detected in blood is getting increasing attention, since blood samples are easily obtained and can be performed repeatedly. A selection of proposed MS biomarkers is described in the following section.

1.3.1. Oligoclonal IgG bands

The presence of oligoclonal IgG bands (OCB) in CSF, but not serum, together with an elevated IgG index, are features commonly found in MS patients. The presence of CSF OCB is an indication of increased intrathecal IgG synthesis, and it has been largely used as a diagnostic criterion for MS in the past[18,37]. Although to the current guidelines, the demonstration of CSF OCB is not a requirement for MS diagnosis, its presence is considered as evidence of DIT in the pathology. However, the presence of OCB in CSF is not specific for MS. OCB are considered to reflect the chronic activation of the immune system in the CNS, and therefore, can be found in a variety of other neurological disorders[39–41]. Therefore, the presence of CSF OCB should be interpreted carefully.

1.3.2. Markers of inflammation

Whether inflammation is the leading cause or a consequence in MS is still under debate, however, its contribution to the pathology is a well-known fact. Moreover, some of the immune cells infiltrating into the CNS are known to induce the secretion inflammatory cytokines and other regulators of inflammation. Therefore, the presence of inflammatory regulators in abnormal levels in the MS pathology is not surprising. In several studies, significantly higher levels of inflammatory cytokines have been reported, including interleukin (IL)-6, IL-8, IL-10, interferon-γ, and tumor necrosis factor[42,43]. The chemokine CXCL-13 has been largely investigated in MS, and increasing evidence highlights its potential as candidate biomarker of MS. Levels of CXCL-13 are significantly augmented in MS patients[43–45], correlating with the disease activity[46]. In addition, studies have reported a decrease in CXCL-13 levels in MS patients receiving therapy[47,48].

Nonetheless, no inflammatory molecule has been recognized as MS biomarker so far. However, although the reported molecules cannot be employed as markers specific for the MS pathology, their potential as biomarker relies on their use to monitor disease activity or therapy efficacy.

1.3.3. Neurofilament light chain

Neurofilaments (NFs) are structural scaffolding proteins, present exclusively in neurons[49,50]. NFs belong to the IV class of intermediate filaments and, together with microfilaments and microtubules, form the neural cytoskeleton, providing structural support to the cell[49,51]. According to the molecular weight, NFs are classified into three categories: neurofilament heavy chain (NF-H, ∼200 kDa), neurofilament medium chain (NF-M, ∼150 kDa), and neurofilament light chain (NF-L, ∼70 kDa)[49].

In the last years, NF-L has emerged as a potential candidate biomarker of MS[52–55]. Following situations accompanied by neural injury, NF-L are released in significant amounts into interstitial fluid, and eventually into the CSF and blood, providing an indication of the ongoing neuronal damage. Several studies have reported significantly higher levels of NF-L in both CSF and blood (serum or plasma) samples of MS patients[54–58]. NF-L levels were found as well to be correlated with the disease progression [55–58]and decrease following the treatment with disease-modifying therapies[53,55,59–61]. In addition, good correlation of NF-L levels was reported between CSF and blood-derived samples[55,56]. All these findings support the potential of NF-L as a promising biomarker of disease activity and disability progression in MS, as well as to monitor therapeutic efficacy.

The concentration levels of NF-L vary as a function of the investigated fluid, being present at higher concentrations in CSF and significantly lower in plasma and serum. In healthy subjects, the reported median levels of NF-L range between 10-30 pg/mL in plasma and serum, increasing up to 50 times in CSF[57,62]. In controls, NF-L levels are associated with age; higher NF-L concentrations have been observed in elderly population[57,63]. In MS, NF-L levels in plasma and serum are between 100-200 pg/mL[56,64], and higher than 1000 pg/mL in CSF[55,65].

1.3.4. Mitochondrial DNA

The implication of mitochondria in the activation of the immune response is a well-known fact, as, upon the degradation of the organelle, the release of mitochondrial products can trigger an innate immune response[66]. Among these, the own organelle genome, mitochondrial DNA (mtDNA) has been widely investigated as an alarm signal. mtDNA tends to persist in the extracellular fluids, as it seems to be more resistant to the degradation by nucleases than nuclear DNA[67].

Mitochondrial disfunction plays an important role in demyelination, and it has been associated with neuroinflammation and neurological disorders, such as Alzheimer's (AD) and Parkinson's disease (PD), and MS[68,69]. In recent studies, a significant decrease in circulating mtDNA levels in CSF of AD and PD patients was reported[70,71]. In contrast, in MS, increased levels of mtDNA have been reported in CSF[72], and plasma[42]. Based on this observation, mtDNA has been described as a damage-associated molecular pattern, in agreement with a scenario where inflammation is not the leading cause, but a consequence in MS[71]. This hypothesis would be in line with other studies, in which a decrease in mtDNA circulating levels in MS patients was observed upon treatment[72].

1.4. Detection of MS biomarkers

1.4.1. Magnetic resonance imaging

To date, the most widely used tool in MS diagnosis is based on imaging techniques for identification of demyelinating lesions. Since its development in the early 1980s, MRI became an essential tool in the diagnosis of MS. In fact, the current guidelines for MS diagnosis rely on MRI findings, integrated with clinical and laboratory analysis[35]. Although the histopathological examination is not possible in MS, MRI can be used to evaluate the extent of the CNS damage, as well as its dissemination. In addition, MRI allows the detection of lesions within the CNS suggestive of MS in subjects not presenting any symptomatology, and it is a valuable tool for monitoring disease activity and response to treatment[36].

However, although the value of MRI in MS is irrefutable, the technique presents important limitations. Despite the high sensitivity, MRI lacks specificity for MS. To overcome this problem, advanced MRI techniques have been developed. However, despite presenting

increased specificity and improving the diagnostic precision, these techniques are limited in widespread clinical usage due to technical issues[73]. The lack of standardized protocols for image acquisition and analysis represents and additional problem in MRI. Since the observed findings are strongly dependent on the acquisition parameters, there is an urgent need for standardization. Finally, it is important to mention that MRI requires extremely expensive and very specific instrumentation, which, despite being widely available in developed countries, is a limiting factor for its use in clinical practice in developing countries.

1.4.2. Electrophoresis

Electrophoretic-based assays of the CSF have largely employed for the detection of molecular biomarkers of MS. For instance, the recommended method for CSF OCB detection is isoelectric focusing, which will allow the separation of CSF proteins, followed by immunoblotting, used to separate IgG molecules[74]. The analysis of CSF should be performed in parallel to the examination of serum, and the obtained results in CSF have to be compared to serum. The interpretation of the results might be difficult, as different protein "patterns" have been described. In addition, the quality of the results strongly depends on the initial amount of protein loaded, and since over- or underloading may occur, standardization of protein amount to load is not recommendable. Therefore, an intrinsic calibration is recommended in every laboratory to ensure optimal results[75].

Immunoblotting has been used also for NF-L detection[76]. However, these first-generation immunoassays were semi-quantitative, and presented low sensitivity, which led to the development of more sensitivity assays.

1.4.3. Enzyme-linked immunosorbent assay

Enzyme-linked immunosorbent assays (ELISA) represent to date the gold standard detection method for many biological analytes. Since its development in the 1970s, ELISA has been routinely employed in clinical practice in a variety of different samples. The conventional ELISA assay consists of the detection of the analyte of interest in a sandwich-type assay. However, despite its many advantages, such as high sensitivity and specificity, ELISA presents certain limitations, as the need of two antibodies against the same target with different recognition epitopes, and labelling. In addition, the assay procedure is laborious and requires

specialized equipment. The sensitivity of the assay is strongly dependent on the analyte of interest; for instance, the sensitivity of ELISA for the detection of complexes as microRNAs is insufficient[77].

In MS, ELISA assays have been widely used for the analysis of CSF, serum, or plasma[43,46,48]. The second-generation assays for NF-L detection were based on ELISA and provided the first reliable quantitative data[50]. However, high inter-laboratory variability was reported, due to a lack of standardized ELISA protocols[78].

1.4.4. Electrochemiluminescence assay

The principle of electrochemiluminescence (ECL) assays relies on the generation of an electrochemically mediated chemiluminescent reaction. In an ECL-based immunoassay, the biorecognition element, e.g., the antibody, is labelled with an ECL specie, which will generate a detectable signal upon binding with the target molecule. ECL technology represents the third-generation assays for NF-L detection, and presents higher analytical sensitivity compared to ELISA[64,79].

1.4.5. Single molecule array

In the last years, single molecule arrays (SiMoA) have emerged as an ultra-sensitive platform for detection of biological markers. SiMoA, also known as digital ELISA, is based on the detection on single enzyme molecules, drastically increasing the sensitivity of the assay[80]. Compared to the conventional ELISA, SiMoA allows the possibility of detecting molecules at much lower concentrations, up to 10^{-15}M[80].

Recently, specific SiMoA kits for NF-L quantification have been developed, representing the fourth-generation assay. SiMoA technology presents extremely high sensitivity, being 126-fold and 25-fold more sensitive than ELISA and ECL assay, respectively[81]. The improvement in sensitivity allowed the accurate discrimination of NF-L levels in both, physiological and pathological, range of concentrations in blood samples[55,62].

Despite its extremely high sensitivity, SiMoA presents important disadvantages, strongly limiting its use for routinary testing. SiMoA technology is very expensive, requires dedicated

equipment with specialized training, and, so far, the number of proteins that can be analyzed with SiMoA is relatively low.

1.4.6. Polymerase chain reaction

Polymerase chain reaction (PCR) exploits the ability of DNA polymerase to synthesize new complementary DNA strands. This technique allows the exponential amplification of a target DNA sequence, by creating millions of new copies. PCR presents extremely high sensitivity, in the single molecule range, which allows the determination of rare sequences. Since its development in the 1980s, PCR revolutionized the field of clinical diagnosis. Nowadays, PCR is widely used for detection of bacteria difficult to cultivate and for the detection of human immunodeficiency virus, tuberculosis, or the recent COVID-19 virus, among others[82,83]. Additionally, PCR has been employed in MS for detection of mtDNA[42,72], as it is not possible with the previously mentioned techniques.

Nonetheless, PCR presents some limitations, as it can only be employed to study DNA or RNA sequences. The quality of the obtained results depends on the initial components, as small errors will be gradually propagated during the amplification. Another common problem in PCR is cross-contamination, as during the assay, any material containing DNA is susceptible to replication. Therefore, specific and isolated areas should be designated to perform the assay, and the contamination of the materials and equipment should be avoided at all costs.

1.5. Concluding remarks

Nowadays, standard methods for the detection of MS biomarkers are based on several of the above-mentioned techniques. Nonetheless, despite their many advantages, all these methods present a common limitation: they cannot be employed for routinary testing. Therefore, there is an unmet need for the development of fast, reliable, low-cost, and user-friendly methods for the detection of clinical markers of MS. The development of such technology would allow to perform routinary testing not limited to hospitals, but even at home. Especially, this would have a major impact in developing countries. Moreover, it would affect drastically the quality of life of MS patients, improving the monitoring of disease activity as well as treatment response.

1.6. References

1. Lassmann, H., Brück, W. & Lucchinetti, C. F. The Immunopathology of Multiple Sclerosis: An Overview. *Brain Pathology* **17**, 210–218 (2007).

2. Walton, C. *et al.* Rising prevalence of multiple sclerosis worldwide: Insights from the Atlas of MS, third edition. *Multiple Sclerosis Journal* **26**, 1816–1821 (2020).

3. Trojano, M. *et al.* Geographical Variations in Sex Ratio Trends over Time in Multiple Sclerosis. *PLoS One* **7**, e48078 (2012).

4. Tao, C. *et al.* Higher latitude is significantly associated with an earlier age of disease onset in multiple sclerosis. *J Neurol Neurosurg Psychiatry* **87**, 1343–1349 (2016).

5. Simpson, S. *et al.* Latitude continues to be significantly associated with the prevalence of multiple sclerosis: an updated meta-analysis. *J Neurol Neurosurg Psychiatry* **90**, 1193–1200 (2019).

6. Balcerac, A. & Louapre, C. Genetics and familial distribution of multiple sclerosis: A review. *Rev Neurol (Paris)* **178**, 512–520 (2022).

7. Fagnani, C. *et al.* Twin studies in multiple sclerosis: A meta-estimation of heritability and environmentality. *Multiple Sclerosis Journal* **21**, 1404–1413 (2015).

8. Jersild, C., Svejgaard, A. & Fog, T. HL-A antigens and multiple sclerosis. *Lancet* **1**, 1240–1 (1972).

9. Naito, S., Namerow, N., Mickey, M. R. & Terasaki, P. I. Multiple sclerosis: association with HL-A3. *Tissue Antigens* **2**, 1–4 (1972).

10. Compston, D. A., Batchelor, J. R. & McDonald, W. I. B-lymphocyte alloantigens associated with multiple sclerosis. *Lancet* **2**, 1261–5 (1976).

11. Terasaki, P. I., Park, M. S., Opelz, G. & Ting, A. Multiple sclerosis and high incidence of a B lymphocyte antigen. *Science* **193**, 1245–7 (1976).

12. Patsopoulos, N. A. Genetics of Multiple Sclerosis: An Overview and New Directions. *Cold Spring Harb Perspect Med* **8**, a028951 (2018).

13. Gale, C. R. & Martyn, C. N. Migrant studies in multiple sclerosis. *Prog Neurobiol* **47**, 425–448 (1995).

14. Ebers, G. C. Environmental factors and multiple sclerosis. *Lancet Neurol* **7**, 268–277 (2008).

15. Olsson, T., Barcellos, L. F. & Alfredsson, L. Interactions between genetic, lifestyle and environmental risk factors for multiple sclerosis. *Nat Rev Neurol* **13**, 25–36 (2017).

16. Tarlinton, R. E., Martynova, E., Rizvanov, A. A., Khaiboullina, S. & Verma, S. Role of Viruses in the Pathogenesis of Multiple Sclerosis. *Viruses* **12**, 643 (2020).

17. Marrodan, M., Alessandro, L., Farez, M. F. & Correale, J. The role of infections in multiple sclerosis. *Multiple Sclerosis Journal* **25**, 891–901 (2019).

18. Dendrou, C. A., Fugger, L. & Friese, M. A. Immunopathology of multiple sclerosis. *Nat Rev Immunol* **15**, 545–558 (2015).

19. Dutta, R. & Trapp, B. D. Pathogenesis of axonal and neuronal damage in multiple sclerosis. *Neurology* **68**, S22-31; discussion S43-54 (2007).

20. Correale, J., Gaitán, M. I., Ysrraelit, M. C. & Fiol, M. P. Progressive multiple sclerosis: from pathogenic mechanisms to treatment. *Brain* aww258 (2016) doi:10.1093/brain/aww258.

21. Lassmann, H. Multiple Sclerosis Pathology. *Cold Spring Harb Perspect Med* **8**, a028936 (2018).

22. Compston, A. & Coles, A. Multiple sclerosis. *The Lancet* **372**, 1502–1517 (2008).

23. Schapiro, R. T. Managing symptoms of multiple sclerosis. *Neurol Clin* **23**, 177–187 (2005).

24. Pagnini, F., Bosma, C. M., Phillips, D. & Langer, E. Symptom changes in multiple sclerosis following psychological interventions: a systematic review. *BMC Neurol* **14**, 222 (2014).

25. Lublin, F. D. *et al.* Defining the clinical course of multiple sclerosis: The 2013 revisions. *Neurology* **83**, 278–286 (2014).

26. Miller, D., Barkhof, F., Montalban, X., Thompson, A. & Filippi, M. Clinically isolated syndromes suggestive of multiple sclerosis, part I: natural history, pathogenesis, diagnosis, and prognosis. *Lancet Neurol* **4**, 281–288 (2005).

27. Okuda, D. T. *et al.* Incidental MRI anomalies suggestive of multiple sclerosis: The radiologically isolated syndrome. *Neurology* **72**, 800–805 (2009).

28. Klineova, S. & Lublin, F. D. Clinical Course of Multiple Sclerosis. *Cold Spring Harb Perspect Med* **8**, a028928 (2018).

29. Lublin, F. D. & Reingold, S. C. Defining the clinical course of multiple sclerosis: Results of an international survey. *Neurology* **46**, 907–911 (1996).

30. Andersen, O., Lygner, P. E., Bergström, T., Andersson, M. & Vablne, A. Viral infections trigger multiple sclerosis relapses: a prospective seroepidemiological study. *J Neurol* **240**, 417–422 (1993).

31. Tremlett, H. *et al.* Monthly Ambient Sunlight, Infections and Relapse Rates in Multiple Sclerosis. *Neuroepidemiology* **31**, 271–279 (2008).

32. Confavreux, C., Hutchinson, M., Hours, M. M., Cortinovis-Tourniaire, P. & Moreau, T. Rate of Pregnancy-Related Relapse in Multiple Sclerosis. *New England Journal of Medicine* **339**, 285–291 (1998).

33. Damek, D. M. & Shuster, E. A. Pregnancy and Multiple Sclerosis. *Mayo Clin Proc* **72**, 977–989 (1997).

34. Ransohoff, R. M., Hafler, D. A. & Lucchinetti, C. F. Multiple sclerosis—a quiet revolution. *Nat Rev Neurol* **11**, 134–142 (2015).

35. Thompson, A. J. *et al.* Diagnosis of multiple sclerosis: 2017 revisions of the McDonald criteria. *Lancet Neurol* **17**, 162–173 (2018).

36. Giorgio, A. & de Stefano, N. Effective Utilization of MRI in the Diagnosis and Management of Multiple Sclerosis. *Neurol Clin* **36**, 27–34 (2018).

37. Nylander, A. & Hafler, D. A. Multiple sclerosis. *Journal of Clinical Investigation* **122**, 1180–1188 (2012).

38. lo Sasso, B., Agnello, L., Bivona, G., Bellia, C. & Ciaccio, M. Cerebrospinal Fluid Analysis in Multiple Sclerosis Diagnosis: An Update. *Medicina (B Aires)* **55**, 245 (2019).

39. Ticozzi, N. *et al.* Oligoclonal bands in the cerebrospinal fluid of amyotrophic lateral sclerosis patients with disease-associated mutations. *J Neurol* **260**, 85–92 (2013).

40. Pannewitz-Makaj, K. *et al.* Evidence of Oligoclonal Bands Does Not Exclude Non-Inflammatory Neurological Diseases. *Diagnostics* **11**, 37 (2020).

41. Berek, K. *et al.* Cerebrospinal fluid oligoclonal bands in Neuroborreliosis are specific for Borrelia burgdorferi. *PLoS One* **15**, e0239453 (2020).

42. Nasi, M. *et al.* Increased plasma levels of mitochondrial DNA and pro-inflammatory cytokines in patients with progressive multiple sclerosis. *J Neuroimmunol* **338**, 577107 (2020).

43. Magliozzi, R. *et al.* Inflammatory intrathecal profiles and cortical damage in multiple sclerosis. *Ann Neurol* **83**, 739–755 (2018).

44. Krumbholz, M. *et al.* Chemokines in multiple sclerosis: CXCL12 and CXCL13 up-regulation is differentially linked to CNS immune cell recruitment. *Brain* **129**, 200–211 (2006).

45. Khademi, M. *et al.* Cerebrospinal fluid CXCL13 in multiple sclerosis: a suggestive prognostic marker for the disease course. *Multiple Sclerosis Journal* **17**, 335–343 (2011).

46. Khademi, M. *et al.* Cerebrospinal fluid CXCL13 in multiple sclerosis: a suggestive prognostic marker for the disease course. *Multiple Sclerosis Journal* **17**, 335–343 (2011).

47. Novakova, L. *et al.* Cerebrospinal fluid biomarkers as a measure of disease activity and treatment efficacy in relapsing-remitting multiple sclerosis. *J Neurochem* **141**, 296–304 (2017).

48. Novakova, L. *et al.* Cerebrospinal fluid biomarkers of inflammation and degeneration as measures of fingolimod efficacy in multiple sclerosis. *Multiple Sclerosis Journal* **23**, 62–71 (2017).

49. Yuan, A., Rao, M. v., Veeranna & Nixon, R. A. Neurofilaments and Neurofilament Proteins in Health and Disease. *Cold Spring Harb Perspect Biol* **9**, a018309 (2017).

50. Khalil, M. *et al.* Neurofilaments as biomarkers in neurological disorders. *Nat Rev Neurol* **14**, 577–589 (2018).

51. Liu, Q. *et al.* Neurofilament proteins in neurodegenerative diseases. *Cellular and Molecular Life Sciences* **61**, 3057–3075 (2004).

52. Varhaug, K. N., Torkildsen, Ø., Myhr, K.-M. & Vedeler, C. A. Neurofilament Light Chain as a Biomarker in Multiple Sclerosis. *Front Neurol* **10**, (2019).

53. Kuhle, J. *et al.* Blood neurofilament light chain as a biomarker of MS disease activity and treatment response. *Neurology* **92**, e1007–e1015 (2019).

54. Håkansson, I. *et al.* Neurofilament light chain in cerebrospinal fluid and prediction of disease activity in clinically isolated syndrome and relapsing-remitting multiple sclerosis. *Eur J Neurol* **24**, 703–712 (2017).

55. Disanto, G. *et al.* Serum Neurofilament light: A biomarker of neuronal damage in multiple sclerosis. *Ann Neurol* **81**, 857–870 (2017).

56. Håkansson, I. *et al.* Neurofilament levels, disease activity and brain volume during follow-up in multiple sclerosis. *J Neuroinflammation* **15**, 209 (2018).

57. Barro, C. *et al.* Serum neurofilament as a predictor of disease worsening and brain and spinal cord atrophy in multiple sclerosis. *Brain* **141**, 2382–2391 (2018).

58. Ferraro, D. *et al.* Plasma neurofilaments correlate with disability in progressive multiple sclerosis patients. *Acta Neurol Scand* **141**, 16–21 (2020).

59. Abdelhak, A. *et al.* Plasma neurofilament light chain levels suggest neuroaxonal stability following therapeutic remyelination in people with multiple sclerosis. *J Neurol Neurosurg Psychiatry* **93**, 972–977 (2022).

60. Novakova, L. *et al.* Monitoring disease activity in multiple sclerosis using serum neurofilament light protein. *Neurology* **89**, 2230–2237 (2017).

61. Varhaug, K. N. *et al.* Neurofilament light chain predicts disease activity in relapsing-remitting MS. *Neurology - Neuroimmunology Neuroinflammation* **5**, e422 (2018).

62. Gisslén, M. *et al.* Plasma Concentration of the Neurofilament Light Protein (NFL) is a Biomarker of CNS Injury in HIV Infection: A Cross-Sectional Study. *EBioMedicine* **3**, 135–140 (2016).

63. Khalil, M. *et al.* Serum neurofilament light levels in normal aging and their association with morphologic brain changes. *Nat Commun* **11**, 812 (2020).

64. Kuhle, J. *et al.* Serum neurofilament light chain is a biomarker of human spinal cord injury severity and outcome. *J Neurol Neurosurg Psychiatry* **86**, 273–9 (2015).

65. Kuhle, J. *et al.* A comparative study of CSF neurofilament light and heavy chain protein in MS. *Mult Scler* **19**, 1597–603 (2013).

66. De Gaetano, A. *et al.* Molecular Mechanisms of mtDNA-Mediated Inflammation. *Cells* **10**, 2898 (2021).

67. Tepper, C. G. & Studzinski, G. P. Resistance of mitochondrial DNA to degradation characterizes the apoptotic but not the necrotic mode of human leukemia cell death. *J Cell Biochem* **52**, 352–361 (1993).

68. Barcelos, I. P. de, Troxell, R. M. & Graves, J. S. Mitochondrial Dysfunction and Multiple Sclerosis. *Biology (Basel)* **8**, 37 (2019).

69. Mao, P. & Reddy, P. H. Is multiple sclerosis a mitochondrial disease? *Biochimica et Biophysica Acta (BBA) - Molecular Basis of Disease* **1802**, 66–79 (2010).

70. Podlesniy, P. *et al.* Low cerebrospinal fluid concentration of mitochondrial DNA in preclinical Alzheimer disease. *Ann Neurol* **74**, 655–668 (2013).

71. Pyle, A. *et al.* Reduced cerebrospinal fluid mitochondrial DNA is a biomarker for early-stage Parkinson's disease. *Ann Neurol* **78**, 1000–1004 (2015).

72. Varhaug, K. N. *et al.* Increased levels of cell-free mitochondrial DNA in the cerebrospinal fluid of patients with multiple sclerosis. *Mitochondrion* **34**, 32–35 (2017).

73. Hemond, C. C. & Bakshi, R. Magnetic Resonance Imaging in Multiple Sclerosis. *Cold Spring Harb Perspect Med* **8**, a028969 (2018).

74. Keir, G., Luxton, R. W. & Thompson, E. J. Isoelectric Focusing of Cerebrospinal Fluid Immunoglobulin G: An Annotated Update. *Annals of Clinical Biochemistry: International Journal of Laboratory Medicine* **27**, 436–443 (1990).

75. Link, H. & Huang, Y.-M. Oligoclonal bands in multiple sclerosis cerebrospinal fluid: An update on methodology and clinical usefulness. *J Neuroimmunol* **180**, 17–28 (2006).

76. Petzold, A. Neurofilament phosphoforms: Surrogate markers for axonal injury, degeneration and loss. *J Neurol Sci* **233**, 183–198 (2005).

77. Sakamoto, S. *et al.* Enzyme-linked immunosorbent assay for the quantitative/qualitative analysis of plant secondary metabolites. *J Nat Med* **72**, 32–42 (2018).

78. Petzold, A. *et al.* Neurofilament ELISA validation. *J Immunol Methods* **352**, 23–31 (2010).

79. Kuhle, J. *et al.* A highly sensitive electrochemiluminescence immunoassay for the neurofilament heavy chain protein. *J Neuroimmunol* **220**, 114–9 (2010).

80. Rissin, D. M. *et al.* Single-molecule enzyme-linked immunosorbent assay detects serum proteins at subfemtomolar concentrations. *Nat Biotechnol* **28**, 595–599 (2010).

81. Kuhle, J. *et al.* Comparison of three analytical platforms for quantification of the neurofilament light chain in blood samples: ELISA, electrochemiluminescence immunoassay and Simoa. *Clinical Chemistry and Laboratory Medicine (CCLM)* **54**, (2016).

82. Wages, J. M. POLYMERASE CHAIN REACTION. in *Encyclopedia of Analytical Science* 243–250 (Elsevier, 2005). doi:10.1016/B0-12-369397-7/00475-1.

83. Tahamtan, A. & Ardebili, A. Real-time RT-PCR in COVID-19 detection: issues affecting the results. *Expert Rev Mol Diagn* **20**, 453–454 (2020).

Chapter 2.
Biosensing with organic electronics

In this chapter, an introduction to organic electronics is presented, as well as its interfacing with the biological world. Organic electronic devices are introduced, and their working mechanism is described in detailed. Finally, the potential applications of these devices for biosensing purposes are described.

2.1. General introduction to biosensors

The need of cheap and reliable tests, able to provide a fast response, and that can be easily operated in the field employed (for example, for medical applications, at the doctor's office, or even at home), has led to the constantly rising development of novel biosensors. A biosensor can be defined as a device that, by incorporating a biological sensing element, is able to detect the presence of specific analytes, generating a measurable signal[1] (Figure 2.1).

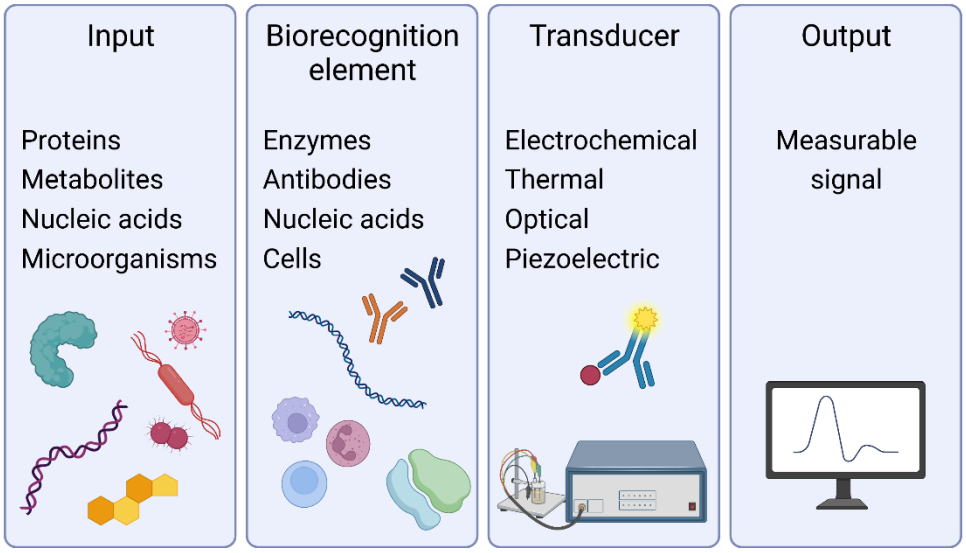

Figure 2.1. Schematic illustration of a biosensor. The analyte (input) is detected by the biorecognition element, and the resulting signal from this interaction is converted by the transducer into a measurable signal (output).

A typical biosensor is composed by the elements described in Figure 2.1: i) the input, which is the target analyte to detect and that can be represented by different molecules, including proteins, nucleic acids, metabolites, or microorganisms, ii) the biorecognition element, which is the molecule able to selective and specifically detect the analyte; it can be represented by an antibody, enzyme, oligonucleotide sequence, or even a cell, iii) the transducer, that allows the conversion of the signal resulting from the analyte-biorecognition element interaction into a measurable signal (e.g, optical, thermal, electrochemical, or piezoelectric), and iv) the output, which is the processed signal, and it can be measured in the form of light, voltage, or current, among others.

When designing a biosensor, several important features have to be taken into account: the biosensor has to present high selectivity towards the analyte of interest, being capable of detecting it even in a complex sample and in the presence of interfering molecules. The

biosensor should provide a stable and reproducible response for the same concentration of the analyte in different experiments. Moreover, the biosensor should be able to recognize the analyte in a relevant concentration range, i.e., the useful range for clinical use, providing an accurate discrimination between the physiological and pathological range.

Commonly, two types of biosensors can be distinguished, based on whether the signal resulting from the recognition event is directly transduced (direct, label-free detection sensors), or it is the result of the interaction with an additional element, e.g., enzymes or fluorescent tags (indirect, label-based detection sensors)[2]. As well, based on the transduction mechanisms, biosensors can be classified in different categories. Some of the most common transduction mechanisms are the following:

- *Optical.* Optical biosensors are the most established type biosensors. The detection relies on the light properties' changes upon the interaction of the analyte with the biorecognition element. Typical label-based optical biosensors are the fluorometric or colorimetric assays, while among the label-free, the more exploited optical biosensors are based on surface plasmon resonance (SPR)[3,4].

- *Electrochemical.* The principle of electrochemical biosensors relies on the transduction of a chemical signal, resulting from the biorecognition event, into an electrical signal. Commonly, electrochemical biosensors measure the variation in conductance, resistance, or capacitance at the biosensor surface induced by the biorecognition event[5,6].

- *Piezoelectric.* Piezoelectric biosensors detect the changes in resonant frequency of an oscillating piezoelectric crystal as a function of the mass on the surface, induced by the analyte-biorecognition element binding[2].

The first demonstration of a biosensor dates back to the second half of the twentieth century, when, in 1962, Clark and Lyons reported an electrochemical system for the monitoring of blood gas levels during cardiovascular surgery. Since then, the field of biosensing has experienced an enormous growth, and nowadays successful examples of biosensors can be found in glucometers, home pregnancy tests, or the recently developed[7] COVID-19 rapid antigen tests. The biosensing field is in continuous expansion, and the recent advances in material science

and device architecture have led to the development of biosensors for a large variety of applications, including healthcare and biomedical[8,9], agri-food[10,11], or environmental.

Currently, the development of biosensors for the biomedical field is receiving increasing attention. Under the present circumstances, with a continuous population growth and the increasing incidence of chronic pathologies together with the unpredicted outbreak of infectious disease, the availability of cheap, disposable, portable, and sensitive biosensors is of great interest[12,13].

2.2. Organic electronics

Organic electronics is an emerging multidisciplinary technology. The term "organic" refers to the exploitation of carbon-based conductive polymers and small molecules as active materials, defining in this way the fundamental difference between the "traditional" electronics, based silicon, germanium, or metal oxides. The birth of organic electronics dates back to the 19th century, with the novel investigations of Henry Letheby on the electrochemical oxidation of aniline to polyaniline[14]. But it was not until a century later when the major advances in the field were achieved. In 1977, Alan J. Heeger, Hideki Shirakawa and Alan G. MacDiarmid reported the development of conductive organic polymers with a controlled doping process[15], a discovery for which the researchers were awarded with the Nobel Prize in Chemistry in 2000. This finding opened up a world of new possibilities, as until then, polymers were exclusively used as insulating materials. The development of conductive polymers and their application as active material resulted in a revolution in the field of organic electronics. The intrinsic properties of conductive polymers, such as the solubility in common solvents and the tunability to meet specific requirements, have opened the way towards the production of large-area, printable, and low-cost electronics. Nowadays, successful examples of organic electronic-based devices can be found in organic field-effect transistors (OFETs)[16], organic heterojunction photovoltaic cells (OPVs)[17], or organic light-emitting diodes (OLEDs)[18].

Currently, the research of conductive polymers is evolving towards the integration of this technology in industry, and, although it might never meet the conventional electronics, in terms of performance, its real potential resides in the possibility of developing cheaper, robust, disposable, flexible, and disposable devices.

2.3. Organic bioelectronics

The merging of electronics and the biological world began in the 18th century with the novel investigations of Luigi Galvani on animal electrophysiology. Since then, the application of electronics for bio-related purposes has been largely exploited, resulting in the development of electronic implants, e.g., pacemakers or cochlear implants, drug-releasing devices, or biosensors[19,20]. However, the nature of the materials employed in "traditional" electronics present strong limitations when aiming at being interfaced with the biological world. In this regard, organic electronic materials are the ideal candidates for interfacing electronics with biological systems. With respect the main advantages of organic electronic materials, it is worth noting their mixed conductivity, as they are capable of conduct not only electronic but also ionic charges[21,22]. This mixed conductivity has been widely exploited for interfacing organic electronics with the biological world, as it allows the transduction of biological (ionic) signals into electrical ones, and vice versa[23]. In addition, the versatility of the organic electronic materials permits their modification by tailored design and synthesis to meet the desirable characteristics, allowing the creation of flexible, elastic, and biocompatible devices.

In the last years, the improvements in the synthesis and design of organic semiconductors have led to enormous advances in the field of organic bioelectronics. In this regard, a wide variety of applications of organic electronic-based devices has been reported, including biosensing, electrophysiology and neuromodulation, wearable electronics, and even plant and bacteria interfacing[24–30].

2.4. Electrolyte-gated organic transistors

One of the new potential applications of organic electronics devices is biosensing. Since the first description of a field-effect transistor operated in a liquid environment, commonly known as electrolyte-gated organic transistor (EGOT), there has been an increasing interest on the application of these devices for biosensing purposes. The operation of these transistors in water confers them with high amplification, which opens the possibility of using EGOT-based devices as a promising biosensing platform.

Commonly, EGOTs are classified in two categories, depending on whether the active layer is permeable or not to the electrolyte ions. Thus, electrochemical organic transistors (OECTs),

employing a permeable organic semiconductor (OSC), and electrolyte-gated organic field-effect transistors (EGOFETs), where no ion penetration into the organic material occurs, can be distinguished[31,32]. The use of polymers and aromatic and conjugated molecules as OSC have been widely explored for EGOT fabrication[33,34]. Among these, probably the most widely material used for OECT fabrication is the polymer PEDOT:PSS, while small molecules, such as pentacene and its derivatives or diF-TES-ADT, and polymers such as P3HT or pBTTT-C14, are commonly employed for EGOFET fabrication[30,35–37]. In EGOFETs, the interaction of the OSC with the ions present in the electrolyte is limited to a single interface. Contrary, in OECTs, the hydrated ions can enter inside the OSC, creating a volumetric capacitance dependent on the thickness of the OSC film[30,33].

2.4.1. Fundamental principles of device operation

An electrolyte-gated organic transistor is a three-terminal device, comprising gate, source, and drain electrodes. Source and drain electrodes are connected by an OSC film that acts as the channel, and is separated from the gate electrode by an electrolyte. Typically, drain and gate voltages are applied relative to the source electrode, which is kept grounded ($V_S = 0$). Upon the application of a negative (positive) potential difference between gate and source electrodes (V_{GS}), cations (anions) present in the electrolyte will move and accumulate at the gate/electrolyte interface, while anions (cations) will accumulate at the electrolyte/OSC interface. In order to compensate for the negative charge at the gate/electrolyte interface, the free charge carriers present in the OSC will be pushed towards the electrolyte/OSC interface, promoting the formation of an electrical double layer (EDL) at both interfaces. The injection of charge carriers into the electrolyte/OSC interface results in the formation of a conducting channel, which, upon the application of a second potential difference, between drain and source electrodes (V_{DS}), will result in a current flow (I_{DS}). The EDL formation results in a large capacitance (tens of $\mu F/cm^2$), which allows to operate at very low voltages (< 1 V)[38–41].

Two kinds of charge carriers can be distinguished for organic semiconductors: electrons, with a negative charge, and holes, with a positive charge. Depending on whether the charge carriers are electrons or holes, the OSC is known as *p* or *n* type, respectively.

2.4.2. Transfer and output characteristics

The current-voltage (*I-V*) characteristics of OFETs are generally classified as transfer characteristics, where the I_{DS} is measured as a function of V_{GS} at a fixed V_{DS} (I_{DS} vs. V_{GS}), and output characteristics, where the I_{DS} is recorded by sweeping the V_{DS} at different V_{GS} (V_{GS} vs. V_{DS}). Representative transfer and output characteristics of a *p*-type device are illustrated in Figure 2.2.

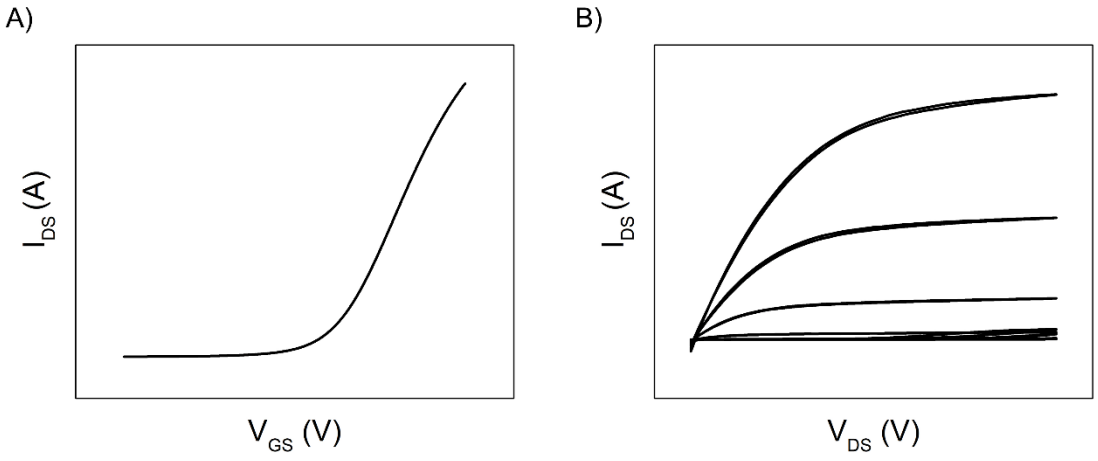

Figure 2.2. Current-voltage characteristics of an OFET, illustrating a transfer (A) and output (B) curves.

Two different operational regimes can be distinguished in (organic) field-effect transistors. Each regime is characterized by an equation relating the drain-source current to different parameters:

Linear regime:

$$I_{DS} = \frac{W}{L} C_i \mu \left(V_{GS} - V_{th} - \frac{V_{DS}}{2} \right) V_{DS} \qquad for\ V_{DS} < V_{GS} - V_{th} \qquad \textit{(Eq. 2.1)}$$

Saturation regime:

$$I_{DS} = \frac{W}{2L} C_i \mu (V_{GS} - V_{th})^2 \qquad for\ V_{DS} > V_{GS} - V_{th} \qquad \textit{(Eq. 2.2)}$$

where W is the channel width and L the channel length, C_i is the capacitance per unit area of the dielectric, V_{th} is the threshold voltage, defined as the minimum gate potential required to form a conductive channel, and μ is the field-effect mobility of the charge carriers.

In the linear regime (Figure 2.3, panel A), when a small V_{DS} potential is applied ($V_{DS} << V_{GS} - V_{th}$), the current increases proportionally to the increase in V_{DS}. This increase in I_{DS} with increasing V_{DS} is linear until reaching $V_{DS} = V_{GS} - V_{th}$. At this point, known as pinch-off (Figure 2.3, panel B), the channel begins to deplete, and a further increase in V_{DS} will not result in an increase in I_{DS}. This operational mode, when $V_{DS} > V_{GS} - V_{th}$, is known as saturation regime (Figure 2.3, panel C).

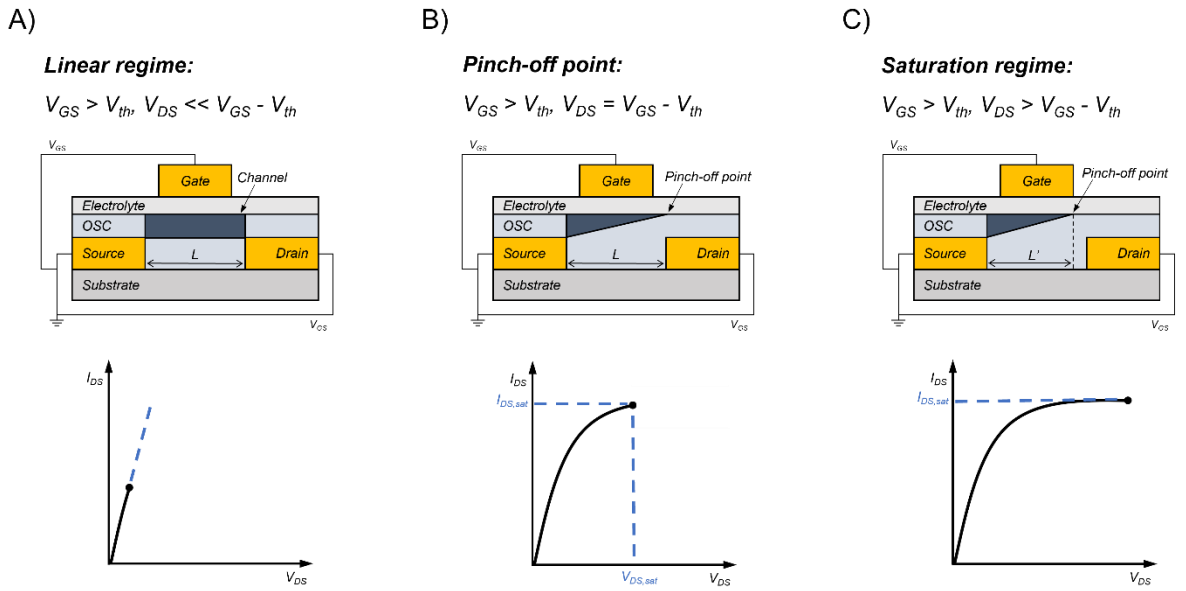

Figure 2.3. Illustration of the different operating regimes of an EGOT, with the corresponding *I-V* characteristics: linear regime (A), pinch-off point (B), and saturation regime (C).

2.4.3. Assessment of the device performance

In order to evaluate the electrical performance of OFETs, several figures of merit can be extracted from the transfer curves:

- *Transconductance (g_m).* The transconductance describes the variation of the drain current with respect to the gate voltage, and is a reflection of the capability of the gate to modulate the channel current. Thereby, a device with high transconductance is more sensible to small changes in the gate voltage. Transconductance is expressed in Siemens (S), and it can be extracted from the slope of the linear part of the transfer curve, or as the first derivative of the drain current with respect to the gate voltage (Figure 2.4).

$$g_m = \frac{\delta I_{DS}}{\delta V_{GS}} \qquad \textit{(Eq. 2.3)}$$

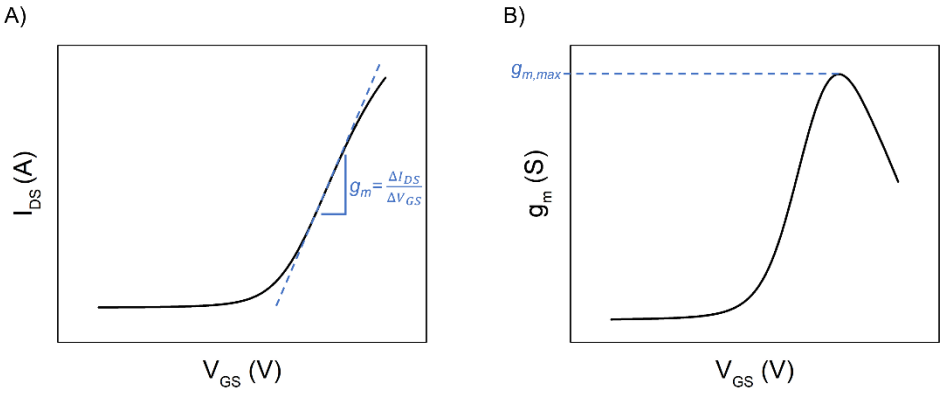

Figure 2.4. Extraction of the transconductance by calculating the slope of the linear part of the transfer curve (A), or by the first derivative of the transfer curve (B).

- *Threshold voltage (V_{th}).* The threshold voltage is defined as the gate voltage at which the charge accumulation begins, and therefore, at which the current begins to flow. The calculation of the threshold voltage can be complicated, since there is no one universal method. The most common method for V_{th} extraction, probably, is the extrapolation from the linear part of the transfer curve to the intercept of the V_{GS} axis. However, this method is subjected to variability, which stems from the identification of the linear region of the transfer curve, that is prone to error (Figure 2.5, panel A). In a second approach, V_{th} can be extracted by plotting the second derivative of the transfer curve (Figure 2.5, panel B).

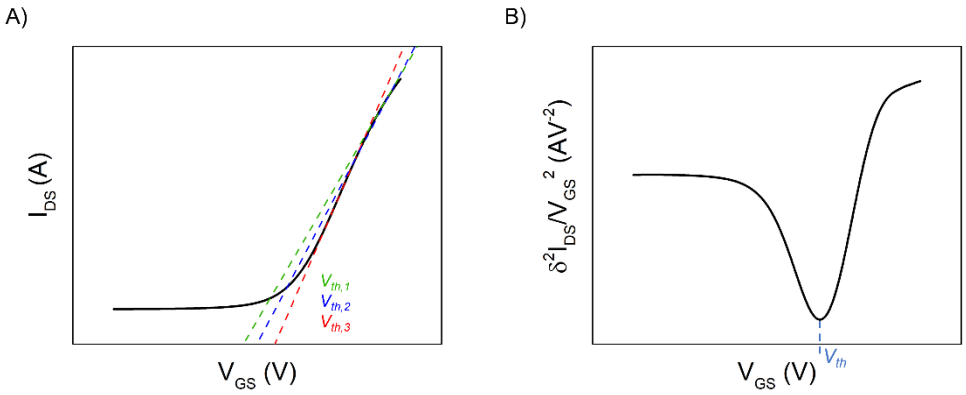

Figure 2.5. Extraction of the threshold voltage by extrapolation of the linear part of the transfer curve (A), or by the second derivative of the transfer curve (B).

- *On/off current ratio (I_{on}/I_{off}).* The *on/off* current ratio is a parameter that shows how effectively the device is turned into an *on* or *off* state, and is calculated as the I_{DS} at a

certain V_{GS} (*on* state) divided by the I_{DS} when the device is in the *off* state. The *on/off* ratio is influenced by the gate leakage current (I_{GS}) and the organic semiconductor material. A high *on/off* ratio is preferable.

- *Hysteresis.* Hysteresis is defined as the variation of the measured I_{DS} between the forward and backward scans. This phenomenon is caused by several factors, being the semiconductor charge trapping one of the most common. Semiconductor traps, which can increase or decrease the output current, leading to an erroneous parameter extraction. In OFETs, hysteresis should be as little as possible[42,43].

2.5. Electrolyte-gated organic transistor-based biosensors

The intrinsic amplification capability of EGOTs, combined with the operability in liquid environments, makes them an attractive platform for biosensing applications. Since the first demonstration of an organic field-effect transistor in water in 2010, the research around this topic has been in continuous expansion[44]. The versatility of these devices allows the modification of one of the relevant device interfaces, i.e., the gate electrode or the conductive material, allowing for the immobilization of specific recognition elements, turning the device into a sensor. Upon the exposition of the device to a sample containing the target analyte, the recognition events will generate a measurable signal. The capability of operating EGOTs in water opens up to the possibility of employing these devices directly in biological samples, such as blood, saliva, or sweat, allowing the fast and label-free detection of target analytes. Moreover, the high capacitance achieved when the device is exposed to a liquid environment allows its operation at very low voltages (< 1 V), which is a critical requirement when working with biological molecules.

2.5.1. Functionalization strategies

The functionalization of the gate electrode is, probably, the most widely used approach in the fabrication of EGOT-based biosensors[45–48]. Although the functionalization of the OSC has been exploited as well[49–54], and even the use of modified electrolytes, serving as the sensing part of the device, has been reported[55–57].

The election of the recognition element is critical, and is determined by the target analyte to be detected, being the most common one antibodies, aptamers, enzymes, or nucleic acids. Several strategies for the anchoring of the biorecognition element on the interface of interest have been investigated, exploiting physical adsorption, covalent binding, or bioaffinity coupling. Physical adsorption consists of the direct deposition of the biorecognition element, e.g., antibody, on the relevant interface surface. This approach has been successfully employed in several studies[52,58,59]. Covalent immobilization is generally achieved using self-assembled (SAM) monolayers. Usually, carboxyl (amino) groups are present at the SAM extremes, driving the coupling to the amino (carboxyl) groups of the biorecognition element. The formation of SAM on the surface not only promotes the immobilization of the biorecognition element, with a controlled density, but also serves as an antifouling agent to avoid non-specific adsorption of interfering elements[60]. Several studies have reported the successful development of EGOT-based biosensors by exploiting the SAM-mediated immobilization of the biorecognition element[46,61,62]. The immobilization of antibodies mediated by protein G is a common example of bioaffinity coupling. In this approach, the high affinity of protein G towards the fragment crystallizable (Fc) region of the immunoglobulins is exploited to immobilize the antibody on the surface. The use of protein G-mediated immobilization has been widely employed with the aim of controlling the orientation of the immobilized antibody[63–67]. Another common approach for bioaffinity coupling exploits biotin-streptavidin interactions. A biotin molecule can be easily attached to the biorecognition element, promoting its immobilization on a streptavidin layer present in the interface surface[68,69].

2.5.2. Device architecture

EGOTs can be fabricated exploiting different configurations, based on the position of the gate electrode with respect to the OSC channel. The most common architecture in EGOT-based biosensors is the top-gated geometry, where the gate is positioned directly over the channel. In this architecture, the gate and the OSC are connected by the electrolyte, which generally is a buffer solution containing the analyte of interest[45,49,62]. Moreover, in recent studies the use of a biological sample, such as serum, saliva, or sweat, as the electrolyte has been reported[47,53,54,70]. Other, less common, EGOT geometries, include the bottom-gated[71], where the gate is separated from the OSC by an ion-conducting membrane, or the side-gated geometry[72–74], in which both the gate and the channel rely in the same plane. An alternative EGOT architecture is the extended or floating gate geometry. This geometry is characterized

by the presence of an additional gate (sensing gate), that is in contact with the electrolyte containing the target analyte, and is electronically connected, but physically separated, to the transistor. The main advantage of this architecture is that the investigated sample is not in contact with the OSC. This platform has been widely employed for biosensing applications[75–77].

Currently, there is an increasing interest in the development of EGOT-based biosensing platforms incorporating a microfluidic system. The use of a microfluidic system offers the possibility of using very small samples quantities, which is of great interest when working with biological samples. Moreover, it is an additional mechanism to avoid non-specific adsorption. In recent years, several successful microfluidic EGOT-based biosensors have been developed for the detection of glucose[78], markers of inflammation[79] or neurodegeneration[80,81], or monitoring of DNA hybridization[82].

2.5.3. EGOT-based biosensors for clinical applications

In the last years, the development of EGOT-based biosensors for the detection of pathology-relevant markers has been widely exploited. Biosensor using an EGOT architecture have been reported for a wide variety of target molecules, including chemicals[48], proteins[45,46,62,83], metabolites[53,72,84], nucleic acids[74,85], and even antibodies[67] and virus[64,86].

Nowadays, thanks to the advances achieved in the development of EGOT-based biosensors, ultra-sensitive platforms, with very low limits of detection (LOD) have been reported. In several works reported by our group, the detection of inflammatory[79,87] and cancer[61] markers with a LOD in the low pM range was demonstrated. In a recent work, the development of an EGOT-based biosensor for detecting anti-drug antibodies was reported. The biosensor presented a LOD as low as 100 fM, much lower than the currently available technologies[67]. The detection in the pM range is optimal for markers that under pathological conditions reach extremely high concentration levels, such as inflammatory markers. However, this sensitivity might not be enough when aiming for the detection of analytes with a narrow concentration range and that, even in pathological conditions, are present at very low concentrations, such as markers of neurodegeneration. In this regard, it is worth mentioning the notable advances in the field of single molecule detection. The pioneer works reported by Luisa Torsi's group demonstrated the development of ultra-sensitive EGOT-based biosensors, or SiMoT (single molecule transistor), with a LOD in the zM range[88,89]. In the reported platform, the ultra-high

sensitivity is achieved by incorporating a large-area capturing interface, which allows the detection in the range of one single molecule within few minutes[88,90]. Furthermore, the developed biosensors proved to successfully detect the target analytes with the same sensitivity even in biological fluids[91,92].

2.6. References

1. Bhalla, N., Jolly, P., Formisano, N. & Estrela, P. Introduction to biosensors. *Essays Biochem* **60**, 1–8 (2016).

2. Rasooly, A. & Prickril, B. Biosensor Technologies. in *Biosensors and Biodetection* vol. 1571 (2017).

3. Estevez, M.-C., Otte, M. A., Sepulveda, B. & Lechuga, L. M. Trends and challenges of refractometric nanoplasmonic biosensors: A review. *Anal Chim Acta* **806**, 55–73 (2014).

4. Damborský, P., Švitel, J. & Katrlík, J. Optical biosensors. *Essays Biochem* **60**, 91–100 (2016).

5. Ronkainen, N. J., Halsall, H. B. & Heineman, W. R. Electrochemical biosensors. *Chem Soc Rev* **39**, 1747 (2010).

6. Abdulbari, H. A. & Basheer, E. A. M. Electrochemical Biosensors: Electrode Development, Materials, Design, and Fabrication. *ChemBioEng Reviews* **4**, 92–105 (2017).

7. Clark, L. C. & Lyons, C. ELECTRODE SYSTEMS FOR CONTINUOUS MONITORING IN CARDIOVASCULAR SURGERY. *Ann N Y Acad Sci* **102**, 29–45 (2006).

8. Naresh, Varnakavi. & Lee, N. A Review on Biosensors and Recent Development of Nanostructured Materials-Enabled Biosensors. *Sensors* **21**, 1109 (2021).

9. Mohankumar, P., Ajayan, J., Mohanraj, T. & Yasodharan, R. Recent developments in biosensors for healthcare and biomedical applications: A review. *Measurement* **167**, 108293 (2021).

10. Lu, Y., Yang, Q. & Wu, J. Recent advances in biosensor-integrated enrichment methods for preconcentrating and detecting the low-abundant analytes in agriculture and food samples. *TrAC Trends in Analytical Chemistry* **128**, 115914 (2020).

11. Griesche, C. & Baeumner, A. J. Biosensors to support sustainable agriculture and food safety. *TrAC Trends in Analytical Chemistry* **128**, 115906 (2020).

12. Karthik, V., Karuna, B., Kumar, P. S., Saravanan, A. & Hemavathy, R. V. Development of lab-on-chip biosensor for the detection of toxic heavy metals: A review. *Chemosphere* **299**, 134427 (2022).

13. Justino, C., Duarte, A. & Rocha-Santos, T. Recent Progress in Biosensors for Environmental Monitoring: A Review. *Sensors* **17**, 2918 (2017).

14. Letheby, H. XXIX.—On the production of a blue substance by the electrolysis of sulphate of aniline. *J. Chem. Soc.* **15**, 161–163 (1862).

15. Chiang, C. K. *et al.* Electrical Conductivity in Doped Polyacetylene. *Phys Rev Lett* **39**, 1098–1101 (1977).

16. Yun, M. *et al.* Stable Organic Field-Effect Transistors for Continuous and Nondestructive Sensing of Chemical and Biologically Relevant Molecules in Aqueous Environment. *ACS Appl Mater Interfaces* **6**, 1616–1622 (2014).

17. Kippelen, B. & Brédas, J.-L. Organic photovoltaics. *Energy Environ Sci* **2**, 251 (2009).

18. Shinar, J. & Shinar, R. Organic light-emitting devices (OLEDs) and OLED-based chemical and biological sensors: an overview. *J Phys D Appl Phys* **41**, 133001 (2008).

19. Joung, Y.-H. Development of Implantable Medical Devices: From an Engineering Perspective. *Int Neurourol J* **17**, 98 (2013).

20. Birmingham, K. *et al.* Bioelectronic medicines: a research roadmap. *Nat Rev Drug Discov* **13**, 399–400 (2014).

21. Rivnay, J., Owens, R. M. & Malliaras, G. G. The Rise of Organic Bioelectronics. *Chemistry of Materials* **26**, 679–685 (2014).

22. Simon, D. T., Gabrielsson, E. O., Tybrandt, K. & Berggren, M. Organic Bioelectronics: Bridging the Signaling Gap between Biology and Technology. *Chem Rev* **116**, 13009–13041 (2016).

23. Ohayon, D. & Inal, S. Organic Bioelectronics: From Functional Materials to Next-Generation Devices and Power Sources. *Advanced Materials* 2001439 (2020) doi:10.1002/adma.202001439.

24. Koklu, A. *et al.* Organic Bioelectronic Devices for Metabolite Sensing. *Chem Rev* **122**, 4581–4635 (2022).

25. Berggren, M., Głowacki, E. D., Simon, D. T., Stavrinidou, E. & Tybrandt, K. *In Vivo* Organic Bioelectronics for Neuromodulation. *Chem Rev* **122**, 4826–4846 (2022).

26. Pitsalidis, C. *et al.* Organic Bioelectronics for *In Vitro* Systems. *Chem Rev* **122**, 4700–4790 (2022).

27. Dufil, G., Bernacka-Wojcik, I., Armada-Moreira, A. & Stavrinidou, E. Plant Bioelectronics and Biohybrids: The Growing Contribution of Organic Electronic and Carbon-Based Materials. *Chem Rev* **122**, 4847–4883 (2022).

28. McCuskey, S. R. *et al.* Current Progress of Interfacing Organic Semiconducting Materials with Bacteria. *Chem Rev* **122**, 4791–4825 (2022).

29. Someya, T. & Amagai, M. Toward a new generation of smart skins. *Nat Biotechnol* **37**, 382–388 (2019).

30. Torricelli, F. *et al.* Electrolyte-gated transistors for enhanced performance bioelectronics. *Nature Reviews Methods Primers* **1**, 66 (2021).

31. Kim, S. H. *et al.* Electrolyte-Gated Transistors for Organic and Printed Electronics. *Advanced Materials* **25**, 1822–1846 (2013).

32. Rivnay, J. *et al.* Organic electrochemical transistors. *Nat Rev Mater* **3**, 17086 (2018).

33. Inal, S., Rivnay, J., Suiu, A.-O., Malliaras, G. G. & McCulloch, I. Conjugated Polymers in Bioelectronics. *Acc Chem Res* **51**, 1368–1376 (2018).

34. Kousseff, C. J., Halaksa, R., Parr, Z. S. & Nielsen, C. B. Mixed Ionic and Electronic Conduction in Small-Molecule Semiconductors. *Chem Rev* **122**, 4397–4419 (2022).

35. Riera-Galindo, S., Leonardi, F., Pfattner, R. & Mas-Torrent, M. Organic Semiconductor/Polymer Blend Films for Organic Field-Effect Transistors. *Adv Mater Technol* **4**, 1900104 (2019).

36. Wang, J., Ye, D., Meng, Q., Di, C. & Zhu, D. Advances in Organic Transistor-Based Biosensors. *Adv Mater Technol* **5**, 2000218 (2020).

37. Wang, D., Noël, V. & Piro, B. Electrolytic Gated Organic Field-Effect Transistors for Application in Biosensors—A Review. *Electronics (Basel)* **5**, 9 (2016).

38. Horowitz, G. Organic Field-Effect Transistors. *Advanced Materials* **10**, 365–377 (1998).

39. Kergoat, L., Piro, B., Berggren, M., Horowitz, G. & Pham, M.-C. Advances in organic transistor-based biosensors: from organic electrochemical transistors to electrolyte-gated organic field-effect transistors. *Anal Bioanal Chem* **402**, 1813–1826 (2012).

40. Cramer, T. *et al.* Double layer capacitance measured by organic field effect transistor operated in water. *Appl Phys Lett* **100**, 143302 (2012).

41. Melzer, K. *et al.* Characterization and simulation of electrolyte-gated organic field-effect transistors. *Faraday Discuss.* **174**, 399–411 (2014).

42. Kim, S., Yoo, H. & Choi, J. Effects of Charge Traps on Hysteresis in Organic Field-Effect Transistors and Their Charge Trap Cause Analysis through Causal Inference Techniques. *Sensors* **23**, 2265 (2023).

43. Paasch, G., Scheinert, S., Herasimovich, A., Hörselmann, I. & Lindner, Th. Characteristics and mechanisms of hysteresis in polymer field-effect transistors. *physica status solidi (a)* **205**, 534–548 (2008).

44. Kergoat, L. *et al.* A Water-Gate Organic Field-Effect Transistor. *Advanced Materials* **22**, 2565–2569 (2010).

45. Sailapu, S. K. *et al.* Standalone operation of an EGOFET for ultra-sensitive detection of HIV. *Biosens Bioelectron* **156**, 112103 (2020).

46. Macchia, E. *et al.* Ultra-sensitive protein detection with organic electrochemical transistors printed on plastic substrates. *Flexible and Printed Electronics* **3**, 034002 (2018).

47. Chen, L., Wang, N., Wu, J., Yan, F. & Ju, H. Organic electrochemical transistor for sensing of sialic acid in serum samples. *Anal Chim Acta* **1128**, 231–237 (2020).

48. Nguyen, T. T. K. *et al.* Triggering the Electrolyte-Gated Organic Field-Effect Transistor output characteristics through gate functionalization using diazonium chemistry: Application to biodetection of 2,4-dichlorophenoxyacetic acid. *Biosens Bioelectron* **113**, 32–38 (2018).

49. Pappa, A. M. *et al.* Direct metabolite detection with an n-type accumulation mode organic electrochemical transistor. *Sci Adv* **4**, (2018).

50. Buth, F., Donner, A., Sachsenhauser, M., Stutzmann, M. & Garrido, J. A. Biofunctional Electrolyte-Gated Organic Field-Effect Transistors. *Advanced Materials* **24**, 4511–4517 (2012).

51. Kim, D.-J. *et al.* Organic electrochemical transistor based immunosensor for prostate specific antigen (PSA) detection using gold nanoparticles for signal amplification. *Biosens Bioelectron* **25**, 2477–2482 (2010).

52. Seshadri, P. *et al.* Low-picomolar, label-free procalcitonin analytical detection with an electrolyte-gated organic field-effect transistor based electronic immunosensor. *Biosens Bioelectron* **104**, 113–119 (2018).

53. Aerathupalathu Janardhanan, J. *et al.* Sensitive Detection of Sweat Cortisol Using an Organic Electrochemical Transistor Featuring Nanostructured Poly(3,4-Ethylenedioxythiophene) Derivatives in the Channel Layer. *Anal Chem* **94**, 7584–7593 (2022).

54. Palazzo, G. *et al.* Detection Beyond Debye's Length with an Electrolyte-Gated Organic Field-Effect Transistor. *Advanced Materials* **27**, 911–916 (2015).

55. Scheiblin, G. *et al.* Screen-printed organic electrochemical transistors for metabolite sensing. *MRS Commun* **5**, 507–511 (2015).

56. Bihar, E. *et al.* A Disposable paper breathalyzer with an alcohol sensing organic electrochemical transistor. *Sci Rep* **6**, 27582 (2016).

57. Khodagholy, D. *et al.* Organic electrochemical transistor incorporating an ionogel as a solid state electrolyte for lactate sensing. *J Mater Chem* **22**, 4440 (2012).

58. Magliulo, M. *et al.* Label-free C-reactive protein electronic detection with an electrolyte-gated organic field-effect transistor-based immunosensor. *Anal Bioanal Chem* **408**, 3943–3952 (2016).

59. Berto, M. *et al.* EGOFET Peptide Aptasensor for Label-Free Detection of Inflammatory Cytokines in Complex Fluids. *Adv Biosyst* **2**, 1700072 (2018).

60. Casalini, S., Bortolotti, C. A., Leonardi, F. & Biscarini, F. Self-assembled monolayers in organic electronics. *Chem Soc Rev* **46**, 40–71 (2017).

61. Selvaraj, M. *et al.* Label free detection of miRNA-21 with electrolyte gated organic field effect transistors (EGOFETs). *Biosens Bioelectron* **182**, 113144 (2021).

62. Manco Urbina, P. A. *et al.* Physical insights from the Frumkin isotherm applied to electrolyte gated organic transistors as protein biosensors. *J Mater Chem C Mater* **9**, 10965–10974 (2021).

63. Casalini, S. *et al.* Multiscale Sensing of Antibody–Antigen Interactions by Organic Transistors and Single-Molecule Force Spectroscopy. *ACS Nano* **9**, 5051–5062 (2015).

64. Berto, M. *et al.* Label free detection of plant viruses with organic transistor biosensors. *Sens Actuators B Chem* **281**, 150–156 (2019).

65. Solodka, K. *et al.* Detection of Neurofilament Light Chain with Label-Free Electrolyte-Gated Organic Field-Effect Transistors. *Adv Mater Interfaces* **9**, 2102341 (2022).

66. Ricci, S. *et al.* Label-free immunodetection of α-synuclein by using a microfluidics coplanar electrolyte-gated organic field-effect transistor. *Biosens Bioelectron* **167**, 112433 (2020).

67. Sensi, M. *et al.* Anti-drug antibody detection with label-free electrolyte-gated organic field-effect transistors. *Chemical Communications* **57**, 367–370 (2021).

68. Decataldo, F. *et al.* BMP-2 functionalized PEDOT:PSS-based OECTs for stem cell osteogenic differentiation monitoring. *Flexible and Printed Electronics* **4**, 044006 (2019).

69. Fenoy, G. E. *et al.* "Clickable" Organic Electrochemical Transistors. *JACS Au* **2**, 2778–2790 (2022).

70. Macchia, E. *et al.* Selective single-molecule analytical detection of C-reactive protein in saliva with an organic transistor. *Anal Bioanal Chem* **411**, 4899–4908 (2019).

71. Koutsouras, D. A., Prodromakis, T., Malliaras, G. G., Blom, P. W. M. & Gkoupidenis, P. Functional Connectivity of Organic Neuromorphic Devices by Global Voltage Oscillations. *Advanced Intelligent Systems* **1**, 1900013 (2019).

72. Galliani, M. *et al.* Flexible Printed Organic Electrochemical Transistors for the Detection of Uric Acid in Artificial Wound Exudate. *Adv Mater Interfaces* **7**, 2001218 (2020).

73. Diacci, C. *et al.* Diurnal in vivo xylem sap glucose and sucrose monitoring using implantable organic electrochemical transistor sensors. *iScience* **24**, 101966 (2021).

74. Sensi, M. *et al.* Monitoring DNA Hybridization with Organic Electrochemical Transistors Functionalized with Polydopamine. *Macromol Mater Eng* **307**, 2100880 (2022).

75. White, S. P., Frisbie, C. D. & Dorfman, K. D. Detection and Sourcing of Gluten in Grain with Multiple Floating-Gate Transistor Biosensors. *ACS Sens* **3**, 395–402 (2018).

76. White, S. P., Sreevatsan, S., Frisbie, C. D. & Dorfman, K. D. Rapid, Selective, Label-Free Aptameric Capture and Detection of Ricin in Potable Liquids Using a Printed Floating Gate Transistor. *ACS Sens* **1**, 1213–1216 (2016).

77. White, S. P., Dorfman, K. D. & Frisbie, C. D. Label-Free DNA Sensing Platform with Low-Voltage Electrolyte-Gated Transistors. *Anal Chem* **87**, 1861–1866 (2015).

78. Koklu, A. *et al.* Microfluidics integrated n-type organic electrochemical transistor for metabolite sensing. *Sens Actuators B Chem* **329**, 129251 (2021).

79. Parkula, V. *et al.* Harnessing Selectivity and Sensitivity in Electronic Biosensing: A Novel Lab-on-Chip Multigate Organic Transistor. *Anal Chem* **92**, 9330–9337 (2020).

80. Koklu, A. *et al.* Microfluidic Integrated Organic Electrochemical Transistor with a Nanoporous Membrane for Amyloid-β Detection. *ACS Nano* **15**, 8130–8141 (2021).

81. Ricci, S. *et al.* Label-free immunodetection of α-synuclein by using a microfluidics coplanar electrolyte-gated organic field-effect transistor. *Biosens Bioelectron* **167**, 112433 (2020).

82. Doumbia, A., Webb, M., Behrendt, J. M., Wilson, R. J. & Turner, M. L. Robust Microfluidic Integrated Electrolyte-Gated Organic Field-Effect Transistor Sensors for Rapid, In Situ and Label-Free Monitoring of DNA Hybridization. *Adv Electron Mater* **8**, 2200142 (2022).

83. Wustoni, S. *et al.* An organic electrochemical transistor integrated with a molecularly selective isoporous membrane for amyloid-β detection. *Biosens Bioelectron* **143**, 111561 (2019).

84. Minami, T. *et al.* An extended-gate type organic field effect transistor functionalised by phenylboronic acid for saccharide detection in water. *Chem. Commun.* **50**, 15613–15615 (2014).

85. Kergoat, L. *et al.* DNA detection with a water-gated organic field-effect transistor. *Org Electron* **13**, 1–6 (2012).

86. Hai, W. *et al.* Human influenza virus detection using sialyllactose-functionalized organic electrochemical transistors. *Sens Actuators B Chem* **260**, 635–641 (2018).

87. Berto, M. *et al.* EGOFET Peptide Aptasensor for Label-Free Detection of Inflammatory Cytokines in Complex Fluids. *Adv Biosyst* **2**, 1700072 (2018).

88. Macchia, E. *et al.* Why a Diffusing Single-Molecule can be Detected in Few Minutes by a Large Capturing Bioelectronic Interface. *Advanced Science* **9**, 2104381 (2022).

89. Macchia, E. *et al.* Organic Field-Effect Transistor Platform for Label-Free, Single-Molecule Detection of Genomic Biomarkers. *ACS Sens* **5**, 1822–1830 (2020).

90. Macchia, E. *et al.* Large-Area Interfaces for Single-Molecule Label-free Bioelectronic Detection. *Chem Rev* **122**, 4636–4699 (2022).

91. Sarcina, L. *et al.* A large-area organic transistor with 3D-printed sensing gate for noninvasive single-molecule detection of pancreatic mucinous cyst markers. *Anal Bioanal Chem* **414**, 5657–5669 (2022).

92. Macchia, E. *et al.* Single-Molecule Bioelectronic Label-Free Assay of both Protein and Genomic Markers of Pancreatic Mucinous Cysts' in Whole Blood Serum. *Adv Electron Mater* **7**, 2100304 (2021).

Chapter 3.
Aim and structure of the thesis

The work performed in this thesis was aimed towards the development of organic electronic-based devices to be employed as biosensors for multiple sclerosis. EGOT-based biosensors were developed while keeping in mind a potential future use for clinical purposes; therefore, the demonstration of their operation in biological fluids was among the main goals of the present work.

In the first part of the thesis (chapter 5), the fabrication and optimization of electrolyte-gated organic field-effect transistors is described. In particular, two different architectures were exploited, namely organic field-effect transistors and organic electrochemical transistors. Once satisfactory results, in terms of electrical performance, were obtained, the thesis work was focused on the investigation of different functionalization strategies to endow the transistors with biorecognition capability. To this aim, the Au gate electrode was employed as the sensing part of the device, and different molecules were tested as potential biomarkers of MS. The biorecognition capability of the developed biosensors was tested in buffered solutions for two potential MS biomarkers: the neuronal protein neurofilament light chain and mitochondrial DNA (chapters 6 and 7, respectively). Both strategies yielded satisfactory results. However, based on recent evidence, NF-L is considered to be a more accurate maker on the ongoing damage in the MS pathology, and, therefore, this protein was used as the target molecule to detect in the last part of the thesis, focused on the development of an EGOT-based biosensor in plasma samples (chapter 8).

Chapter 4.
Experimental techniques, materials, and methods

In the following chapter, the development of the EGOT-based biosensors presented in this thesis is described, covering the device fabrication process and the functionalization strategies used in order to endow the devices with biorecognition capability, as well as the different characterization techniques.

4.1. Fabrication of electrolyte-gated organic transistors

4.1.1. Substrates

In this work, two different substrate architectures were used for the fabrication of EGOTs: test patterns (TPs) from Fondazione Bruno Kessler (FBK), and Micrux thin-film interdigitated electrodes (IDEs).

- *Quartz test patterns (TPs)*

TPs were fabricated on a quartz substrate, of 1 cm^2 total area, and presented four interdigitated source and drain gold electrodes, with a channel length L = 15 μm and channel width W = 30 mm (W/L = 2000). Source and drain electrodes were made of Au, with a thickness of 5 nm, and an adhesive layer of Cr of a few nm, patterned by photolithography and lift-off techniques on a quartz substrate. Prior to the semiconductor deposition, TPs were rinsed with acetone in order to remove the photoresist layer and were cleaned following a standard procedure of i) wash in hot acetone (70°C) for 10 minutes, and ii) immersion in piranha solution (1:1 concentrated H_2SO_4:H_2O_2) at 150°C for 1 minutes. Finally, TPs were rinsed abundantly with DI-H_2O, and dried under N_2 flow.

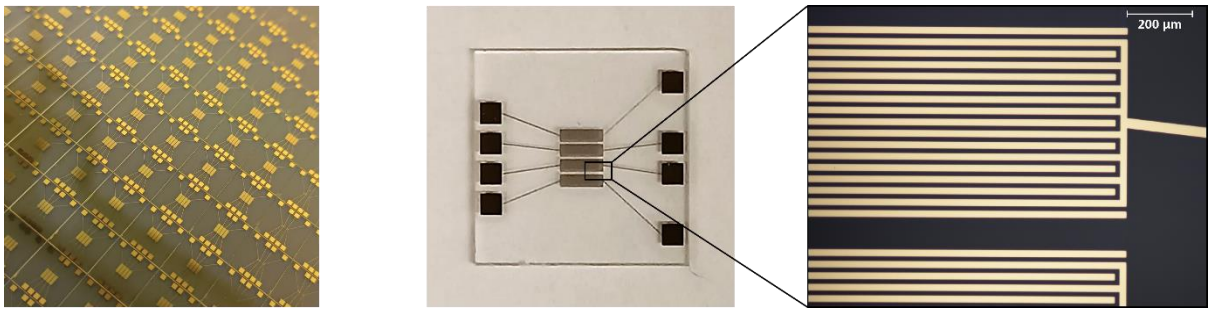

Figure 4.1. Standard FBK quartz test patterns used for the fabrication of EGOT-based biosensors, with a magnification of the interdigitated drain and source Au electrodes.

- *Micrux thin-film interdigitated electrodes (IDEs)*

Micrux IDEs were fabricated using a glass substrate, of 60 mm^2 total area, with interdigitated source and drain electrodes (3.5 mm Ø). The electrodes presented a L = 10 μm and a W = 490 mm (W/L = 49000), and were made of Au with a Ti adhesive layer of 150 and 50 nm thickness, respectively. Before the semiconductor deposition, the substrates were cleaned by sonication in a 1% Hellmanex™ III aqueous solution, followed by sonication in DI-H_2O, and finally

sonication in ethanol. Every sonication step lasted for 15 minutes, and once the cleaned procedure was completed, the substrates were dried gently under N_2 flow.

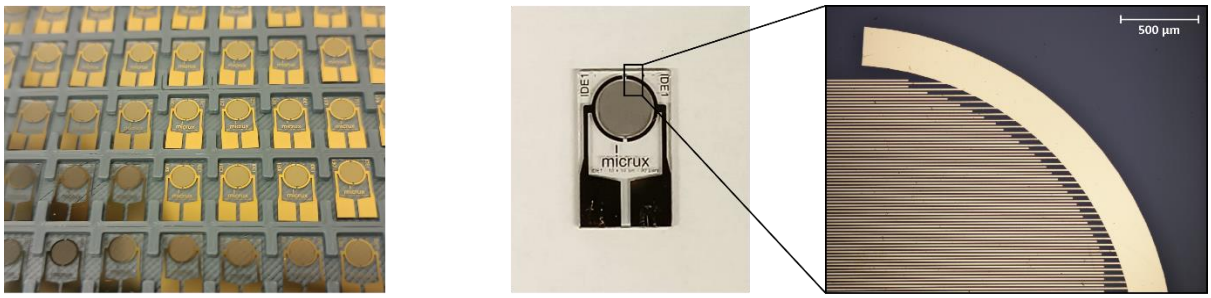

Figure 4.2. Micrux glass substrates used in this thesis for EGOT, with a magnified view of the interdigitated electrodes.

4.1.2. Semiconductor deposition

In this thesis, two different organic materials have been used as semiconductor: the small molecule TIPS-pentacene (6,13-bis(triisopropylsilylethinyl)pentacene)), and the polymer DPP-DTT (poly[3,6-bis(5-thiophen-2-yl)-2,5-bis(2-octyldodecyl)pyrrolo[3,4-c]pyrrole1, 4(2H,5H)-dione-2,2'-diyl-alt-thieno[3,2-b]thiophen-2,5-diyl]).

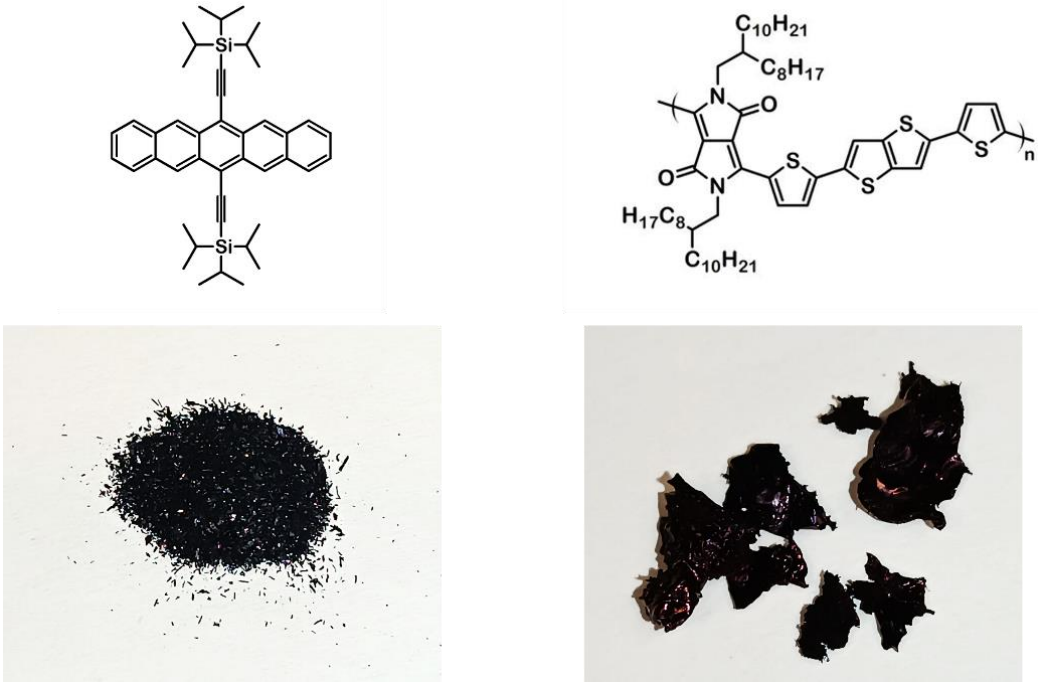

Figure 4.3. Chemical structure (top) and appearance (bottom) of the OSC TIPS-pentacene (left) and DPP-DTT (right).

TIPS-pentacene was used for the fabrication of EGOFET-based biosensors. The OSC solution was prepared by dissolving TIPS-pentacene in a mixture of organic solvents (toluene:hexane in a ratio of 80:20) to a final concentration of 2% (w/w). In order to achieve the complete dissolution of the OSC, the solution was stirred at 80°C for at least 3 hours. The quartz TPs were used as substrate, and TIPS-pentacene was deposited on top of the interdigitated source and drain electrodes by drop casting or spin coating.

Drop casting is probably the easiest technique for OSC deposition. It consists of depositing a drop of the solution on the substrate and waiting for the solvent to evaporate, as depicted in Figure 4.4 (panel A). Because of its simplicity, it is one of the most widely used methods for OSC deposition. The morphology of the obtained film strongly depends on factors such as the temperature and concentration of the solution or the solvent evaporation rate, therefore the temperature affects the outcome of the process. Small variations in these parameters often lead to a non-uniform film formation, with variable thickness and morphology, strongly limiting the reproducibility.

Another common technique for thin film deposition is spin coating (Figure 4.4, panel B). This method consists in dropping the OSC solution on the substrate and spinning the sample at high speed. The rotational speed applied spreads the solution while, simultaneously, the solvent is evaporated, leading to the formation of a uniform film all over the substrate. The thickness of the formed film can be controlled by the initial solution concentration and viscosity, and the parameters of the spin coater (revolutions per minute, acceleration, and total time).

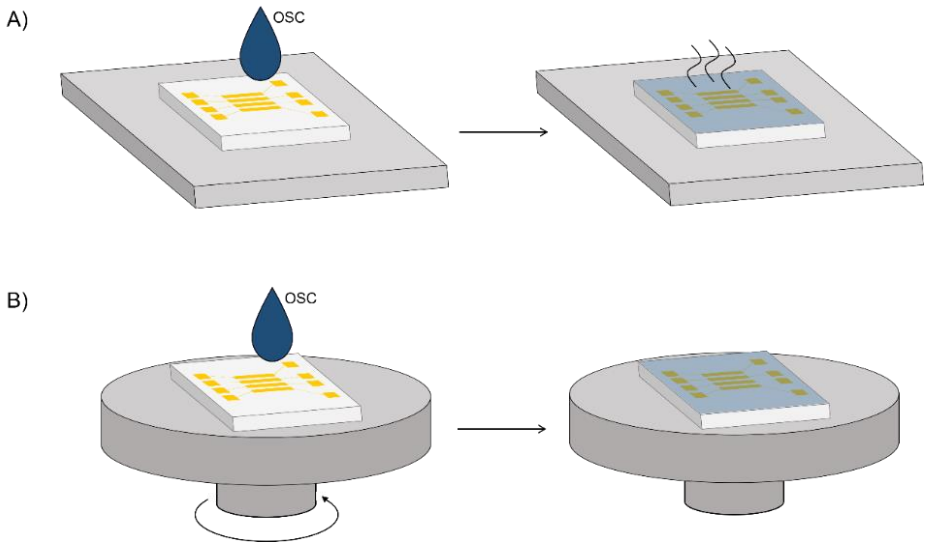

Figure 4.4. Schematic illustration of OSC deposition by drop casting (A) and spin coating (B) techniques.

In this thesis, with respect to the formation of a TIPS-pentacene channel, different OSC deposition techniques and annealing methods were investigated:

Protocol 1. Deposition of 50 μL of TIPS-pentacene by drop casting, followed by a thermal annealing at 60°C for 30 minutes.

Protocol 2. Deposition of 80 μL of TIPS-pentacene by spin coating at 600 rpm for 15 seconds, followed by combined thermal and solvent vapour annealing. The annealing step consisted in placing the substrate on a hot plate at 60°C, covered by a glass Petri dish, creating a solvent vapour-rich environment, for 30 minutes.

Protocol 3. Deposition of 80 μL of TIPS-pentacene by spin coating, followed by curing in vacuum at room temperature for 40 minutes.

The crystallization process was monitored using an optical microscope, and the electrical performance of the EGOFETs fabricated following the different protocols was investigated. The outcome of the fabrication process will be discussed in chapter 5.

The OSC of choice for the fabrication of OECT-based biosensors was the molecule DPP-DTT. The solution was prepared by dissolving the polymer in an organic solvent, 1,2-dichlorobeneze, to a final concentration of 5 mg/mL. The solution was then stirred at 80°C for at least 1 hour in order to assure the complete dissolution of DPP-DTT. Once a homogeneous solution was achieved, 5 μL of the OSC solution were deposited on the substrate, either FBK quartz TPs or Micrux IDEs, by spin-coating (1200 rpm, 2 minutes). The substrates were cured in the oven at 140°C for 45 minutes, and the devices were kept in a 50 mM phosphate buffer until use.

4.2. Electrical characterization

All the electrical measurements were performed at room temperature inside a Faraday cage. Source, drain, and gate electrodes were connected to an Agilent B2902A Source Measure Unit, and the electrical redout was acquired by means of a personalized control software (Figure 4.5). An Au wire (Au 99.99%, 1 mm Ø), immersed in the electrolyte, was used as the gate electrode during the experiments.

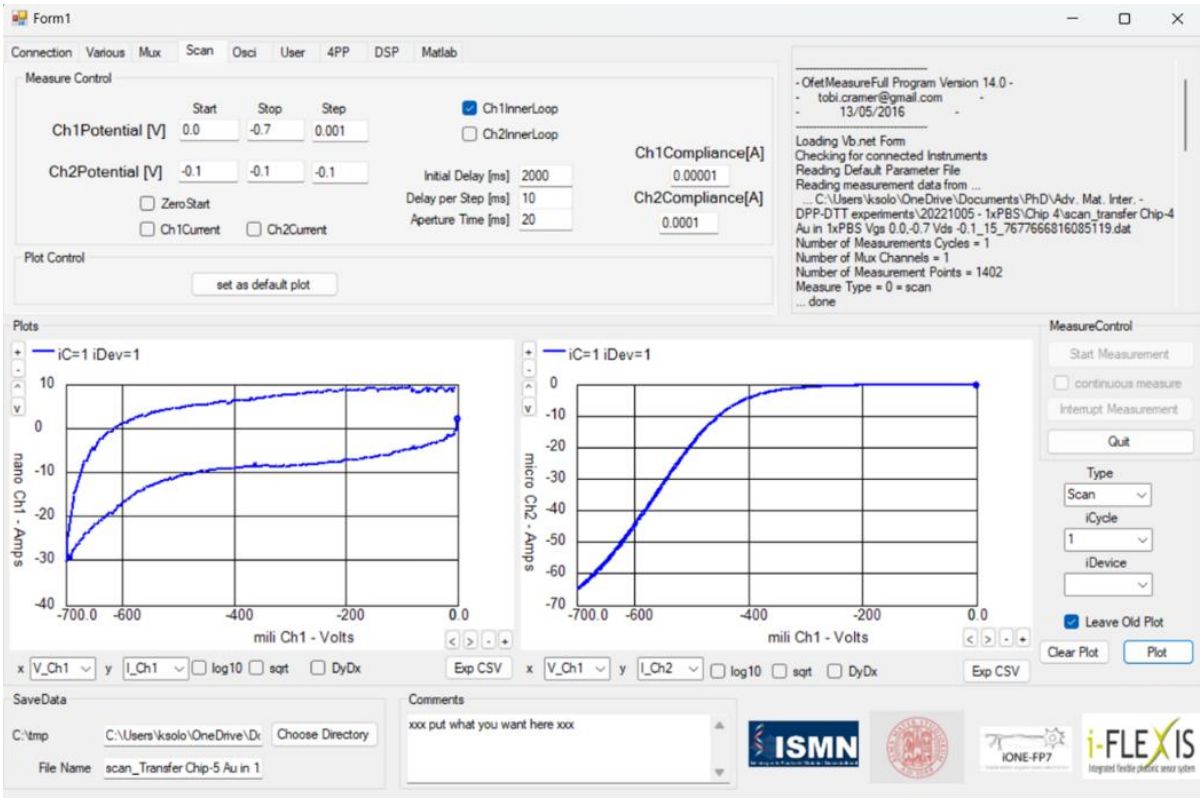

Figure 4. 5. Visual interface of the personalized measurement software used to perform all the electrical characterization. A representative transfer curve (I_{DS} vs. V_{GS}) can be seen in the right frame, and the gate leakage current (I_{GS} vs. V_{GS}) is shown in the left.

4.2.1. EGOT characterization

The electrical characterization of EGOFET, TIPS-pentacene-based transistors was performed in a phosphate buffer solution (50 mM PB, pH 7.4)**.** Transfer characteristics were acquired by applying a sweeping gate-source potential from 0 to -0.5 V, while output characteristics were recorded by sweeping the drain-source potential from 0 to -0.5 V, at a constant V_{GS}, from 0 to -0.5 V.

An extensive investigation of the electrical performance of OECT, DPP-DTT-based transistors in different solutions, including PBS, artificial sweat, artificial saliva, artificial wound exudate, and blood plasma, was performed. The effect of exposing the device to complex solutions, high ionic strength, or changes in pH, as well as the stability of the device when exposed to these solutions, were investigated. During these experiments, an Au wire was used as the gate electrode, and the electrolyte (50 µL) was confined inside an adhesive pool. First, 15 continuous transfer measurements were acquired sweeping the V_{GS} potential from 0 to -0.7 V, at a constant V_{DS} of -0.1 V. In order to investigate the stability of the device and the effect of

changing the buffer, this was repeated 3 times. Output characteristics were acquired by sweeping the V_{DS} from 0 to -0.4 V, at constant V_{GS}, from 0 to -0.7 V. In addition, the response of the device to small changes in the gate-source potential was investigated. This was performed by applying pulses, small potential differences (-100, -50, and -10 μV), at the gate-source potential, while recording the I_{DS} as a function of time at a constant V_{GS} (V_{GS} at which $g_m = g_{m,max}$). Finally, the time response of the device to changes in V_{GS} was investigated. In this case, I_{DS} was recorded as previously mentioned, and pulses of -0.1 V were applied at the gate-source potential.

4.2.2. Sensing experiments

The sensing experiments described in chapter 6, using an EGOFET-based biosensor, were performed using a phosphate buffer solution as electrolyte (50 mM PB, pH 7.4). The Au gate electrode was immersed in 50 μL of the electrolyte and transfer characteristics were repeatedly recorded until reaching stabilization (30 measurements). The gate-source potential was applied from V_{GS} = -0.1 to -0.6 V, while maintaining a constant drain-source potential of V_{DS} = -0.2 V (linear regime). Once stabilization was reached, dose curve experiments were performed by exposing the device to increasing concentrations of NF-L, from 100 fM to 10 nM (in 50 mM PB, pH 7.4).

The electrical monitoring of mtDNA hybridization using a DPP-DTT-based biosensor (chapter 7) was performed by recording transfer characteristics in PBS containing increasing concentrations of ss-mtDNA, complementary to the capture probe immobilized on the Au gate electrode. The gate electrode was immersed in 50 μL of the electrolyte, confined in an adhesive pool. The V_{GS} applied ranged from to -0.3 to -0.7 V, while applying a constant V_{DS} of -0.1.

The detection of NF-L in blood plasma was performed using a DPP-DTT-based immunosensor (chapter 8). First, the electrical performance of the biosensor was studied in PBS and blood plasma from healthy donors. The plasma was previously diluted in PBS to a ratio of 1/50. Once the electrical performance in both media was assessed, sensing experiments were performed by exposing the device to plasma samples spiked with increasing concentrations of NF-L, from 50 pM to 10 nM, while recording *I-V* characteristics. The experiments were performed by sweeping the V_{GS} from -0.2 to -0.8 V, at a constant V_{DS} of -0.1 V. During the experiments, a volume of 50 μL of the electrolyte was used, confined inside an adhesive pool.

4.2.3. Parameter extraction

Transconductance, threshold voltage and current on/off ratio were extracted from the average of the last transfer curves recorded. Transconductance was extracted from the first derivative of the transfer curve, while threshold voltage was obtained from the second derivative. Hysteresis was calculated as the difference in the drain current between the forward and backward scans of the transfer curve at the same gate potential applied ($I_{DS,F}$-$I_{DS,B}$), normalized with respect to $I_{DS,max}$.

4.3. Gate functionalization

One of the major advantages of EGOT-based biosensors is their capability of selectively detect target analytes at very low concentrations[1–3]. This is generally achieved by immobilizing a recognition unit, i.e., an antibody or an aptamer, in one of the relevant interfaces of the device. In this work, the gate electrode was used as the sensing surface of the device and specific antibodies or oligonucleotide probes as biorecognition elements.

Polycrystalline gold wires were used as gate electrodes, which, prior to functionalization, were subjected to a cleaning procedure consisting of immersion in 2.5 M KOH at 130°C for 4 hours, followed by immersion in concentrated H_2SO_4 at 220°C for 2 hours. Then, the electrodes were rinsed with abundant water, and a final electrochemical polish in acidic conditions (1 M H_2SO_4) was performed by sweeping the potential between 1.5 and -0.25 V for a minimum of 5 cycles.

Different gate functionalization strategies were investigated. The area of the gate electrode was kept constant by means of a passivation layer.

4.3.1. Protein G-mediated antibody immobilization

Protein G is a surface protein expressed in some bacteria that presents high affinity towards immunoglobulins G. It specifically binds to the fragment crystallizable region of IgGs, and it is a popular technique for antibody immobilization[4–6]. Because of the binding between protein G and the Fc region, the antibodies are immobilized with a defined and uniform orientation, leaving the Fab region free and accessible for the antigen to bind[7].

In this thesis, protein G-mediated antibody immobilization on Au gate electrodes was explored for the development of an EGOFET-based biosensor for detection of NF-L (chapter 6). The first step of the gate functionalization consisted of the formation of a protein G monolayer on the Au surface. This was achieved by incubating overnight at 4°C the gate electrode in a recombinant protein G solution (2 mg/mL in 50 mM phosphate buffer, pH 7.4). Protein G presented a single cysteine residue, that binds covalently the Au gate electrode. Once a covalently bound monolayer of protein G was formed, specific antibodies were immobilized on the gate by incubating the electrode with a solution of anti-NF-L (0.1 mg/mL in 50 mM phosphate buffer, pH 7.4) for 1 hour at room temperature. The last step of the gate functionalization consisted of the passivation of the electrode by the formation of a self-assembled monolayer (SAM) of thiolated oligoethylene glycol (OEG). Because of the antifouling properties that OEG SAMs exhibit[8,9], this final step was incorporated in an attempt to reduce nonspecific binding. After each functionalization step, the gate electrode was washed carefully with 50 mM phosphate buffer.

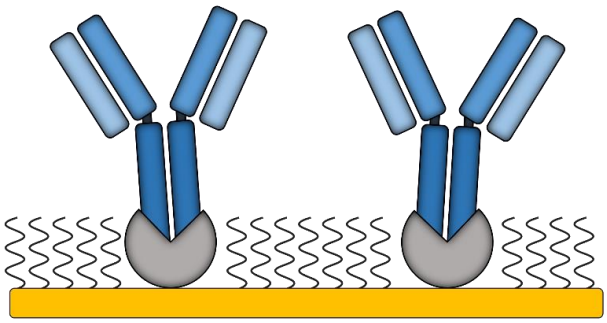

Figure 4.6. Schematic illustration of protein G mediated antibody immobilization on the Au gate surface. Protein G is represented in grey, while the antibody is blue.

4.3.2. Avidin-biotin affinity for DNA immobilization

The interaction between avidin and biotin, despite being non-covalent, exhibits extremely high affinity, with a K_D of ~10^{-15} M. This interaction is rapid and very stable, as factors as temperature or pH have a minimal influence on the stability of the bond[10,11]. Biotin is a small molecule that can be easily attached to biomolecules, without affecting their conformation or functionality. Because of the high affinity and stability of the avidin-biotin interaction, and the facility of using biotin for labelling, this interaction has been widely exploited for coupling biomolecules of interest[12,13], as well as for the immobilization of DNA sequences[14–16]. In chapter 7, this strategy was employed for the development of a biosensor for mtDNA detection,

using to this end a specific biotin-labelled single-stranded (ss)-mtDNA sequence as the capturing probe (P-DNA).

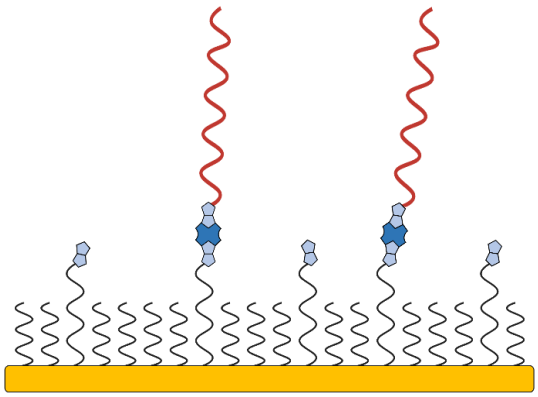

Figure 4.7. Schematic illustration of the Au gate functionalization for monitoring mtDNA hybridization. The biotin moieties are represented in clear blue, while neutravidin in dark blue, and the capturing probe, P-DNA, is red.

To form a mixed SAM monolayer with biotin moieties on the Au surface, the gate electrodes were incubated overnight in a mixed Biotin-OEG SAM and OEG SAM (0.1:0.9 mM in ethanol). After the incubation, the excess of SAM was removed by rinsing gently the electrodes with ethanol and with PBS containing 0.05% Tween 20 (PBS-T). Tween 20 is a surfactant commonly used as a detersive agent that, during these experiments, was used with the aim of reducing nonspecific interactions. Then, the electrodes were incubated with a solution of neutravidin, an avidin analogue, (2 μM in PBS-T) for 30 minutes at room temperature. Next, the Au electrodes were incubated with a specific ss-mtDNA sequence (200 nM in PBS-T) for 20 minutes. This was achieved by adding a biotin tag on the 5' end of the oligonucleotide. A final incubation step of 15 minutes in PBS-T was performed prior to the electrical measurements. Once the DNA sequence was immobilized on the Au gate surface, it was used as the capturing probe for the complementary mtDNA sequence. The specific oligonucleotide sequences for P-DNA, C-DNA, and non-complementary (NC-DNA) probes are detailed in Table 4.1. All the immobilization steps were done at room temperature.

Table 4.1. mtDNA oligonucleotide sequences employed during the sensing experiments.	
P-DNA	5'-Biotin-AAA AAA TTA CCG GGC TCT GCC ATC T-3'
C-DNA	5'-AGA TGG CAG AGC CCG GTA A-3'
NC-DNA	5'-TAA CAA CAT ACC CAT GGC CA-3'

4.3.3. Avidin-biotin affinity for antibody coupling

In chapter 8, the neutravidin-biotin interaction was exploited for the immobilization of specific antibodies on the Au gate electrodes to serve as the sensing elements in an EGOT-based immunosensor for the detection of NF-L in blood plasma.

During these experiments, with the aim of increasing the gate to channel ratio, coiled Au wires were used as gate electrodes. The Au electrodes were immersed overnight, at room temperature, in a mixed SAM solution, containing Biotin-OEG SAM and OEG SAMs (0.1:0.9 mM in ethanol). The next day, the excess of SAM was removed by rinsing gently the electrodes with ethanol and with PBS. Then, the gate electrodes were incubated in a neutravidin solution (2 μM in PBS), for 30 minutes at room temperature. After the conjugation of neutravidin to the biotin moieties of the SAM, anti-NF-L antibodies were immobilized on the surface. This was achieved by exposing the electrodes to a biotinylated anti-NF-L solution (0.1 mg/mL in PBS) for 1 hour at room temperature. Finally, in order to prevent nonspecific binding, Au gate electrodes were incubated in a solution containing 0.1 mg/mL BSA + 0.05% Tween 20 (30 minutes at room temperature). After every functionalization step, the Au gate electrodes were gently rinsed with PBS, unless specified differently.

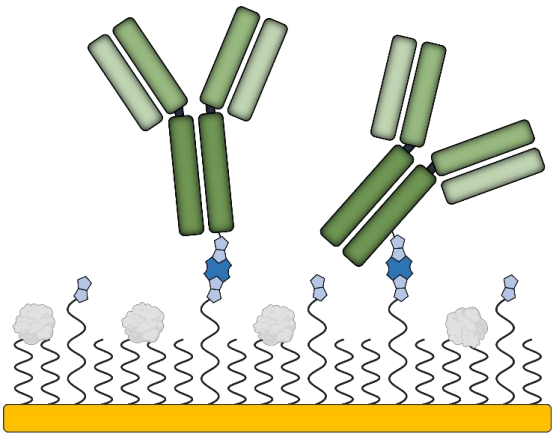

Figure 4.8. Schematic illustration of antibody immobilization on the Au gate surface by exploiting the biotin-neutravidin interaction. The biotinylated antibody is represented in green, biotin and neutravidin in light blue and dark blue, respectively, and BSA in grey.

4.4. Electrochemical characterization

Electrochemistry is a heterogeneous field that encompasses several techniques for the study of reactions involving electron transfer. Among these, cyclic voltammetry (CV) is a widely used

for the investigation of redox reactions occurring at the electrode-electrolyte interface. CV is generally performed in a three-electrode cell, comprising the working (WE), reference (RE), and counter (CE) electrodes. During CV measurements, cyclic voltammograms are recorded by applying a sweeping potential to the WE while recording the generated current. The potential applied is commonly reported against the RE, as it has a well-defined and stable equilibrium potential[17].

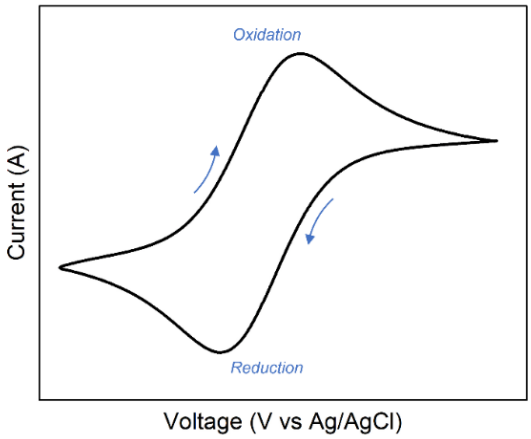

Figure 4.9. Typical "duck shape" of a cyclic voltammogram, with clearly distinguishable reduction and oxidation peaks.

In this thesis, cyclic voltammetry was used to monitor the gate functionalization strategy used for the protein G-driven antibody immobilization. All the measurements were performed in 5 mM $K_3[Fe(CN)_6]$ solution containing 1 M KCl, at 50 mV/s. The experiments were carried out using a CH Instrument Potentiostat 760c model, in a three-electrode cell setup, where the Au gate electrode was used as the working electrode, and a Pt and Ag/AgCl electrodes were used as counter and reference electrodes, respectively.

4.5. Surface plasmon resonance and surface plasmon-enhanced fluorescence spectroscopy

Surface plasmon resonance (SPR) is an optical phenomenon resulting from the excitation of the electrons (surface plasmons, SPs) of a metal surface by the incident photons, which induces the propagation of the SPs along the surface[18]. The excitation of the SPs occurs at a certain angle of the incident light that is strongly dependent on the refractive index (RI) of the material. Small changes in the RI will be reflected in a shift of the SPR angle of incidence or wavelength.

By exploiting this extremely high sensitivity, SPR has been widely employed for real-time monitoring of biomolecular interactions, as well as for kinetics studies, as any binding event occurring at the metal surface will trigger a change in the RI that can be directly measured from the angle/wavelength shift. Since the first demonstration of SPR for the investigation of processes at metal surfaces or for sensing, dating back in the 1980s[19,20], enormous advances have been achieved in the field, placing SPR as one of the most useful tools for the characterization and quantification of molecular interactions[21–23].

The coupling to surface plasmons can be done in different ways. In the present work, this was achieved via a high index prism (prism-coupling), using the Kretschmann configuration, illustrated in Figure 4.10. In this configuration, the incident light is directed through a prism that is coupled to a metal layer, and the reflected light is recorded as a function of the incident angle. The metal layer serves as a sensor, and is used to immobilize probe molecules. When the target analyte is injected into the system, the binding between probe and analyte will induce a change in the RI as well as in the angle of reflection that can be easily quantified.

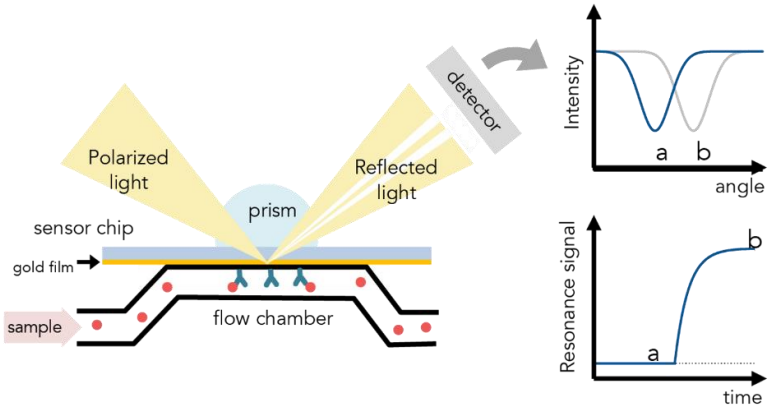

Figure 4.10. Simplified chart of the Kretschmann configuration. The binding events occurring at the sensor surface are monitored in real-time. The SPR signal is recorded as a function of variations in the RI induced by analyte binding. The figure was adapted from reference 24[24].

Despite being a powerful tool for studying biomolecular processes, SPR presents some limitations, as its sensitivity is limited for analytes of low molecular weight or present at low concentrations. In order to increase the sensitivity, SPR can be combined with fluorescent spectroscopy, in a technique known as surface plasmon-enhanced fluorescent spectroscopy (SPFS)[25]. SPFS offers the advantages of SPR, such as real-time monitoring of biomolecules interaction, with high sensitivity. Furthermore, when compared to traditional fluorescence spectroscopy techniques, in SPFS the fluorescent signal is significantly increased due to the strong coupling between the fluorophores and the electromagnetic field of the surface plasmons

at the metal surface[26,27]. In the last years, many SPFS-based biosensors have been reported for monitoring biomolecular interactions, including protein binding[28,29], and DNA hybridization[30,31].

In this thesis, SPFS was used to monitor in real-time the functionalization strategy for mtDNA immobilization, as well as the hybridization with its complementary sequence. The experiments were performed at the facilities of the Austrian Institute of Technology. The sensor chips were prepared by evaporating Au, with a thickness of 50 nm, on BK7 glass slides, with a Cr adhesive layer of 2 nm. Then, the Au slides were rinsed with ethanol and DI-H_2O, dried, and cleaned with UV-ozone for 20 minutes. Once the cleaning procedure was finished, the Au slides were immersed overnight in a mixed Biotin-OEG SAM and OEG SAM solution (0.1:0.9 mM in ethanol). The next day, the Au slides were rinsed with ethanol to remove the excess of SAM, and gently dried with N_2 flow.

The optical configuration employed for fluorescence readout for total internal reflection fluorescence. In the optical setup, a beam emitted from a HeNe laser passed through a laser band-pass filter, a polarizer, and a neutral density filter (1%). A TM polarized beam at the wavelength λ_{ex} = 633 nm with the intensity of 1.5 μW was coupled to a 90° prism coupler made of LASFN9 glass. The Au slide was optically matched to the prism base using immersion oil. In order to delimit the liquid sample, a flow cell was clamped on the surface of the sensor chip. The flow cell, with a volume of 1.5 μL, was made from a thin PDMS gasket and sealed by a transparent fused silica glass substrate. Inlet and outlet ports were drilled into the silica substrate, that were connected by tubing to a peristaltic pump. The angle of incidence θ of the excitation beam hitting the gold sensor surface was adjusted at the reflectivity minimum in order to assure the resonant coupling to SPs at the interface with an aqueous sample. The enhanced field intensity of SPs excited randomly oriented fluorophore labels at the distance *f* from the gold sensor surface. The emitted fluorescence light at λ_{em}= 670 nm was collected by a module with a lens and passed through a set of filters consisting of a notch filter that was used to block the excitation wavelength λ_{ex} and two bandpass filters with the transmission window centered at the λ = 670 nm and spectral width of about 10 nm. The fluorescence beam was focused on the input of a photomultiplier (H6240-01, Hamamatsu, Japan) that was connected to a counter (53131A from Agilent, USA). The output from the counter was recorded in counts per second (cps) by using software Wasplas developed at the Max Planck Institute for Polymer Research in Mainz (Germany). The detailed description of the SPFS setup is described in reference 32[32].

During the assay, the binding of the neutravidin molecules to the exposed biotin moieties of the SAM surface and the further immobilization of the capturing mtDNA probe was monitored by SPR. A solution of PBS-T was flushed into the system (50 µL per minute), which served as the baseline, and the SPR signal was recording by measuring the reflected beam intensity. Then, the Au chip was incubated with a neutravidin solution (2 µM in PBS-T) for 30 minutes, and with a solution containing the capturing mtDNA (P-DNA, 200 nM in PBS-T), for 20 minutes. After every immobilization step, a washing step was done by flushing PBS-T into the system for 5 minutes.

Because of its small size and low concentration, the hybridization of the complementary mtDNA sequence with the capturing probe could not be followed using SPR, and it was monitored by using SPFS instead. To prove the specific interaction of both DNA strands, a sandwich-type assay was developed. The schematic of the assay is illustrated in Figure 4.10. After the immobilization of the capturing mtDNA probe on the Au surface, a solution containing increasing concentrations of complementary mtDNA (C-DNA) was flushed into the system. This sequence was longer than the capturing probe, therefore after the hybridization, part of the complementary oligonucleotide sequence was free, available for binding. After the injection of every concentration, an additional DNA probe (L-DNA), complementary to C-DNA, was injected into the system at a constant concentration of 10 nM. The L-DNA probe was specifically labelled with a fluorophore at the 3' end. The emitted fluorescence signal was then detected and recorded. The Au sensor was incubated with C-DNA and L-DNA for 10 minutes each and washed with PBS-T after every hybridization step. The specific mtDNA sequences used in these experiments are detailed in Table 4.2.

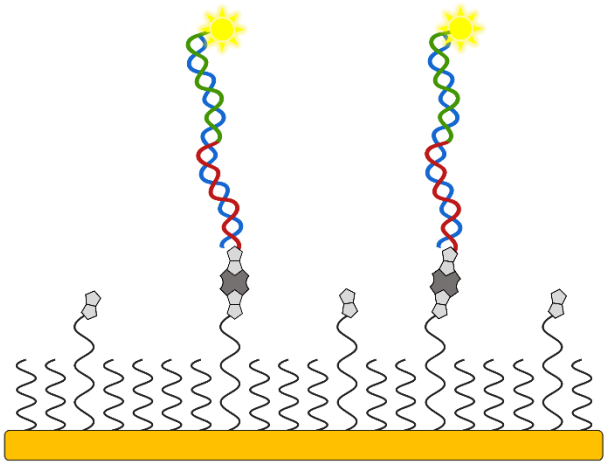

Figure 4.11. Schematic representation of the sandwich SPFS assay. Biotin and neutravidin are depicted in grey (light and dark, respectively), P-DNA in red, C-DNA in blue, and L-DNA with a fluorescent tag in green and yellow, respectively.

Table 4.2. mtDNA oligonucleotide sequences used for SPFS experiments.	
Capturing sequence (P-DNA)	5'-Biotin-AAA AAA TTA CCG GGC TCT GCC ATC T-3'
Complementary sequence (C-DNA)	3'-AAT GGC CCG AGA CGG TAG AAT TGT TTG GGA CAA-5'
Fluorescently labelled sequence (L-DNA)	5'-TA ACA AAC CCT GGT-AlexaFluor647-3'

4.6. Fiber optic-based surface plasmon resonance spectroscopy

Alternatively, the coupling to surface plasmons can be achieved by replacing the prism with an optical fiber (FO). In this setup, the cladding of the fiber is removed and instead, a thin layer of a metal, typically Au, is deposited, which serves as the sensing element. White light is coupled into the FO and travels through the core of the fiber, that acts as a waveguide, to the tip, exciting the surface plasmons. An event occurring at the FO surface will lead to a local refractive index change and therefore modifies the resonance condition to couple to SPs. This can be easily tracked by recording the SPR signal over time[33,34]. Since the first demonstration of a FO-based SPR sensor in the 1990s[34], the use of FOs has been widely applied for biosensing purposes. In addition to the advantages of traditional SPR, such as the label-free and real-time monitoring of biomolecular interactions, FO-SPR allows the miniaturization and low-cost fabrication[35,36].

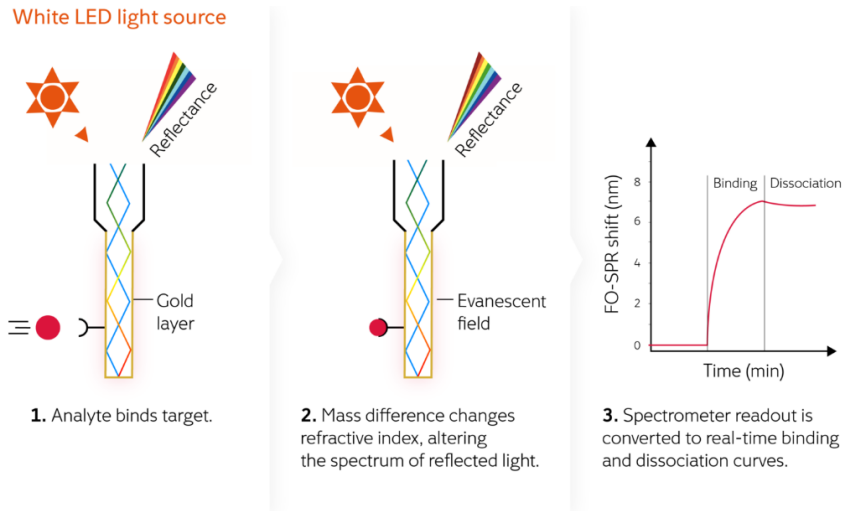

Figure 4.12. Simplified schematic of the working principle of the detection of biomolecule interaction using FO-SPR[37].

In chapter 8, the antibody immobilization on the Au electrodes was monitored in real-time using FO-SPR. This technique presents the advantage that the FO resembles the Au wire employed in the electrical experiments. The fiber tips were coated homogenously with 50 nm of Au in a sputter coater. The FO setup was mounted by coupling polychromatic light from a halogen light source to a Y optical splitter input, guiding the light to the tip of the plasmonic fiber prob to resonantly excite propagating SPs on the outer Au surface. The Au acted as a mirror, reflecting the light, that was coupled back to the Y optical splitter, connected to a spectrometer. The measured spectrum of the reflected light beam from the fiber was normalized with that of the fiber in the air. The normalized reflectivity spectra were processed by a dedicated LabView software. The detailed fabrication procedure of FO and the setup are described in reference 38[38]. All the FO-SPR experiments were performed at the Austrian Institute of Technology.

Previous to the assay, the fibers were incubated in a biotin-OEG solution, as described in section 4.3.2, resulting in the formation of SAM on the Au FO surface. Then, the fibers were mounted in the FO setup and immersed in a PBS solution while recording the SPR signal. After assessing the baseline, the fibers were incubated with neutravidin solution (2 μM in PBS) for 1 hour, followed by a wash with PBS (5 minutes). The washing step was performed twice, in order to create a new baseline for the next immobilization step. After the washing steps, the fiber was incubated with a specific anti-NF-L antibody (0.1 mg/mL in PBS), containing a biotin residue. The incubation step lasted 1 hour, and then the fiber was washed with PBS, in order to remove the non-bound antibody. Finally, after assessing the immobilization process, a sucrose calibration was performed to assess the sensitivity of the fiber and normalize the obtained signal.

4.7. Morphological characterization: atomic force microscopy & scanning electron microscopy

Atomic force microscopy (AFM) is a technique of the family of scanning probe microscopy developed in the 1980s that allows the investigation of surface topographies at the nanoscale level[39]. In AFM, an elastic cantilever with a sharp tip is used to scan the sample. The forces resulting from the interaction of the tip with the surface lead to the deflection of the cantilever.

By using a laser beam on top of the cantilever and a photodiode, the reflection can be measured, proving information on the tip-surface interaction forces.

Another technique widely used for surface characterization is scanning electron microscopy (SEM). SEM was developed in the early 1950s, and the working principle is similar to the traditional optical microscopy, with the singularity that instead of light, a focused beam of electrons is used to scan the sample. This allows the characterization at high magnification with extremely high resolution, providing structural and morphological information at the micro- and nanoscale level[40].

In chapter 6, AFM and SEM techniques were used as a complementary evaluation of the Au electrodes surface. In order to optimize the morphological analysis, planar Au electrodes were used instead of the Au wires used during the experiments. The planar electrodes were functionalized following the procedure described previously, and AFM and SEM analysis was performed upon the incubation with increasing concentrations of NF-L.

AFM, operated in semi-contact mode, was performed with a SMENA solver platform (NT-MDT Spectrum Instruments, Limerick, Ireland), and the images were analysed using Gwyddion 2.56 freeware[41]. SEM characterization was performed using a SEM Zeiss Sigma equipped with a Schottky field emission gun operating at 5 keV.

4.8. Solutions and buffers

The detailed composition of all the solutions and buffers used in this thesis is reported in Table 4.3. PBS was prepared using a commercially available preparation (1x PBS).

The plasma samples used in this thesis belonged to healthy donors and were collected in the framework of a previous project[42]. Samples of venous blood were collected by venepuncture, after obtaining ethical clearance by local Ethical Committee and patient's informed consent. Blood was collected into tubes containing ethylenediaminetetraacetic acid to avoid coagulation. Plasma was separated from blood cells by centrifugation and stored at -80°C until use.

Table 4.3. Detailed list of the composition of the buffers and solutions used during this thesis. The concentration is expressed as molarity (M).	
Phosphate buffer, pH 7.4	
Na_2HPO_4	50×10^{-3}
KH_2PO_4	10×10^{-3}
Artificial sweat[43]*, pH 4.7*	
NaCl	342×10^{-3}
NH_4Cl	327×10^{-3}
Na-Lactate	16.7×10^{-3}
Urea	83.3×10^{-3}
Acetic acid	41.6×10^{-3}
Artificial saliva[44]*, pH 7.2*	
Na_2HPO_4	4.227×10^{-3}
$CaCl_2$	5.406×10^{-3}
KCl	5.366×10^{-3}
NaCl	6.845×10^{-3}
Urea	133×10^{-3}
Artificial wound exudate[45]*, pH 6.72*	
NaCl	124×10^{-3}
$MgCl_2$	831×10^{-6}
$CaCl_2$	2.48×10^{-3}
$NaHCO_3$	36.8×10^{-3}
Glucose	5×10^{-3}
BSA	150×10^{-6}
Na-Lactate	10×10^{-6}

4.9. Chemicals and reagents

EGOT substrates: quartz test patterns were purchased from Fondazione Bruno Kessler (Trento, Italy), and Micrux thin-film interdigitated electrodes from Micrux Technologies (Gijón, Spain).

Chemicals, salts, and solvents: phosphate salts, potassium ferricyanide, sodium chloride, potassium chloride, magnesium chloride, calcium chloride, ammonium chloride, sodium lactate, sodium bicarbonate, glucose, urea, bovine serum albumin, potassium hydroxide, hydrogen peroxide, sulfuric acid, acetone, ethanol, hexane, toluene, 1,2-dichlorobenzene were purchased from Sigma-Aldrich (Merck Life Science, Milano, Italy).

Organic semiconductors: TIPS-pentacene (M151) and DPP-DTT (M0311A6) were purchased from Ossila (Sheffield, United Kingdom).

SAMs: OEG SAM (11-mercaptoundecyl-triethylene glycol, 673110) was purchased from Sigma-Aldrich (Merck Life Science, Milano, Italy), and biotin-OEG SAM (TH 004-m11.n6) was purchased from Prochimia Surfaces (Advanced Wave Sensors, Paterna, Spain).

Antibodies, proteins and oligonucleotides: recombinant cys-protein G (NBP2-34962) and biotinylated anti-NF-L antibody (NFL/736) were purchased from Novus Biologicals (Bio-Techne, Milano, Italy). Monoclonal anti-NF-L (DA2) and anti-IL-6 (677B6A2) antibodies, and NeutrAvidin protein (31000) were purchased from Thermo Fischer Scientific (Life Technologies Italia, Monza, Italy). Recombinant human NF-L (ab224840), IL-6, and IL-1 proteins were purchased from Abcam (Prodotti Gianni, Milano, Italy), ReliaTech (Vinci-Biochem, Vinci, Italy), and AdipoGen Life Sciences (Vinci-Biochem, Vinci, Italy), respectively. Customized DNA oligonucleotide sequences were purchased from Integrated DNA Technologies (TEMA Ricerca, Bologna, Italy).

4.10. References

1. Fu, Y. *et al.* Ultrasensitive Detection of Ribonucleic Acid Biomarkers Using Portable Sensing Platforms Based on Organic Electrochemical Transistors. *Anal Chem* **93**, 14359–14364 (2021).

2. Macchia, E. *et al.* Ultra-sensitive protein detection with organic electrochemical transistors printed on plastic substrates. *Flexible and Printed Electronics* **3**, 034002 (2018).

3. Berto, M. *et al.* EGOFET Peptide Aptasensor for Label-Free Detection of Inflammatory Cytokines in Complex Fluids. *Adv Biosyst* **2**, 1700072 (2018).

4. Park, J. & Kim, M. Strategies in Protein Immobilization on a Gold Surface. *Applied Science and Convergence Technology* **24**, 1–8 (2015).

5. Jung, Y., Jeong, J. Y. & Chung, B. H. Recent advances in immobilization methods of antibodies on solid supports. *Analyst* **133**, 697 (2008).

6. Kim, D. & Herr, A. E. Protein immobilization techniques for microfluidic assays. *Biomicrofluidics* **7**, 041501 (2013).

7. Bae, Y. M., Oh, B.-K., Lee, W., Lee, W. H. & Choi, J.-W. Study on orientation of immunoglobulin G on protein G layer. *Biosens Bioelectron* **21**, 103–110 (2005).

8. Casalini, S., Bortolotti, C. A., Leonardi, F. & Biscarini, F. Self-assembled monolayers in organic electronics. *Chem Soc Rev* **46**, 40–71 (2017).

9. Ostuni, E., Chapman, R. G., Holmlin, R. E., Takayama, S. & Whitesides, G. M. A Survey of Structure−Property Relationships of Surfaces that Resist the Adsorption of Protein. *Langmuir* **17**, 5605–5620 (2001).

10. Wilchek, M. & Bayer, E. A. [2] Introduction to avidin-biotin technology. in 5–13 (1990). doi:10.1016/0076-6879(90)84256-G.

11. Rusmini, F., Zhong, Z. & Feijen, J. Protein Immobilization Strategies for Protein Biochips. *Biomacromolecules* **8**, 1775–1789 (2007).

12. Dundas, C. M., Demonte, D. & Park, S. Streptavidin–biotin technology: improvements and innovations in chemical and biological applications. *Appl Microbiol Biotechnol* **97**, 9343–9353 (2013).

13. You, C., Bhagawati, M., Brecht, A. & Piehler, J. Affinity capturing for targeting proteins into micro and nanostructures. *Anal Bioanal Chem* **393**, 1563–1570 (2009).

14. Ladd, J. *et al.* DNA-Directed Protein Immobilization on Mixed Self-Assembled Monolayers via a Streptavidin Bridge. *Langmuir* **20**, 8090–8095 (2004).

15. Larsson, C., Rodahl, M. & Höök, F. Characterization of DNA Immobilization and Subsequent Hybridization on a 2D Arrangement of Streptavidin on a Biotin-Modified Lipid Bilayer Supported on SiO $_2$. *Anal Chem* **75**, 5080–5087 (2003).

16. Smith, C. L., Milea, J. S. & Nguyen, G. H. Immobilization of Nucleic Acids Using Biotin-Strept(avidin) Systems. in 63–90 (2005). doi:10.1007/128_017.

17. Elgrishi, N. *et al.* A Practical Beginner's Guide to Cyclic Voltammetry. *J Chem Educ* **95**, 197–206 (2018).

18. Zeng, Y. *et al.* Recent advances in surface plasmon resonance imaging: detection speed, sensitivity, and portability. *Nanophotonics* **6**, 1017–1030 (2017).

19. Gordon, J. G. & Ernst, S. Surface plasmons as a probe of the electrochemical interface. *Surf Sci* **101**, 499–506 (1980).

20. Liedberg, B., Nylander, C. & Lunström, I. Surface plasmon resonance for gas detection and biosensing. *Sensors and Actuators* **4**, 299–304 (1983).

21. Kotlarek, D. *et al.* Surface plasmon resonance-based aptasensor for direct monitoring of thrombin in a minimally processed human blood. *Sens Actuators B Chem* **320**, 128380 (2020).

22. Masson, J.-F. Surface Plasmon Resonance Clinical Biosensors for Medical Diagnostics. *ACS Sens* **2**, 16–30 (2017).

23. Homola, J. Surface Plasmon Resonance Sensors for Detection of Chemical and Biological Species. *Chem Rev* **108**, 462–493 (2008).

24. https://cmi.hms.harvard.edu/surface-plasmon-resonance (Accessed: April 2023).

25. Dostálek, J. & Knoll, W. Biosensors based on surface plasmon-enhanced fluorescence spectroscopy (Review). *Biointerphases* **3**, FD12–FD22 (2008).

26. Liebermann, T. & Knoll, W. Surface-plasmon field-enhanced fluorescence spectroscopy. *Colloids Surf A Physicochem Eng Asp* **171**, 115–130 (2000).

27. Fujiki, A. *et al.* Enhanced fluorescence by surface plasmon coupling of Au nanoparticles in an organic electroluminescence diode. *Appl Phys Lett* **96**, 043307 (2010).

28. Toma, M. & Tawa, K. Polydopamine Thin Films as Protein Linker Layer for Sensitive Detection of Interleukin-6 by Surface Plasmon Enhanced Fluorescence Spectroscopy. *ACS Appl Mater Interfaces* **8**, 22032–22038 (2016).

29. Riedel, T. *et al.* Plasmonic Hepatitis B Biosensor for the Analysis of Clinical Saliva. *Anal Chem* **89**, 2972–2977 (2017).

30. Knoll, W. *et al.* Comparing Surface Plasmon-Optical and Electronic Immuno-Sensing of Affinity Interactions—A Case Study. *Chemosensors* **9**, 11 (2021).

31. Schmidt, K. *et al.* Rolling Circle Amplification Tailored for Plasmonic Biosensors: From Ensemble to Single-Molecule Detection. *ACS Appl Mater Interfaces* **14**, 55017–55027 (2022).

32. Hageneder, S., Bauch, M. & Dostalek, J. Plasmonically amplified bioassay – Total internal reflection fluorescence vs. epifluorescence geometry. *Talanta* **156–157**, 225–231 (2016).

33. Yildizhan, Y. *et al.* FO-SPR biosensor calibrated with recombinant extracellular vesicles enables specific and sensitive detection directly in complex matrices. *J Extracell Vesicles* **10**, (2021).

34. Jorgenson, R. C. & Yee, S. S. A fiber-optic chemical sensor based on surface plasmon resonance. *Sens Actuators B Chem* **12**, 213–220 (1993).

35. Leung, A., Shankar, P. M. & Mutharasan, R. A review of fiber-optic biosensors. *Sens Actuators B Chem* **125**, 688–703 (2007).

36. Liu, W. *et al.* Specialty optical fibers and 2D materials for sensitivity enhancement of fiber optic SPR sensors: A review. *Opt Laser Technol* **152**, 108167 (2022).

37. Fiber optic surface plasmon resonance. Available at: https://foxbiosystems.com/fiber-optic-surface-plasmon-resonance-fox-biosystems/ (Accessed: February 2023).

38. Hasler, R. *et al.* Field-Effect Transistor with a Plasmonic Fiber Optic Gate Electrode as a Multivariable Biosensor Device. *ACS Sens* **7**, 504–512 (2022).

39. Binnig, G., Quate, C. F. & Gerber, Ch. Atomic Force Microscope. *Phys Rev Lett* **56**, 930–933 (1986).

40. Raghavendra, P. & Pullaiah, T. Biomedical Imaging Role in Cellular and Molecular Diagnostics. in *Advances in Cell and Molecular Diagnostics* 85–111 (Elsevier, 2018). doi:10.1016/B978-0-12-813679-9.00004-X.

41. http://gwyddion.net/ (Accessed: November 2022).

42. de Biasi, S. *et al.* Mitochondrial functionality and metabolism in T cells from progressive multiple sclerosis patients. *Eur J Immunol* **49**, 2204–2221 (2019).

43. Trengove, N. J., Langton, S. R. & Stacey, M. C. Biochemical analysis of wound fluid from nonhealing and healing chronic leg ulcers. *Wound Repair and Regeneration* **4**, 234–239 (1996).

44. Tlili, C., Myung, N. V., Shetty, V. & Mulchandani, A. Label-free, chemiresistor immunosensor for stress biomarker cortisol in saliva. *Biosens Bioelectron* **26**, 4382–4386 (2011).

45. Rathish, R. J. *et al*. Corrosion Behaviour of Metals in Artificial Sweat~!2010-01-04~!2010-02-25~!2010-05-06~! *The Open Corrosion Journal* **3**, 38–44 (2010).

Chapter 5.
Characterization of electrolyte-gated organic transistors

The following chapter describes the electrical characterization of electrolyte-gated organic transistors. The electrical performance of the transistors fabricated following different strategies is discussed in detail, with a focus on the investigation of the device stability and reproducibility. Moreover, the performance of the transistors in different electrolytes, from buffered solutions to blood plasma, is discussed.

5.1. Introduction

Over the past few years, significant progress has been achieved in the field of organic bioelectronic sensors. The development of new materials and device architectures, together with the advances in sensing strategies, have led to the emergence of new versatile bioelectronic platforms as promising candidates for biosensing applications in the clinical field. Among them, EGOTs are rapidly emerging as strong competitors to the conventional immunoassays. EGOTs exhibit unique characteristics, such as the high transconductance, label-free detection, and capability of working in liquid environment, which makes them an attractive tool for immunosensing applications. The fact that EGOTs can be operated in liquid medium offers two major advantages: the possibility of using the biological fluid of interest as electrolyte, and the possibility of working at a low operational voltage (< 1 V), which is an essential requisite when working with biological analytes. The use of EGOTs as biosensing tool has been widely investigated, and a large number of studies can be found in literature reporting the development of OECT or EGOFET-based biosensors for the ultrasensitive detection of environmental or clinically relevant biomarkers, such as inflammatory markers[1,2], nucleic acids[3,4], metabolites[5,6], antibodies[7], and even bacteria[8] and viruses[9].

In this chapter, the development of EGOT-based sensors for biosensing applications is described. In the first part, the fabrication and optimization of EGOFETs is discussed, while the second part of the chapter covers the development of OECTs. A focus is given to the optimization of the transistors in terms of electrical performance, device stability, and reproducibility. In addition, the response of the transistors to different solutions, including blood plasma, is investigated. The final architecture consisted of a top-gated EGOT, where an Au wire, used as gate electrode, was immersed in the electrolyte, as depicted in Figure 5.1.

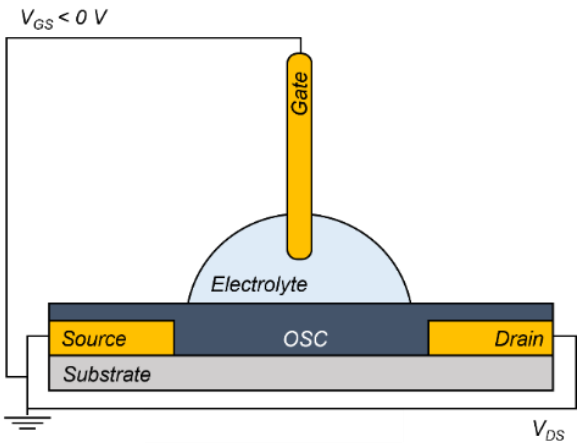

Figure 5.1. Schematic illustration of the EGOFET device, comprising the electrical connections.

5.2. Electrical characterization of electrolyte-gated organic field-effect transistors

EGOFETs were fabricated using quartz test patterns with interdigitated Au drain and source electrodes and TIPS-pentacene was used as the OSC. Three different fabrication procedures were investigated, combining OSC deposition with a thermal annealing (*Protocol 1*), or the deposition by spin coating followed by a solvent vapour (*Protocol 2*) or vacuum annealing (*Protocol 3*).

Probably the most widely used annealing for OFETs is the thermal annealing. The exposure of OFETs to increased temperatures has been reported to increase the molecular ordering and crystallinity of the film, improving the electrical properties of the transistors[10–12]. Another method that is gaining popularity is the solvent vapour annealing (SVA), as it is believed to improve the electrical performance of OFETs by controlling the morphology of the OSC film growth[13]. SVA was described for the first time in 2006[14], when Dickey and co-workers observed a morphological and structural rearrangement in the OSC film following the exposition of the transistors to a solvent vapour-rich ambient. As reported by the authors, the induced changes in the film morphology were correlated to a drastic improvement of the device performance. Since then, several groups reported the fabrication of OFETs with highly uniform and crystalline films and enhanced electrical performance by submitting the transistor to a SVA[12,15–17]. The second annealing method investigated in this thesis consisted in the drying of the solvent under vacuum conditions.

Once the transistor fabrication was completed, the film crystallization was observed under an optical microscope (Figure 5.2), and the electrical performance of the transistors was evaluated in terms of maximum transconductance, threshold voltage, and current *on/off* ratio. The results of the electrical evaluation are reported in Table 5.1. In order to mimic the physiological conditions, a phosphate buffer (50 mM PB, pH 7.4) was used as electrolyte during the electrical characterization.

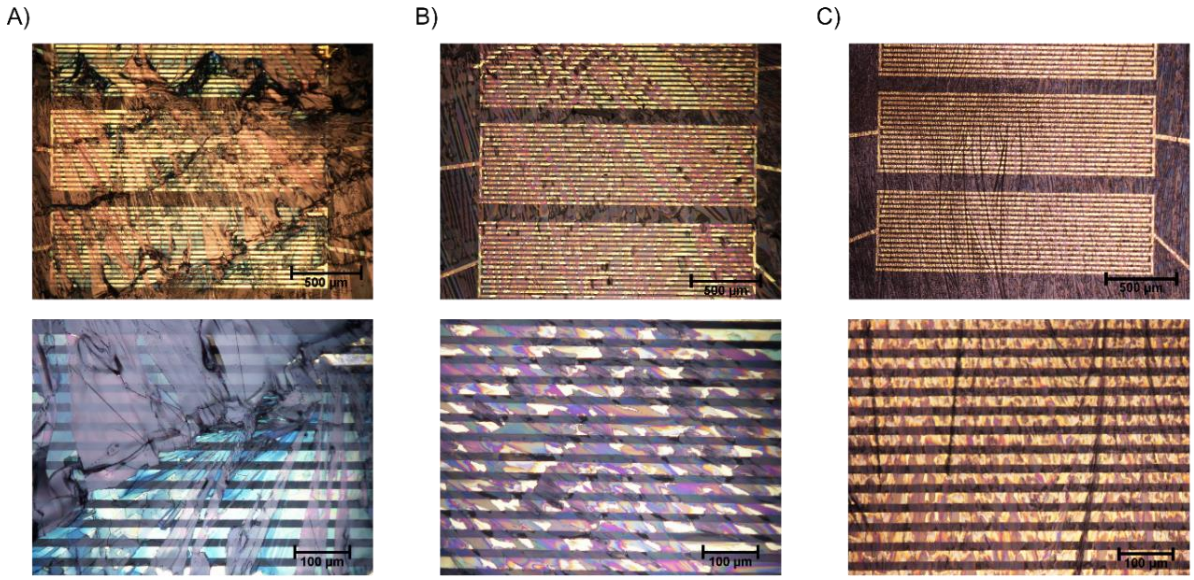

Figure 5.2. Optical microscopy images of TIPS-pentacene crystal film formation on the quartz substrate following different OSC deposition techniques A) *Protocol 1*, drop casting with heat annealing, B) *Protocol 2*, spin coating with heat, solvent vapour annealing, and C) *Protocol 3*, spin coating and vacuum annealing. The images are taken at different magnifications, 5x (top) and 20x (bottom).

Table 5.1. Comparison of the electrical performance of the EGOFET devices fabricated using the different protocols described. The results are expressed as the mean ± SD (standard deviation) of three different transistors.

	$g_{m,max}$ (S)	V_{th} (V)	I_{on}/I_{off}
Protocol 1	$1.0\times10^{-6} \pm 0.3\times10^{-6}$	-0.28 ± 0.08	$2\times10^{2} \pm 3\times10^{2}$
Protocol 2	$5.1\times10^{-6} \pm 0.9\times10^{-6}$	-0.28 ± 0.01	$1.5\times10^{3} \pm 0.1\times10^{3}$
Protocol 3	$2.6\times10^{-6} \pm 0.6\times10^{-6}$	-0.29 ± 0.01	$1.5\times10^{3} \pm 0.5\times10^{3}$

Because of its simplicity, the first method for OSC deposition investigated was drop casting (*Protocol 1*). As illustrated in Figure 5.2 (panel A), the film was composed by big TIPS-pentacene crystals, covering all the interdigitated area. However, the crystal film was not uniform and presented many grain boundaries, which have been associated with charge carrier trapping and decreased electrical performance[18,19]. As expected, the transistors showed poor electrical performance (Table 5.1), with low transconductance and low on/off current ratio. Moreover, as it can be concluded from the SD, the deposition of the OSC by drop casting exhibited poor reproducibility.

Thus, with the aim of improving the crystal film formation, in the other two fabrication strategies (*Protocol 2* and *Protocol 3*), the deposition of the OSC was done by spin coating. For the OSC deposition, the same spin coater parameters were used for both strategies, varying the fabrication protocol only in the annealing step. In *Protocol 2*, the OSC deposition was followed by a combined thermal and solvent vapour annealing, while in *Protocol 3*, the annealing was performed under vacuum.

As reported in Figure 5.2, both protocols led to the formation of a uniform OSC film, with large and continuous crystals covering the whole interdigitated area. Accordingly, both strategies yielded satisfactory results in terms of electrical performance of the transistors, achieving high transconductance and on/off current ratio (Table 5.1). Nonetheless, transistors fabricated following *Protocol 2* showed a maximum transconductance two times higher when compared to *Protocol 3*, and therefore, it was the strategy of choice for the fabrication of EGOFET-based biosensors. During the electrical measurements, hysteresis and the gate leakage current (I_{GS}) were continuously monitored. As showed in Figure 5.3, the leakage current between the transistor and the gate was negligible, as it is invariably two orders of magnitude lower than the drain current, and no hysteresis was observed.

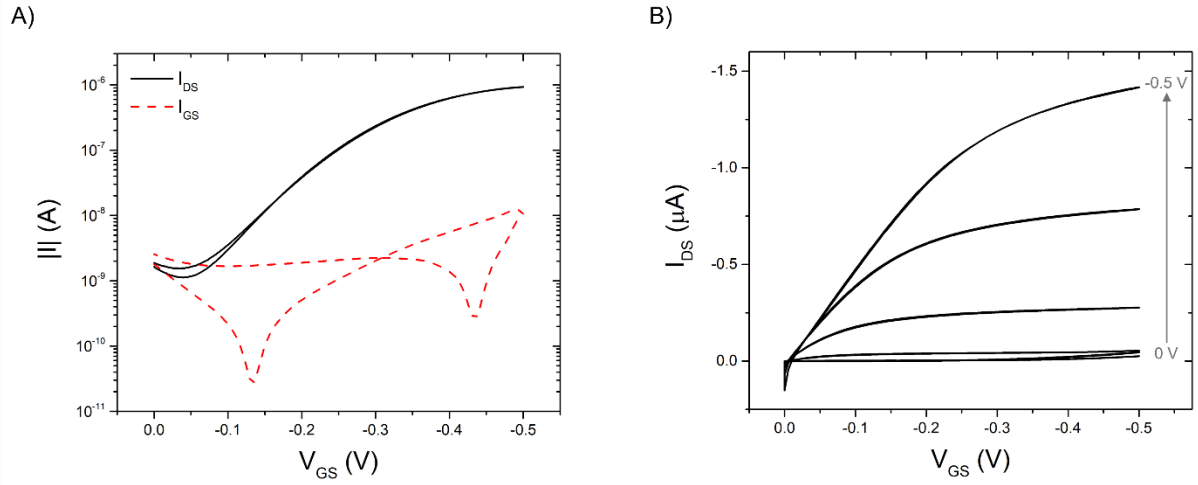

Figure 5.3. Current-voltage characteristics of an EGOFET fabricated following *Protocol 2*. Typical transfer (A) and output (B) curves are illustrated. Solid lines (black curves) represent the drain current, I_{DS}, while dashed lines (red curves) correspond to the gate leakage current, I_{GS}.

5.3. Organic electrochemical transistors

The second EGOT architecture used in this thesis work are OECTs. The transistors were fabricated by spin coating the OSC DPP-DTT on the substrate, followed by a thermal annealing step. Once the fabrication was completed, the devices were immersed in a phosphate buffer (50 mM PB, pH 7.4) for at least 12 hours. Since one of the main goals of this thesis work was development of organic transistor-based biosensors to be used in biological fluids, the electrical performance of the fabricated OECTs was assessed in different solutions. In particular, the transistors were electrically characterized in PBS, in several artificial solutions mimicking physiological fluids (sweat, saliva, and wound exudate), and in blood plasma.

During the electrical characterization, the devices were first stabilized: transfer curves were repeatedly recorded by applying a sweeping V_{GS} potential from 0.0 to -0.7 V, while maintaining a constant V_{DS} of -0.1 V. After 15 measurements, the electrolyte was replaced by a fresh solution and the measurement was restarted. In order to ensure the stabilization of the device, this procedure was repeated for 3 times. In Figure 5.4, representative transfer curves recorded in PBS (panel A) and blood plasma (panel B) are exhibited, demonstrating the successful operation of OECTs working in the accumulation in mode. Although the successful performance of EGOTs in biological solutions, including blood[20], plasma[20], serum[21–23], sweat[24,25], or saliva[23,26,27], has been previously reported, so far, the behaviour of a DPP-DTT-based transistor exposed to biological fluids has not been described.

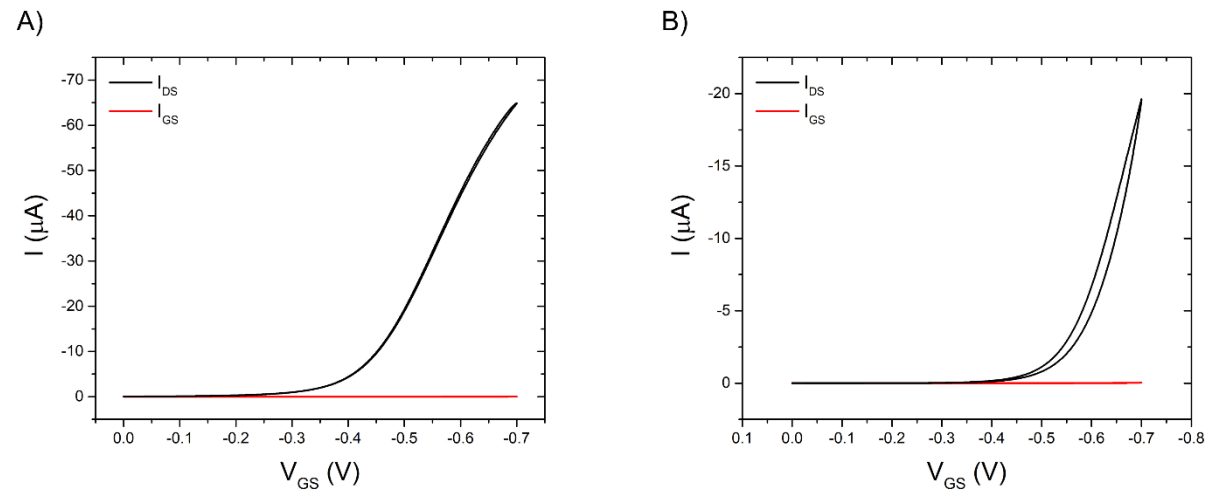

Figure 5.4. Representative transfer curves of a DPP-DTT-based transistor recorded in A) PBS, and B) blood plasma, at a fixed V_{DS} of -0.1 V.

The transistors presented good electrical performance in all the solutions tested, even in a highly complex biological matrix as it is blood plasma. The electrical performance of the devices in the different solutions was assessed in terms of the typical figures of merit of EGOTs: $g_{m,max}$, V_{th}, and *on/off* current ratio, extracted from the transfer curves (Figure 5.5). In addition, the hysteresis and the gate leakage current were continuously monitored during the experiments and the stability and reproducibility of the transistors were assessed.

In all the solutions tested, high values of maximum drain current ($I_{DS,max}$), reaching tens of μA, usually, were achieved, and minimal hysteresis and negligible gate leakage current were observed (Figure 5.4). As well, as reported in Figure 5.5 (panel A), all the transistors showed high transconductance, although a slight decrease in $g_{m,max}$ was observed in the transistors exposed to artificial saliva, artificial wound exudate and plasma. Interestingly, in artificial wound exudate and plasma, the two solutions containing proteins, the gate potential at which the $g_{m,max}$ was achieved was considerably higher, almost 100 mV, when compared to the other solutions tested. Similarly, transistors exposed to artificial wound exudate and plasma presented more negative values for V_{th}, around -0.55 V and 0.60 V respectively, in comparison to PBS, artificial sweat and artificial saliva, which presented values of V_{th} between -0.40 V and -0.45 V, approximately. This difference in the transistor performance between PBS and blood plasma is not surprising, as, even though the pH and ionic strength of both solutions is very similar, the composition is very different. As well, a similar behaviour has been observed in a previous work from our group[28]. In this study, a decrease in $I_{DS,max}$ as well as in V_{th} was reported upon changing the electrolyte solution from a phosphate buffer to a complex medium (cell culture medium RPMI-1640 + 10% fetal bovine serum, FBS). The change in the electrical performance of the transistor was attributed to the composition of the complex medium, which includes charged and high-molecular weight molecules, which would have an impact in the electrical double layer, reflected in a decreased areal charged density[28].

A drastic increase, of almost two orders of magnitude, in the *on/off* current ratio was observed in the transistors characterized in artificial wound exudate and plasma (Figure 5.5, panel C). Curiously, the increase in I_{on}/I_{off} ratio was not caused by an increase of I_{on}, but by a radical decrease in I_{off} current. Taking into account the composition complexity of both solutions, the decrease in the I_{off} current might be ascribed to a potential non-specific protein absorption on the Au surface, increasing in this way the passivation of the gate electrode. Moreover, as

reported in Figure 5.5 (panel D), the transistors showed minimal hysteresis (< 15%) in all the solutions tested, except for plasma, where a slightly bigger hysteresis was observed (~20%).

Interestingly, the transistors characterized in artificial sweat presented very similar performance to the ones characterized in PBS, indicating that neither the pH nor the ionic strength of the solutions have a noticeable effect on the device performance.

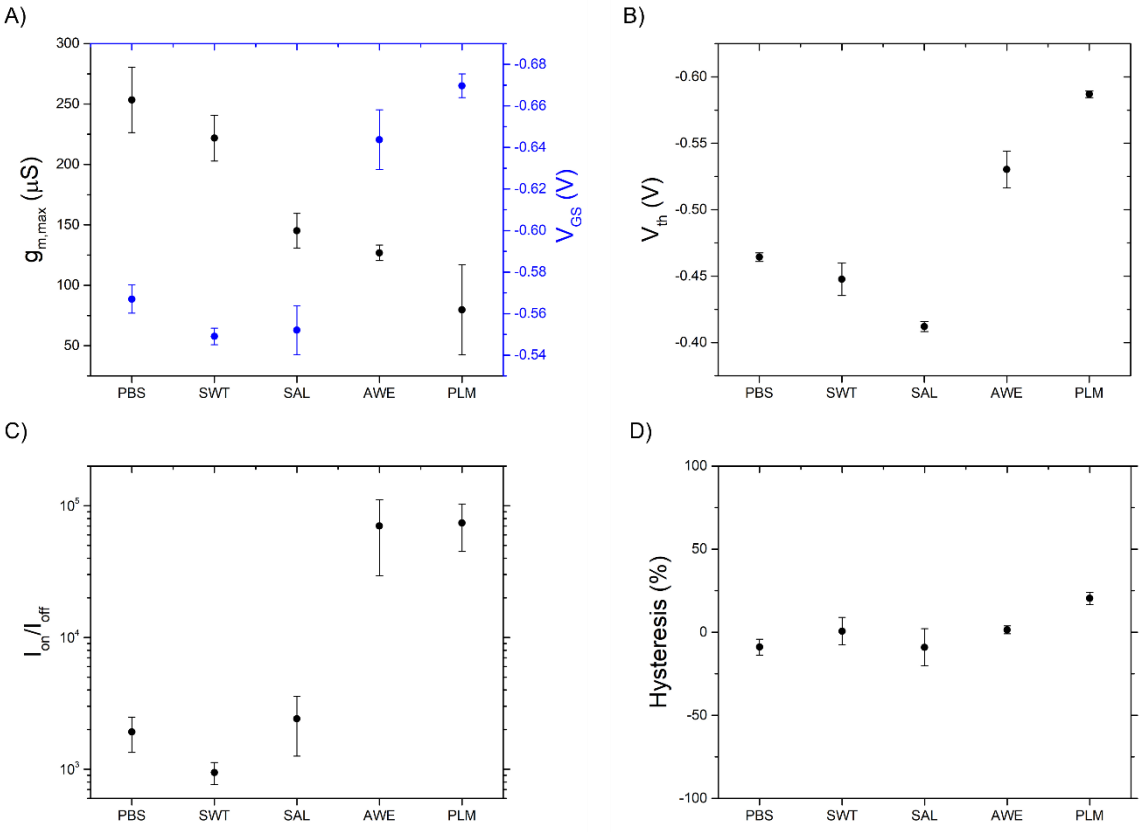

Figure 5.5. Assessment of the electrical performance, in terms of $g_{m,max}$ and the gate potential at which is achieved (A), V_{th} (B), I_{on}/I_{off} ratio (C), and hysteresis (D), of DPP-DTT-based transistors tested in PBS, artificial sweat (SWT), artificial saliva (SAL), artificial wound exudate (AWE), and blood plasma (PLM). The results are shown as the mean ± SE (standard error) of 3 different devices.

Altogether, all these observations indicate that the fabricated DPP-DTT-based transistors show optimal performance, not only in a buffered solution but also in more complex solutions, resembling biological fluids, as well as in whole blood plasma. However, in order to be used as biosensors, besides good electrical properties, the transistors must show good stability and reproducibility. Therefore, after proving the successful operation of the transistors, even in complex solutions, the stability and reproducibility of the devices was assessed.

The device stability was investigated mimicking a sensing experiment. To this aim, continuous transfer curves were recorded until reaching stabilization (15 measurements), and then, the electrolyte was replaced by a fresh solution and the measurement was restarted. This was repeated for 3 times, and the response of the transistor to the changes in the electrolyte was investigated in terms of variations in the drain current. The stability of the transistors, expressed as the normalized variation in the maximum drain current upon changing the solution, averaged of 3 experiments, is reported in Table 5.2. As it can be seen, optimal stability was observed in all the solutions tested, presenting variation always lower than 5%. This data indicates that, when performing sensing experiments in PBS, for instance, variations higher than 1% can be safely ascribed to binding events, while variations lower than 1% should be examined carefully, as they might result merely from fluctuations in the current, and not be related to binding processes.

In addition, the transistors showed satisfactory results in terms of reproducibility, with a device-to-device variability lower than 10% in all the solutions tested. The reproducibility was calculated as the variability of the device response, defined as $I_{DS,max}$ normalized against $g_{m,max}$, within 3 different devices.

Table 5.2. Evaluation of the stability and reproducibility of the transistors in different solutions.

Solution	*Stability (%)*	*Reproducibility (%)*
PBS	99	98
Art. Sweat	96	96
Art. Saliva	97	94
Art. Wound exudate	96	94
Plasma	98	93

Furthermore, the device response to small potential changes at the gate electrode was examined. To this aim, a fixed gate potential (V_{GS} at which $g_m = g_{m,max}$) was applied and the drain current was recorded as a function of time. Then, small potential pulses were applied to the gate (ΔV_{GS} = -100 μV, -50 μV, and -10 μV), resulting in noticeable changes in the drain

current, as illustrated in Figure 5.6. The transistors proved to be sensitive to detect potential changes as low as ΔV_{GS} = -10 µV, providing a fast response in all the solutions tested.

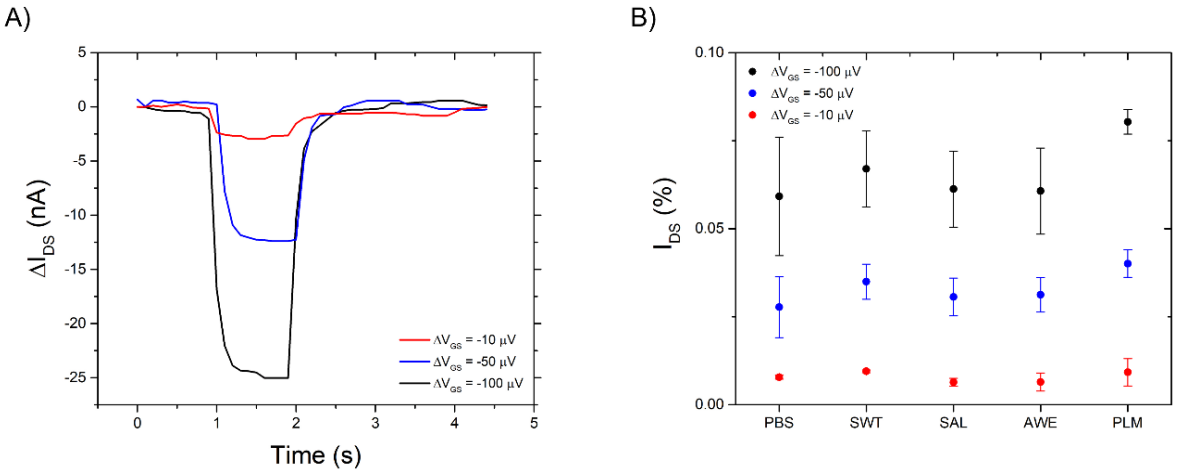

Figure 5.6. Analysis of the drain current, I_{DS}, variation upon the application of small potential changes to the gate, under a constant V_{DS} of -0.1 V. A) Representative example using PBS as electrolyte. B) Normalized change in the drain current for all the solutions tested. Data is shown as the mean ± SE of three independent experiments.

5.4. References

1. Parkula, V. *et al.* Harnessing Selectivity and Sensitivity in Electronic Biosensing: A Novel Lab-on-Chip Multigate Organic Transistor. *Anal Chem* **92**, 9330–9337 (2020).

2. Manco Urbina, P. A. *et al.* Physical insights from the Frumkin isotherm applied to electrolyte gated organic transistors as protein biosensors. *J Mater Chem C Mater* **9**, 10965–10974 (2021).

3. Selvaraj, M. *et al.* Label free detection of miRNA-21 with electrolyte gated organic field effect transistors (EGOFETs). *Biosens Bioelectron* **182**, 113144 (2021).

4. Sensi, M. *et al.* Monitoring DNA Hybridization with Organic Electrochemical Transistors Functionalized with Polydopamine. *Macromol Mater Eng* **307**, 2100880 (2022).

5. Diacci, C. *et al.* Diurnal in vivo xylem sap glucose and sucrose monitoring using implantable organic electrochemical transistor sensors. *iScience* **24**, 101966 (2021).

6. Berto, M. *et al.* Label free urea biosensor based on organic electrochemical transistors. *Flexible and Printed Electronics* **3**, 024001 (2018).

7. Sensi, M. *et al.* Anti-drug antibody detection with label-free electrolyte-gated organic field-effect transistors. *Chemical Communications* **57**, 367–370 (2021).

8. He, R.-X. *et al.* Detection of bacteria with organic electrochemical transistors. *J Mater Chem* **22**, 22072 (2012).

9. Berto, M. *et al.* Label free detection of plant viruses with organic transistor biosensors. *Sens Actuators B Chem* **281**, 150–156 (2019).

10. Bae, J.-H. *et al.* Thermal annealing effect on the crack development and the stability of 6,13-bis(triisopropylsilylethynyl)-pentacene field-effect transistors with a solution-processed polymer insulator. *Org Electron* **11**, 784–788 (2010).

11. Yang, F. *et al.* Effect of In Situ Annealing Treatment on the Mobility and Morphology of TIPS-Pentacene-Based Organic Field-Effect Transistors. *Nanoscale Res Lett* **12**, 503 (2017).

12. Kim, G. W., Kwon, E. H., Kim, M. & Park, Y. D. Uniform and Reliable Dip-Coated Conjugated Polymers for Organic Transistors as Obtained by Solvent Vapor Annealing. *The Journal of Physical Chemistry C* **123**, 23255–23263 (2019).

13. de Luca, G. *et al.* Solvent vapour annealing of organic thin films: controlling the self-assembly of functional systems across multiple length scales. *J Mater Chem* **20**, 2493 (2010).

14. Dickey, K. C., Anthony, J. E. & Loo, Y.-L. Improving Organic Thin-Film Transistor Performance through Solvent-Vapor Annealing of Solution-Processable Triethylsilylethynyl Anthradithiophene. *Advanced Materials* **18**, 1721–1726 (2006).

15. Hou, S., Zhuang, X., Fan, H. & Yu, J. Grain Boundary Control of Organic Semiconductors via Solvent Vapor Annealing for High-Sensitivity NO2 Detection. *Sensors* **21**, 226 (2021).

16. Khim, D. *et al.* High Performance and Stable N-Channel Organic Field-Effect Transistors by Patterned Solvent-Vapor Annealing. *ACS Appl Mater Interfaces* **5**, 10745–10752 (2013).

17. Kim, J., Park, C., Park, J. E., Chu, K. & Choi, H. C. Vertical Crystallization of C_{60} Nanowires by Solvent Vapor Annealing Process. *ACS Nano* **7**, 9122–9128 (2013).

18. Tello, M., Chiesa, M., Duffy, C. M. & Sirringhaus, H. Charge Trapping in Intergrain Regions of Pentacene Thin Film Transistors. *Adv Funct Mater* **18**, 3907–3913 (2008).

19. Mas-Torrent, M. *et al.* Correlation between Crystal Structure and Mobility in Organic Field-Effect Transistors Based on Single Crystals of Tetrathiafulvalene Derivatives. *J Am Chem Soc* **126**, 8546–8553 (2004).

20. Preziosi, V. *et al.* Organic electrochemical transistors as novel biosensing platforms to study the electrical response of whole blood and plasma. *J Mater Chem B* **10**, 87–95 (2022).

21. Wustoni, S. *et al.* Membrane-Free Detection of Metal Cations with an Organic Electrochemical Transistor. *Adv Funct Mater* **29**, 1904403 (2019).

22. Magliulo, M. *et al.* Label-free C-reactive protein electronic detection with an electrolyte-gated organic field-effect transistor-based immunosensor. *Anal Bioanal Chem* **408**, 3943–3952 (2016).

23. Liu, H. *et al.* Ultrafast, sensitive, and portable detection of COVID-19 IgG using flexible organic electrochemical transistors. *Sci Adv* **7**, (2021).

24. Parlak, O., Keene, S. T., Marais, A., Curto, V. F. & Salleo, A. Molecularly selective nanoporous membrane-based wearable organic electrochemical device for noninvasive cortisol sensing. *Sci Adv* **4**, (2018).

25. Coppedè, N. *et al.* Human stress monitoring through an organic cotton-fiber biosensor. *J. Mater. Chem. B* **2**, 5620–5626 (2014).

26. Pappa, A.-M. *et al.* Organic Transistor Arrays Integrated with Finger-Powered Microfluidics for Multianalyte Saliva Testing. *Adv Healthc Mater* **5**, 2295–2302 (2016).

27. Liao, C., Mak, C., Zhang, M., Chan, H. L. W. & Yan, F. Flexible Organic Electrochemical Transistors for Highly Selective Enzyme Biosensors and Used for Saliva Testing. *Advanced Materials* **27**, 676–681 (2015).

28. Berto, M. *et al.* EGOFET Peptide Aptasensor for Label-Free Detection of Inflammatory Cytokines in Complex Fluids. *Adv Biosyst* **2**, 1700072 (2018).

Chapter 6.
Sensing NF-L with an EGOFET-based biosensor

This chapter covers the development of an EGOFET-based biosensor for serving as biosensor for the detection of the multiple sclerosis biomarker neurofilament light chain. The gate functionalization procedure, as well as the results from the sensing experiments, are carefully examined. Furthermore, the analysis of the data is discussed in detail.

6.1. Introduction

Neurofilament light chain is a structural protein present in neurons that has emerged as a promising biomarker of multiple sclerosis[1,2]. In recent years, a large number of studies has been published reporting a link between increased NF-L levels in MS and disease progression[3–7]. Yet, the accurate quantification of NF-L in bodily fluids remains challenging. Cerebrospinal fluid analysis provides valuable information and, as NF-L levels are significantly higher when compared to plasma or serum, the results are more accurate. However, CSF cannot be used for repeated monitoring and, therefore, blood-derived samples are preferred for NF-L detection. Recently, highly sensitive methods based on single-molecule arrays have been developed for NF-L detection in biological fluids[3–6]. These methods present high sensitivity and specificity, but also some limiting factors, as they are expensive, time consuming, and require specialized equipment and trained personnel, as well as enzymatic or fluorescent labelling.

Within this framework, the field of organic electronics and, in particular, organic electronic-based devices, has experienced a huge progress in the last years. The development of highly sensitive transistor-based sensors, such as EGOFETs or OECTs, for biosensing applications places this technology as a strong competitor to the conventional optical assays[8–11].

In this chapter, the development of an EGOFET-based biosensor for the detection of NF-L is described. The transistor was turned into an immunosensor by endowing the gate electrode with biorecognition capability. This was achieved by immobilizing specific anti-NF-L antibodies on the gate surface, with a controlled and uniform orientation, increasing the probability of binding events. Once the fabrication of the EGOFET immunosensor was completed, its biorecognition capability was tested in buffer solutions containing increasing concentrations of the target NF-L protein.

6.2. Characterization of the gate functionalization strategy

In an attempt of increasing the probability of binding events at the gate surface, specific anti-NF-L antibodies were immobilized at the gate electrode with controlled and potentially uniform orientation. This was achieved by using protein G for antibody immobilization. As reported by Bae et al in 2005[12], protein G leads to a uniform antibody immobilization, with the proper orientation for antigen binding. In this study, the authors presented an extensive

characterization of antibody immobilization comparing two different strategies, 11-mercaptoundecanoic acid (11-MUA) self-assembled monolayer and thiolated protein G. The results from the surface plasmon resonance analysis showed a successful antibody immobilization achieved with both methods, with a similar surface coverage. However, when the surface was examined by atomic force microscopy, it was observed that the antibody immobilization driven by 11-MUA induced and increase in the surface roughness, that the authors attributed to the different orientations of the immobilized antibodies. Conversely, protein G-mediated antibody immobilization did not cause significant changes in the surface topology, indicating that the antibodies were immobilized on the surface with a constant-oriented configuration, in which the Fc region of the antibodies is bound to the protein G, while the Fab region is oriented away from the substrate. On this basis, the use of protein G for an improved antibody immobilization has been widely exploited, and its application has been reported for different immunoassays and biosensors[13–15]. Moreover, antibody immobilization using protein G has been previously employed in our group for the selective detection of proteins and viruses[16–18].

In this work, the functionalization strategy consisted of the formation of a protein G monolayer on the gate electrode, followed by the immobilization of anti-NF-L antibodies with a proper orientation. In a last step, the gate surface was passivated using an OEG SAM. Poly-EG and its derivatives are known to present antifouling properties[19]. The suggested mechanism is that, upon the molecule rearrangement, the strong hydration of the SAM acts as a barrier to protein adsorption[20]. Therefore, OEG was used in this work in an attempt to reduce non-specific binding. The schematics of the EGOFET-based biosensor, with an inset of the functionalized gate electrode, is illustrated in Figure 6.1.

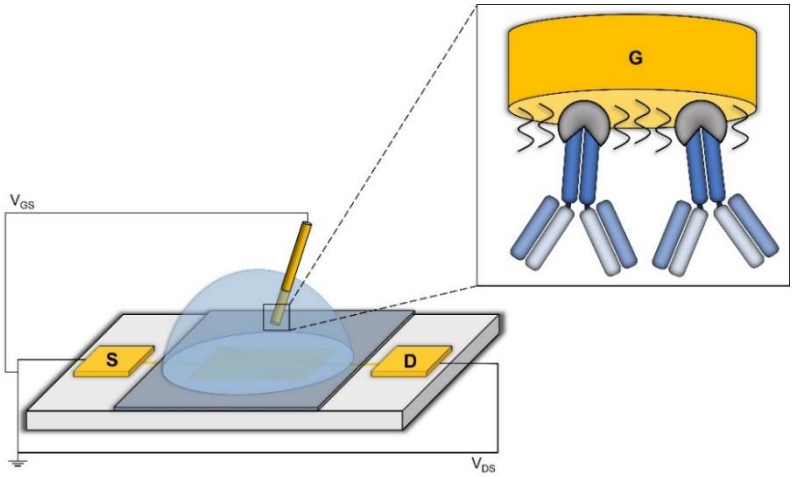

Figure 6.1. Schematic representation of the EGOFET-based biosensor, including the electrical connections, and a zoomed view of the functionalized gate electrode.

Every step of the gate functionalization protocol was monitored electrochemically and electrically. During the electrochemical characterization, cyclic voltammetry measurements were performed using the gate electrode as the working electrode. The electrical characterization was performed by recording transfer curves following every functionalization step.

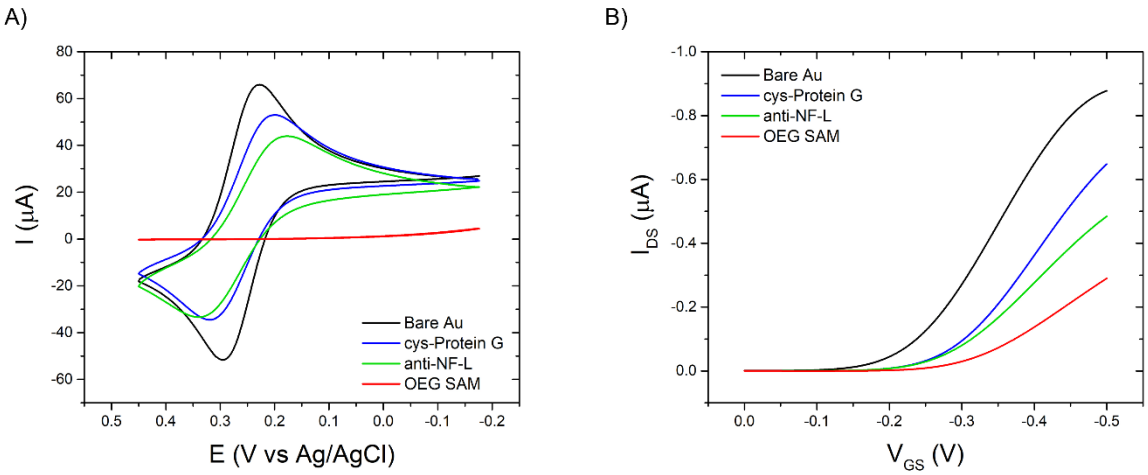

Figure 6.2. Electrochemical (A) and electrical (B) characterization of the gate functionalization protocol. Cyclic voltammograms were recorded in 5 mM $K_3[Fe(CN)_6]$ in the presence of 1 M KCl at a scan rate of 50 mV/s. Transfer curves were acquired in a 50 mM phosphate buffer.

As it can be noted from the CV curves (Figure 6.2, panel A), after the first functionalization step, an increase in the peak-to-peak separation was observed (blue line), proving the successful adsorption of protein G onto the Au surface. As expected, the subsequent immobilization of the antibody did not cause significant changes in the CV curves (green line), as the binding occurs between the antibodies and the protein G, therefore, the non-functionalized Au area remains nearly unaltered. On the contrary, a radical change was observed following the last functionalization step: the faradaic response was completely inhibited as a consequence of the SAM formation (red line), indicating a total coverage of the Au gate surface.

From these measurements, the area of the Au gate electrode covered by the protein G/anti-NF-L complex was calculated by means of the Randles-Sevçick equation. The coverage was estimated to be 40 ± 4 %, a finding in line with previous results reported by our group[17,18].

In parallel, the gate functionalization process was also monitored electrically by recording transfer characteristics. Following each modification step, a progressive decrease in the drain

current was observed (Figure 6.2, panel B), which was correlated to a decrease in the faradaic response, indicating a gradual passivation of the Au gate electrode.

The transistors showed good electrical performance, in terms of the figures of merit investigated, even after the gate functionalization (Table 6.1). In particular, a decrease in maximum transconductance and the shift of the threshold voltage towards more negative potentials was observed after the gate functionalization. These observations were interpreted as a confirmation of the progressive passivation of the gate electrode upon functionalization. Furthermore, functionalized gate electrodes exhibited an increase of the on/off current ratio when compared to bare Au electrodes. The increase observed was a consequence of the decrease in the off current, which was ascribed to a decrease in the gate leakage current after the functionalization process.

Table 6.1. Electrical performance of the EGOFET-based biosensors before and after the gate functionalization. The results are expressed as the mean ± SD of the 11 sensors used during the sensing experiments.

	$g_{m,max}$ (S)	V_{th} (V)	I_{on}/I_{off}
Bare Au	$2.4\times10^{-6} \pm 0.9\times10^{-6}$	-0.31 ± 0.04	~1000
Functionalized Au	$2.1\times10^{-6} \pm 0.6\times10^{-6}$	-0.38 ± 0.03	~2000

6.3. Sensing NF-L with EGOFET-based biosensors

Once the gate functionalization strategy was successfully assessed, the EGOFET devices were tested as biosensors for the selective detection of NF-L in a wide dynamic range. To this aim, transfer curves were recorded in the -0.1 to -0.6 V potential window in a 50 mM phosphate buffer (pH 7.4) containing increasing concentrations of NF-L, ranging from 100 fM to 10 nM. The typical response of the EGOFETs to increasing [NF-L] is illustrated in Figure 6.3 (panel A): the drain current decreases monotonically following increasing concentrations of the target analyte. This concentration-dependent change in the drain current was ascribed to the binding of NF-L proteins to the corresponding antibodies immobilized on the gate.

The biosensor exhibited a fast response, within a few minutes, and showed good stability in time. The response of the biosensor was quantified as the normalized change in the drain current:

$$\frac{-\Delta I}{I_0} = \frac{I_{DS,n} - I_{DS,0}}{I_{DS,0}} \qquad \textit{(Eq. 6.1)}$$

where $I_{DS,n}$ is the drain current value at the nth NF-L concentration, and $I_{DS,0}$ is the drain current value in the absence of the analyte, i.e. [NF-L] = 0 M. This approach has been previously used to quantitatively assess the response of a biosensor by our groups and others[16,21–24]. Although $-\Delta I/I_0$ can be extracted at any V_{GS} value along the transfer curve, it has been reported in previous works by our group that the response of the biosensor is strongly dependent on the gate voltage at which $-\Delta I/I_0$ is calculated[18,25]. In particular, although the magnitude of the current change is higher when explored at more negative V_{GS} values, its normalized variation is significantly higher at V_{GS} values $\leq V_{th}$. Therefore, in this work, the response of the EGOFET biosensor was calculated at V_{GS} = -0.4 V (Figure 6.3, panel B).

Following the gate incubation with increasing concentrations of NF-L, the biosensor exhibited a monotonical increase in the response, which was attributed to the binding events between NF-L and its specific antibody occurring at the Au surface. For the lowest concentrations tested, i.e. [NF-L] ≤ 10 pM, a rapid increase in the response was observed, which was followed by a less steep increase, almost reaching a plateau in the intermediate range of concentrations ([NF-L] > 1 nM). Interestingly, a fast increase in the response was observed once again when the highest concentration, [NF-L] = 10 nM, was tested.

The observed trend of $-\Delta I/I_0$ versus [NF-L] could not be fitted by any of the classical equilibria binding models, such as Langmuir or Hill. Moreover, the particular distribution of the data suggested the concomitant presence of two simultaneous equilibria taking place at the gate/electrolyte interface. Therefore, to get a better understanding of the binding phenomena occurring at the gate surface, the observed experimental data was fitted to the liquid phase version of the Guggenheim-Anderson-De Boer (GAB) adsorption model.

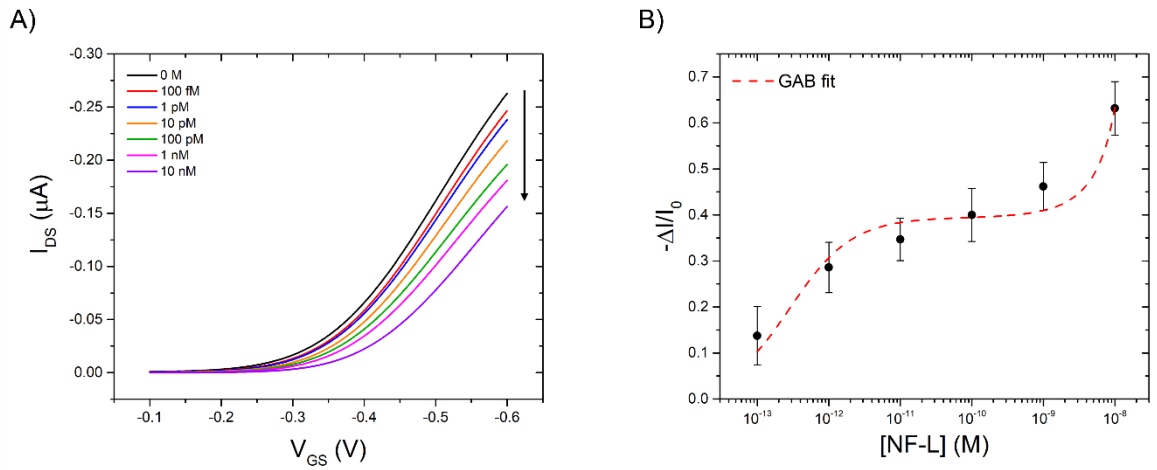

Figure 6.3. A) Typical transfer curve of the biosensor upon exposure to increasing [NF-L]. B) Biosensor dose curve, plotted as $-\Delta I/I_0$ versus Log[NF-L], calculated at V_{GS} = -0.4 V. Data are shown as the mean ± SE of 11 independent experiments; the highest concentration (10 nM) was tested in 8 replicates, while the lowest (100 fM), in 3.

The GAB isotherm is a three-parameter, multilayer adsorption model that, in contrast to the classical ligand-binding models, assumes that the adsorption is not limited to a certain level, i.e., the formation of a protein monolayer. Instead, the GAB model described the presence of two or more different equilibrium states. The first state is characterized by a monolayer of strongly bound proteins and is associated to an equilibrium constant K_S. Further protein binding and the formation of a second, or multiple, layer(s) is characterized by a weaker adsorption, associated to an equilibrium constant K_L[26,27]. Based on previous studies on the characterization of protein adsorption on silica nanoparticles[27,28], the GAB isotherm was applied in this work to describe the experimentally observed data. The model was expressed in terms of $-\Delta I/I_0$, that was assumed to be directly proportional to the adsorbed [NF-L], as follows:

$$\frac{\Delta I}{I_0} = \left(\frac{\Delta I}{I_0}\right)_{max} \frac{K_S C}{(1-K_L C)(1+K_S C-K_L C)} \qquad \textit{(Eq. 6.2)}$$

where $(\Delta I/I_0)_{max}$ is the maximum attainable normalized change in the drain current reached upon the formation of the first monolayer of strongly bound proteins (therefore directly proportional to the maximum surface concentration of NF-L), and C is the bulk protein concentration. When K_L = 0, and therefore no multilayer formation, the equation is reduced to the Langmuir model. While when multilayers are formed, K_L will take values > 0, and

consequently $-\Delta I/I_0$ will take higher values than $(\Delta I/I_0)_{max}$. In Figure 6.3 (panel B), the experimental data fitted to the GAB model is represented as the dashed line, with the best-fit parameters taking the following values: K_S = (3.5 ± 1.6)×10^{12}, K_L = (3.8 ± 0.5)×10^7 and $(\Delta I/I_0)_{max}$= 0.39 ± 0.02.

The fitting to the GAB isotherm accentuated the presence of three regions, corresponding to low, intermediate, and high concentration of NF-L. Taking into consideration the characteristics of the model, this observation was described by the simultaneous presence of two different adsorption processes that partly overlap. The first process is characterized by a progressive increase in the surface concentration of NF-L protein bound to the immobilized antibody on the surface, observed at low concentration of the protein, followed by a pseudo-saturation. At this point, the second adsorption process begins on low-affinity sites, attributed to the formation of multilayers by the binding of NF-L molecules present in solution to the already bound protein-antibody complexes. Following this second adsorption process, a third region can be recognized, characterized by a rapid increase in the amount of adsorbed protein, observed when the high-affinity sites are saturated, and the adsorption occurs only on the low-affinity sites. Processes of this type, characterized by the formation of a second adsorption layer by the binding of proteins to the adsorbed molecules of the first layer, have been previously described by a GAB isotherm in literature[27–29]. The results were interpreted as the formation of protein-protein aggregates based on the tendency of neurofilament proteins to assembly, forming filamentous networks[30–32].

Furthermore, using the GAB isotherm, the limit of detection of the biosensor was estimated to be as low as 30 fM. Furthermore, using the GAB isotherm, the limit of detection of the biosensor was estimated to be as low as 30 fM. The LOD was calculated as $LOD = (\Delta I/I_0)_{blank} + 3\sigma$, where $(\Delta I/I_0)_{blank}$ is the mean value of the biosensor response in the absence of the target analyte, i.e., [NF-L] = 0 M, and σ is the associated standard deviation. σ was obtained from the I_{DS} values during the stabilization time.

As it can be presumed from Figure 6.3 (panel A), the binding of NF-L did not only cause a decrease in the drain current, but was also accompanied by a concomitant decrease in transconductance and a shift of the threshold voltage towards more negative values. The normalized changes in both, g_m and V_{th}, as a function of [NF-L] were quantitatively confirmed, and the corresponding plots are depicted in Figure 6.4.

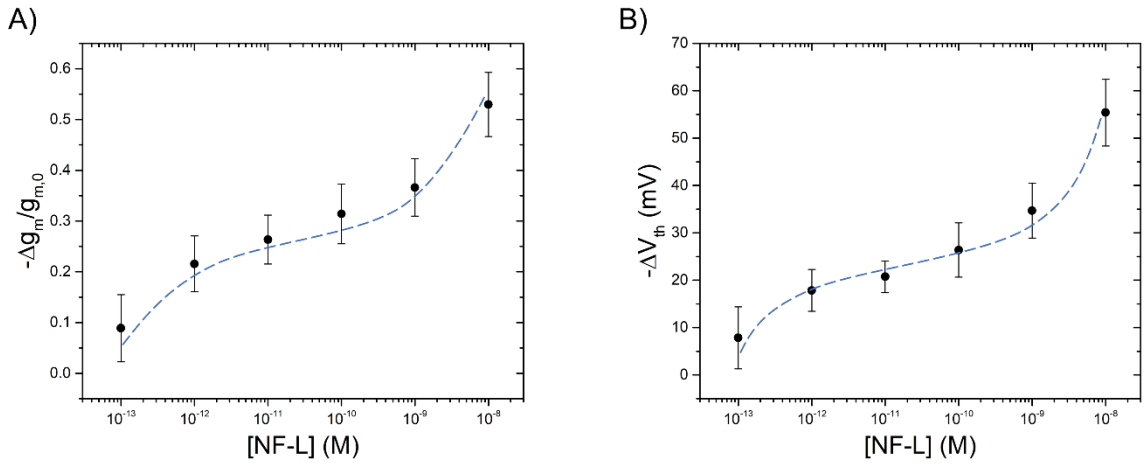

Figure 6.4. Normalized variation in g_m, calculated at V_{GS} = -0.4 V (A) and V_{th} (B) of the EGOFET biosensor as a function of [NF-L]. Data are shown as the mean ± SE of 11 independent experiments; the highest concentration (10 nM) was tested in 8 replicates, while the lowest (100 fM), in 3. The dashed line is a guide to the eye.

A monotonic decrease in both parameters, g_m and V_{th}, was observed following the binding events occurring at the gate surface. It is apparent that both observables showed a similar trend as the observed in the drain current variation, with a big change observed in the low concentrations, followed by a pseudo-plateau in the mid concentration range, and then again, a steep increase at the highest concentrations tested.

The simultaneous variation in g_m and V_{th} resulting from the NF-L binding suggests that the biorecognition process modifies both, the gating capacitance and the gate electrochemical potential. The shift in V_{th} to more negative values was interpreted as the result of the increase of the electrochemical potential at the gate electrode resulting from the binding of NF-L proteins, negatively charged at the operational pH. An increase in the electrochemical potential would derive in a decrease in the work function, with the subsequent decrease in the voltage drop across electrolyte/OSC interface, resulting in a shift if the V_{th} towards more negative potentials and a concomitant decrease in the drain current.

6.4. Morphological characterization

In order to investigate whether the hypothesis of protein aggregate formation at high NF-L concentrations was correct, morphological studies were carried out on the gate surface. Atomic force microscopy and scanning electron microscopy were performed on Au electrodes were

functionalized as previously described and were incubated with solutions containing increasing concentrations of NF-L protein. Figure 6.5 displays the AFM images of Au electrodes recorded at [NF-L] = 0 M, 1 pM, 100 pM, and 1 nM.

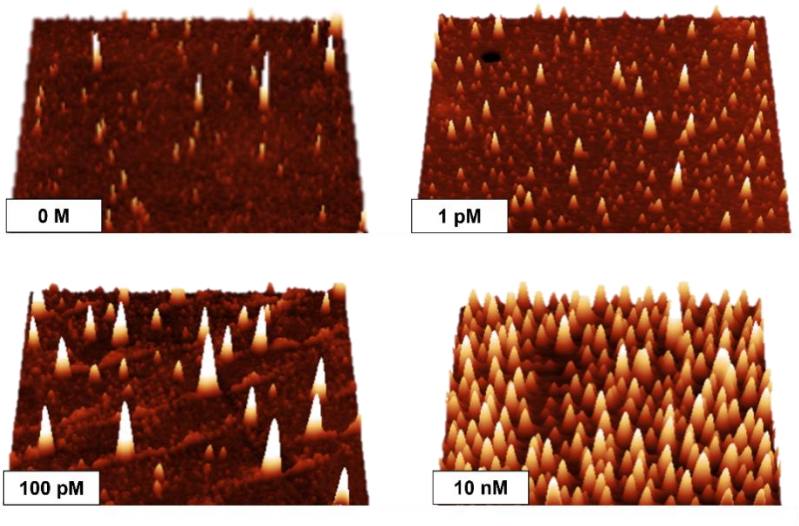

Figure 6.5. 3D AFM topographical images of cys-protein G/anti-NF-L/OEG-modified Au electrodes, upon incubation with increasing concentrations of NF-L.

As reported in Figure 6.5, the morphology of the Au electrodes was heavily dependent on NF-L concentration. Furthermore, at the highest protein concentration tested (10 nM), the formation of particular morphological features, interpreted ad protein aggregates, was observed. This interpretation was further confirmed by performing SEM on the same electrodes, where an increased density of rounded features, ascribed to NF-L aggregates was observed after incubating the electrodes with 10 nM NF-L (Figure 6.6).

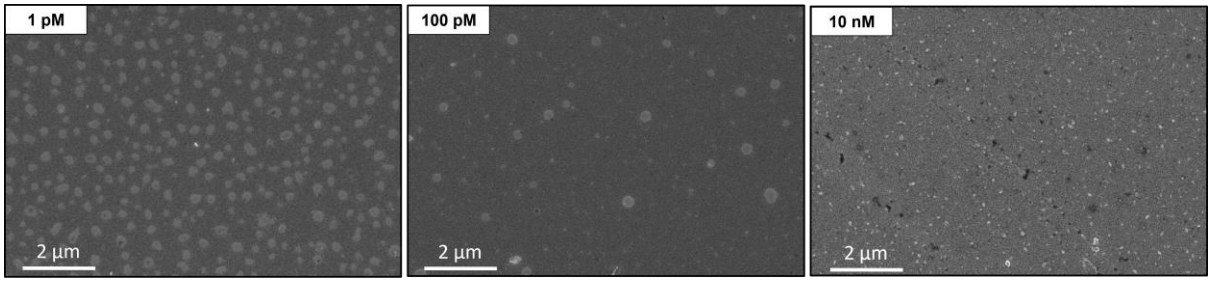

Figure 6.6. SEM images of NF-L proteins immobilized on the Au substrate.

The quantitative analysis of the morphological surface changes with [NF-L], in terms of average surface roughness (σ_{rms}) and lateral correlation length (ξ) is reported in Table 6.2. Due to the increasing protein density bound at the Au electrodes an increase in the surface roughness

was observed. Conversely, an opposite trend was observed in the correlation length: ξ decreases with increasing [NF-L], as the distance between the protein aggregates decreases. Both trends corroborate the interpretation of NF-L aggregation at high protein concentration.

Table 6.2. Morphological analysis at different [NF-L] extracted from AFM images. Results are expressed as mean ± SD of 3 different images of the same electrode.

[NF-L]	σ_{rms} (nm)	ξ (nm)
1 pM	2.9 ± 0.4	209 ± 15
100 pM	5.9 ± 1.6	132 ± 11
10 nM	6.2 ± 0.7	92 ± 8

6.5. Evaluation of the selectivity of the NF-L biosensor

In order to assess the selectivity of the EGOFET-based device, a set of control experiments was performed. In a first set of control experiments, the response of the biosensor was monitored against proteins different to NF-L, which might bind non-specifically at one of the relevant device interfaces yielding an undesired non-specific response. To this purpose, the EGOFETs were exposed to solutions containing a high concentration (1 and 10 nM) of two inflammatory markers, IL-6 or IL-1β, commonly found in the same biological fluids where NF-L can be present. As reported in Figure 6.7 (panel A, blue and green bars), both cytokines caused a non-specific response, however, it is apparent that this non-specific response is significantly lower than the specific one, even when compared to a lower concentration of NF-L. In addition, it is important to highlight that the concentrations of the cytokines tested (1 and 10 nM) are well above the levels than can be found in physiological (about 0.05 pM) as well as pathological (about 0.05 nM) situations[33–35].

In a second round of control experiments, the response of the device was monitored while using a non-selective recognition unit by immobilizing anti-IL-6 antibodies (instead of anti-NF-L ones) on the Au gate surface. In this situation, since no specific recognition unit is present, ideally no specific response is expected following the exposition of the device to solutions containing NF-L. The response of EGOFETs gated by cys-protein G/anti-IL-6/OEG-modified

Au electrodes to NF-L is reported in Figure 6.7 (panel B, purple bars). Noticeably, the non-specific response to NF-L is markedly lower than the specific one. It is apparent that the higher concentration tested, [NF-L] = 10 nM, generated the higher non-specific response, although even in this case, this response was much lower in magnitude than the specific response, even when compared to a lower NF-L concentration, i.e., [NF-L] = 1 nM. In addition, the response observed, for some concentrations, followed the opposite trend with respect to the specific response.

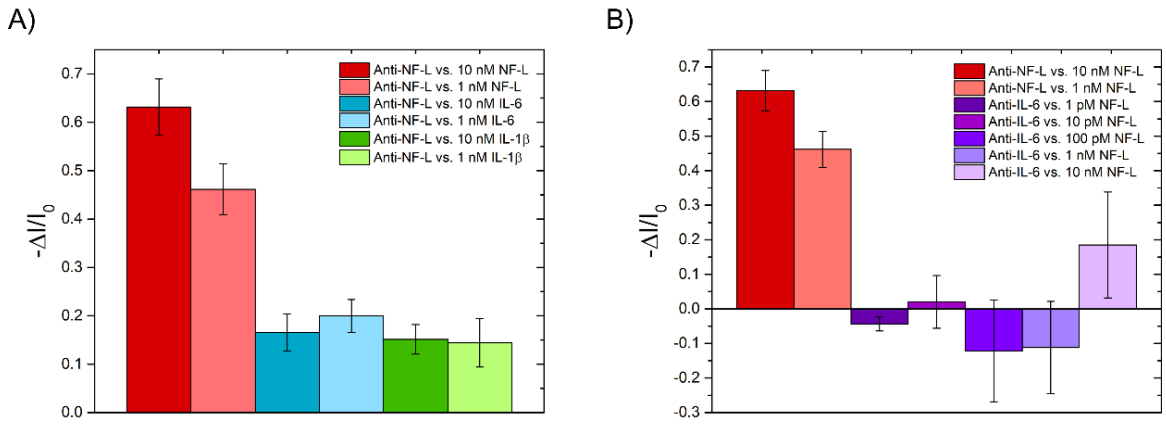

Figure 6.7. Evaluation of the selectivity of the NF-L biosensor. A) Response of the EGOFET-based biosensor upon exposure to different proteins: NF-L (red), IL-6 (blue), and IL-1β (green). B) Comparison of the biosensor response to NF-L when using a specific (red) or a non-specific recognition unit (purple). Data are shown as mean ± SE of 11 (red) or 3 (blue, green, and purple) independent experiments.

In the final round of control experiments, the effect of the presence of other biomolecules was investigated with the aim to assess whether the selectivity of the biosensor would be influenced by the presence of potentially interfering molecules. To this aim, the response of the device was screened against solutions containing increasing concentrations of NF-L in the presence of IL-1β at a constant, high concentration (1 nM). The results are shown in Figure 6.8, with data points represented as blue squares, overlaid to the corresponding dose curve but in the absence of IL-1β (black circles). The response observed to the target analyte is slightly higher in the presence of IL-1β than in its absence, however, taking into account the associated errors, this variations in the current are indistinguishable, indicating that the ability of the biosensor to selectively discriminate NF-L was retained.

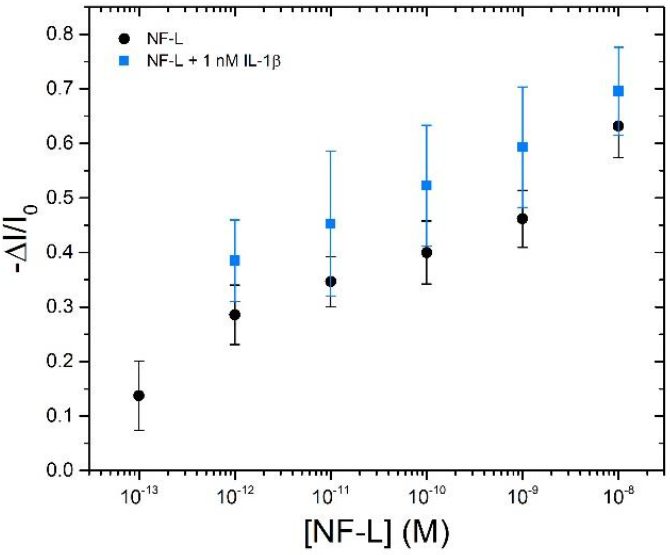

Figure 6.8. Biosensor dose curve $\Delta I/I_0$ versus [NF-L], in the absence (black circles) and the presence (blue squares) of 1 nM IL-1β, calculated at V_{GS} = -0.4 V. Data is shown as mean ± SE of 11 (black circles) and 4 (blue squares) independent experiments.

6.6. Conclusions

The successful detection of NF-L, a biomarker of multiple sclerosis, down to sub-pM concentrations was demonstrated using an EGOFET-based biosensor. The biosensor was able to detect NF-L within a dynamic concentration range, spanning five orders of magnitude, from 100 fM to 10 nM, with an estimated LOD as low as 30 fM. The experimental data was fitted to the GAB adsorption model, which provided an insight of the binding phenomena occurring at the gate surface. In addition, a large set of control experiments was performed in order to evaluate the selective response of the biosensor. The results of these experiments provided evidence that supported that the response observed could be safely ascribed to the specific interaction of NF-L proteins and their corresponding antibody immobilized on the Au surface. In addition, the EGOFET biosensor showed good stability and reproducibility, and provided a fast response. Therefore, although further optimization of the biosensor is required, these results place the biosensor as a promising platform for multiple sclerosis management.

6.7. References

1. Lambertsen, K. L., Soares, C. B., Gaist, D. & Nielsen, H. H. Neurofilaments: The C-Reactive Protein of Neurology. *Brain Sci* **10**, 56 (2020).
2. Khalil, M. *et al.* Neurofilaments as biomarkers in neurological disorders. *Nat Rev Neurol* **14**, 577–589 (2018).
3. Disanto, G. *et al.* Serum Neurofilament light: A biomarker of neuronal damage in multiple sclerosis. *Ann Neurol* **81**, 857–870 (2017).
4. Barro, C. *et al.* Serum neurofilament as a predictor of disease worsening and brain and spinal cord atrophy in multiple sclerosis. *Brain* **141**, 2382–2391 (2018).
5. Kuhle, J. *et al.* Blood neurofilament light chain as a biomarker of MS disease activity and treatment response. *Neurology* **92**, e1007–e1015 (2019).
6. Ferraro, D. *et al.* Plasma neurofilaments correlate with disability in progressive multiple sclerosis patients. *Acta Neurol Scand* **141**, 16–21 (2020).
7. Håkansson, I. *et al.* Neurofilament light chain in cerebrospinal fluid and prediction of disease activity in clinically isolated syndrome and relapsing-remitting multiple sclerosis. *Eur J Neurol* **24**, 703–712 (2017).
8. Koklu, A. *et al.* Microfluidic Integrated Organic Electrochemical Transistor with a Nanoporous Membrane for Amyloid-β Detection. *ACS Nano* **15**, 8130–8141 (2021).
9. Berto, M. *et al.* EGOFET Peptide Aptasensor for Label-Free Detection of Inflammatory Cytokines in Complex Fluids. *Adv Biosyst* **2**, 1700072 (2018).
10. Kim, D.-J. *et al.* Organic electrochemical transistor based immunosensor for prostate specific antigen (PSA) detection using gold nanoparticles for signal amplification. *Biosens Bioelectron* **25**, 2477–2482 (2010).
11. Sailapu, S. K. *et al.* Standalone operation of an EGOFET for ultra-sensitive detection of HIV. *Biosens Bioelectron* **156**, 112103 (2020).
12. Bae, Y. M., Oh, B.-K., Lee, W., Lee, W. H. & Choi, J.-W. Study on orientation of immunoglobulin G on protein G layer. *Biosens Bioelectron* **21**, 103–110 (2005).
13. Lee, J. H., Choi, H. K., Lee, S. Y., Lim, M.-W. & Chang, J. H. Enhancing immunoassay detection of antigens with multimeric protein Gs. *Biosens Bioelectron* **28**, 146–151 (2011).
14. Moon, J. *et al.* Surface-Independent and Oriented Immobilization of Antibody via One-Step Polydopamine/Protein G Coating: Application to Influenza Virus Immunoassay. *Macromol Biosci* **19**, 1800486 (2019).

15. Centi, S., Ratto, F., Tatini, F., Lai, S. & Pini, R. Ready-to-use protein G-conjugated gold nanorods for biosensing and biomedical applications. *J Nanobiotechnology* **16**, 5 (2018).

16. Casalini, S. *et al.* Multiscale Sensing of Antibody–Antigen Interactions by Organic Transistors and Single-Molecule Force Spectroscopy. *ACS Nano* **9**, 5051–5062 (2015).

17. Berto, M. *et al.* Label free detection of plant viruses with organic transistor biosensors. *Sens Actuators B Chem* **281**, 150–156 (2019).

18. Sensi, M. *et al.* Anti-drug antibody detection with label-free electrolyte-gated organic field-effect transistors. *Chemical Communications* **57**, 367–370 (2021).

19. Jiang, C. *et al.* Antifouling Strategies for Selective *In Vitro* and *In Vivo* Sensing. *Chem Rev* **120**, 3852–3889 (2020).

20. Chen, S., Li, L., Zhao, C. & Zheng, J. Surface hydration: Principles and applications toward low-fouling/nonfouling biomaterials. *Polymer (Guildf)* **51**, 5283–5293 (2010).

21. Galliani, M. *et al.* Flexible Printed Organic Electrochemical Transistors for the Detection of Uric Acid in Artificial Wound Exudate. *Adv Mater Interfaces* **7**, 2001218 (2020).

22. Manco Urbina, P. A. *et al.* Physical insights from the Frumkin isotherm applied to electrolyte gated organic transistors as protein biosensors. *J Mater Chem C Mater* **9**, 10965–10974 (2021).

23. Macchia, E. *et al.* Organic Field-Effect Transistor Platform for Label-Free, Single-Molecule Detection of Genomic Biomarkers. *ACS Sens* **5**, 1822–1830 (2020).

24. Ishikawa, F. N. *et al.* A Calibration Method for Nanowire Biosensors to Suppress Device-to-Device Variation. *ACS Nano* **3**, 3969–3976 (2009).

25. Berto, M. *et al.* Green Fabrication of (6,5)Carbon Nanotube/Protein Transistor Endowed with Specific Recognition. *Adv Electron Mater* **7**, 2001114 (2021).

26. Ebadi, A., Soltan Mohammadzadeh, J. S. & Khudiev, A. What is the correct form of BET isotherm for modeling liquid phase adsorption? *Adsorption* **15**, 65–73 (2009).

27. Meissner, J., Prause, A., Bharti, B. & Findenegg, G. H. Characterization of protein adsorption onto silica nanoparticles: influence of pH and ionic strength. *Colloid Polym Sci* **293**, 3381–3391 (2015).

28. Lee, J. G., Lannigan, K., Shelton, W. A., Meissner, J. & Bharti, B. Adsorption of Myoglobin and Corona Formation on Silica Nanoparticles. *Langmuir* **36**, 14157–14165 (2020).

29. Bharti, B., Meissner, J. & Findenegg, G. H. Aggregation of Silica Nanoparticles Directed by Adsorption of Lysozyme. *Langmuir* **27**, 9823–9833 (2011).

30. Angelides, K. J., Smith, K. E. & Takeda, M. Assembly and exchange of intermediate filament proteins of neurons: neurofilaments are dynamic structures. *Journal of Cell Biology* **108**, 1495–1506 (1989).

31. Lee, M., Xu, Z., Wong, P. & Cleveland, D. Neurofilaments are obligate heteropolymers in vivo. *Journal of Cell Biology* **122**, 1337–1350 (1993).

32. Heins, S. *et al.* The rod domain of NF-L determines neurofilament architecture, whereas the end domains specify filament assembly and network formation. *Journal of Cell Biology* **123**, 1517–1533 (1993).

33. Chen, L. Y. C., Hoiland, R. L., Stukas, S., Wellington, C. L. & Sekhon, M. S. Confronting the controversy: interleukin-6 and the COVID-19 cytokine storm syndrome. *European Respiratory Journal* **56**, 2003006 (2020).

34. Gibellini, L. *et al.* Plasma Cytokine Atlas Reveals the Importance of TH2 Polarization and Interferons in Predicting COVID-19 Severity and Survival. *Front Immunol* **13**, (2022).

35. del Valle, D. M. *et al.* An inflammatory cytokine signature predicts COVID-19 severity and survival. *Nat Med* **26**, 1636–1643 (2020).

Chapter 7.
Monitoring mtDNA hybridization with an EGOT-based biosensor

This chapter covers the fabrication of a DPP-DTT-based biosensor for a second potential biomarker for multiple sclerosis, mtDNA. In the proposed architecture, a single stranded mtDNA sequence is immobilized at the Au gate surface, acting as a capturing probe, and the hybridization with the complementary sequence is monitored. After successfully validating and optimizing the Au functionalization protocol using surface plasmon-enhanced fluorescent spectroscopy, the biosensing capability of the EGOT was assessed. The obtained results are discussed.

7.1. Introduction

Mitochondrial dysfunction has been largely studied in the pathology of MS, and it is believed to have an important role in the demyelination process[1,2]. Furthermore, increased levels of circulating mtDNA have been reported in recent studies in MS patients[3,4]. Aiming towards the development of a biosensor for an accurate MS biomarker, this chapter was focused on the investigation of mtDNA as a promising MS biomarker. The proposed architecture was based on an OECT architecture, using the polymer DPP-DTT as OSC. The Au gate electrode was used as the sensing part of the sensor, and the functionalization strategy consisted of the immobilization of a mtDNA sequence on the Au surface via biotin-neutravidin interaction. The capturing mtDNA probe consisted of a single stranded sequence composed by 20 base pairs (bp), with an additional 6 adenine bp, serving as spacer, and a biotin molecule at the 5' end. The biotin-streptavidin coupling has been widely used for the immobilization of molecules of interest, including antibodies[5–7], aptamers[8–10], and nucleic acids[11–13].

Recently, biosensors based on organic electronic transistors have been developed for the detection of nucleic acids. In the reported architectures, the detection was achieved was immobilizing a single stranded capture probe on the gate surface, exploiting different functionalization strategies. Among some of the reported strategies, the capture probe was modified with a thiol residue, mediating its covalent binding on the Au gate surface[14,15]. In a similar approach, the Au gate surface was modified with a SAM, prior to the thiolated probe immobilization[16]. In another work, a polydopamine film was deposited on a carbon gate, and was further functionalized with a DNA probe via Michael's addition or Schiff base chemistry[17]. Furthermore, in a recent work, the development of an ultra-sensitive SiMoT-biosensor, functionalized with a biotinylated DNA probe, was reported[18].

In this chapter, the development of an EGOT-based biosensor for mtDNA, a candidate biomarker of MS, is described. The Au gate functionalization exploits the biotin-streptavidin coupling to immobilize a single-stranded mtDNA probe. Upon the incubation with the complementary sequence, both DNA strands hybridize, resulting in a measurable electrical signal. The employed capturing DNA is a 20-base long oligonucleotide (with a 6-base spacer), with a specific sequence for mtDNA, which ensures the hybridization of mitochondrial, and not nuclear DNA. Prior to employ the developed EGOT biosensor to monitor mtDNA hybridization, the Au functionalization process was monitored in real time using SPFS.

7.2. Gate functionalization and characterization

The Au gate was functionalized with a specific single-stranded mtDNA oligonucleotide sequence, acting as a capturing probe for the complementary sequence. A biotinylated label was attached to the probe sequence, which was used to immobilize it on the gate surface. Previously, the Au gate electrodes were immersed in a mixed biotin-OEG solution, promoting the formation of a SAM on the Au surface. Then, the electrodes were incubated in a solution of neutravidin, allowing its conjugation with the biotin moieties present in the SAM, and driving the further immobilization of the capturing probe.

The combined SPR-SPFS setup allowed the evaluation of the Au functionalization. The immobilization of the capturing mtDNA probe (P-DNA) was evaluated using SPR, while SPFS was employed to monitor the mtDNA hybridization which, due to the small size of the DNA, results in a subtle change in the refractive index that SPR is unable to measure. The hybridization of the mtDNA strands was evaluated in a sandwich assay, where, after the immobilization of the P-DNA on the Au surface, the complementary strand (C-DNA) was injected. C-DNA was composed by a larger number of nucleotides than P-DNA, which allowed its further hybridization with a fluorescently labelled DNA sequence (L-DNA). The employed label was AlexaFluor647. A typical example of the SPR and fluorescence response is illustrated in Figure 7.1.

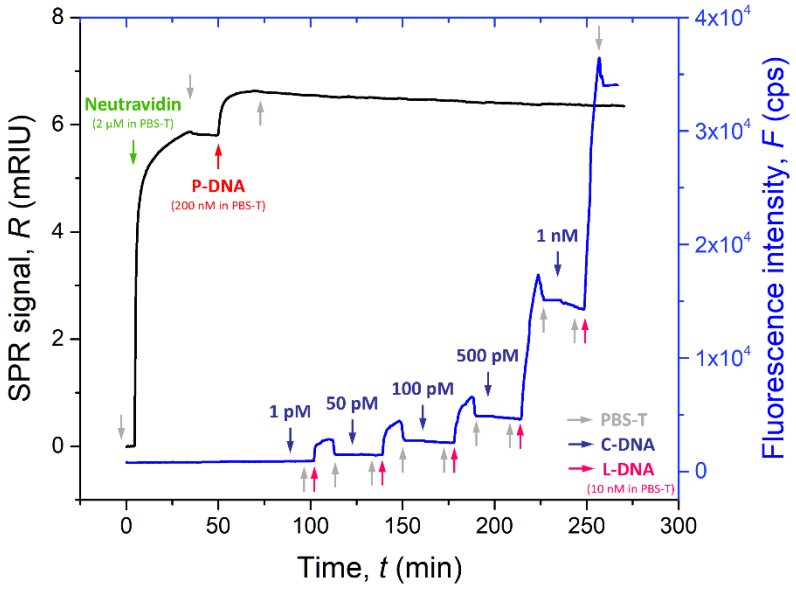

Figure 7.1. Combined SPR-SPFS characterization. Black curve represents the kinetic of the SPR signal upon neutravidin conjugation and P-DNA probe immobilization. In blue, the fluorescence signal is an example of the kinetics upon C-DNA hybridization.

Notably, the specific binding of neutravidin to the biotin moieties exposed on the SAM surface resulted in an increase in the SPR response of ΔR_{NA} = 6 ± 1 mRIU. This step of neutravidin immobilization serves to anchor the capturing ss-mtDNA probe (P-DNA) to the sensing surface, which led to an increase in the SPR response of $\Delta R_{P\text{-}DNA}$ = 0.64 ± 0.11 mRIU. Because of its reduced size, the further hybridization of the immobilized probe with its complementary ss-mtDNA strand (C-DNA) could not be monitored by SPR. Therefore, SPFS was employed for this purpose. As reported in Figure 7.1, a rapid increase in the fluorescence signal is observed following the injection of the fluorescently labelled probe (L-DNA), corresponding to its hybridization with the C-DNA/P-DNA complex immobilized on the Au surface. The selectivity of the L-DNA sequence for C-DNA was evaluated by recording the fluorescent signal after the injection of L-DNA, in the absence of C-DNA. The obtained fluorescence intensity, $\Delta F_{P\text{-}DNA/L\text{-}DNA}$ = 142 ± 68 cps, was significantly smaller in comparison to the smallest concentration of C-DNA tested (ΔF_{1pM} = 731 ± 177 cps), indicating that the fluorescent signal obtained following the injection of increasing concentrations of C-DNA can be safely ascribed to the hybridization of C-DNA with the complementary P-DNA attached on the Au surface.

Additionally, after every reaction step, the reflectivity curves were recorded (Figure 7.2, panel A). From these curves, the functionalization process was evaluated in terms of surface mass density (Γ), and the fluorescence signal resulted following the incubation with increasing concentrations of C-DNA was quantitatively assessed (Figure 7.2, panel B).

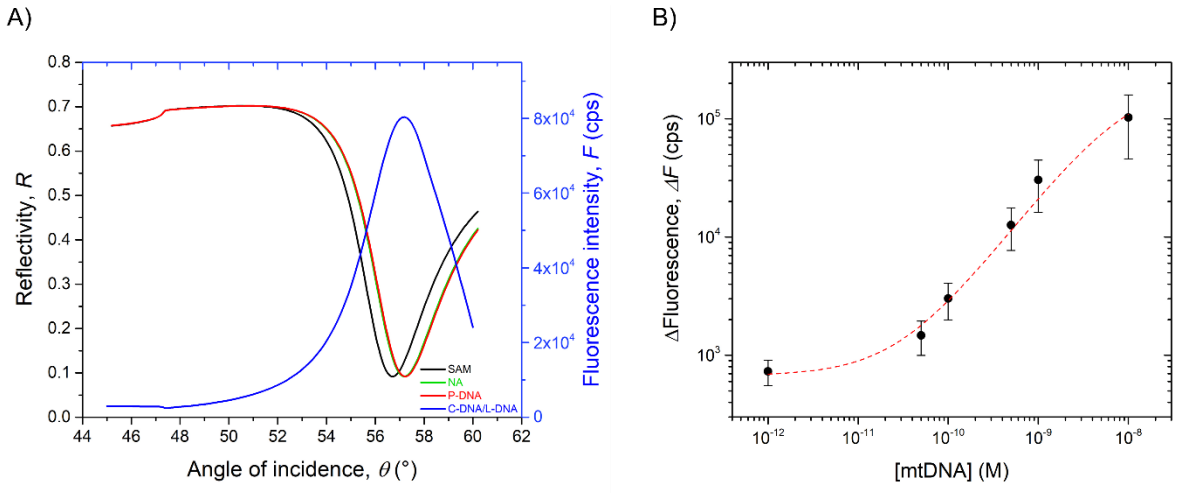

Figure 7.2. A) Respective angular reflectivity, *R*, and fluorescence, *F*, scans measured between the assay steps. The fluorescence curve was recorded following the hybridization of 1 nM C-DNA. B) Normalized fluorescence signal recorded after the hybridization of P-DNA with increasing concentrations of C-DNA, fitted to the Langmuir model (red line). The results are expressed as the mean ± SE of 3 independent experiments.

In order to determine the thickness of the biolayers, the obtained reflectivity curves were fitted to a Fresnel reflectivity-based model, using the Winspall 3.02 software. This fitting allowed the determination of the thickness and the apparent refractive index values for the employed SPR glass slide, which were further employed as reference for the simulation of thickness changes induced by the biolayer formation. The surface mass density, Γ, was determined by applying Feijter's equation[19]:

$$\Gamma = d_p(n_p - n_b)/(dn/dc) \qquad \textit{(Eq. 7.1)}$$

Where d_p is the thickness of the biolayer, n_p is the refractive index of the biolayer, n_b is the refractive index of the aqueous solution in contact with the biolayer, and *dc/dn* is the refractive index increment of the adsorbed biolayer[20]. The determination of Γ for each biolayer allowed to estimate the grafting density, σ, of immobilized protein and mtDNA molecules:

$$\sigma = \Gamma/MW \qquad \textit{(Eq. 7.2)}$$

The obtained data is reported in Table 7.2. The values for *dc/dn* were taken from literature[21].

Table 7.1. Determination of the thickness, d_p, surface mass density, Γ, and grafting density, σ, for the neutravidin and P-DNA biolayers. The aqueous solution in contact with the biolayer was PBS-T buffer (n_b = 1.333).

Layer	$\boldsymbol{d_p}$ (nm)	$\boldsymbol{n_p}$	***dc/dn*** (mm^3/mg)	$\boldsymbol{\Gamma}$ (ng/mm^2)	***MW*** (kDa)	$\boldsymbol{\sigma}$ ($nmol/mm^2$)
Neutravidin	3.6	1.45	0.18	2.4	67	3.6×10^{-5}
P-DNA	0.3	1.45	0.19	0.2	8	2.4×10^{-5}

The calculated thickness, surface mass density and grafting density for neutravidin are well in line with previously reported findings[22–24]. From the calculated grafting density, a binding ratio of ~1.5 between neutravidin and the biotinylated mtDNA probe is obtained, which is in excellent agreement with previous reports[21,25]. However, assuming that after the neutravidin binding to the biotin moieties of the SAM surface two biotin-binding sites remain accessible, a hypothetical ratio of 2 would be expected. Nonetheless, the distance between the two biotin-binding sites is close to the hydrodynamic diameter of DNA, which results in electrostatic

repulsion and, together with steric hindrance, prevents the efficient binding of two biotinylated DNA strands per one single molecules of neutravidin[26,27].

The evaluation of the fluorescence signal resulted from the formation of the P-DNA/C-DNA complex, and its further hybridization with the L-DNA sequence is reported in Figure 7.2 (panel B). The data is presented normalized to the baseline fluorescence ($\Delta F = F - F_{baseline}$). As observed, the recorded fluorescence signal presented a clear dependency on the concentration of the target analyte. The trend showed a small increase in the signal for the lower concentrations tested (low pM range), followed by a steep increase in the mid concentration range, resembling almost a linear dependency. Finally, for the highest concentration tested ([mtDNA] = 10 nM), the same behaviour was observed, but showing a less steep increase in ΔF, which might suggest the approximation to saturation. However, higher concentrations should be tested to confirm this suggestion. Based on the observed trend, the data was fitted to the Langmuir model:

$$\Delta S = \frac{\Delta S_{max} K_a C}{1 + K_a C} \Delta S_0 \qquad \textit{(Eq. 7.3)}$$

where ΔS is the normalized signal obtained, ΔS_{max} is the maximum normalized signal reachable, K_a is the equilibrium association constant, and C is the mtDNA concentration. An additional parameter ΔS_0, defining the observed initial ΔS, has been included in order to offset the fitting curve. The data fitting to the proposed model, illustrated in Figure 7.2 (panel B), allowed the determination of the equilibrium association constant, which value was estimated to be $K_a = (1.1 \pm 0.7) \times 10^8$ M^{-1}. This value is in agreement with previously reported findings using a similar setup[24,28].

Please note that, during the SPFS experiments, all solutions were prepared in a buffer solution containing PBS + 0.05% Tween 20, while during the electrical experiments, in order to avoid the contact of the detergent agent with the organic semiconductor, the measurements were performed using only PBS. Nonetheless, prior to the electrical measurements, a final functionalization step, consisting of incubation in PBS + 0.05% Tween 20 (for 15 minutes), was included with the aim of reducing non-specific binding.

7.3. Dose curve analysis with EGOT devices

After successfully assessing the Au gate functionalization strategy and proving the hybridization process by SPFS, the biosensing experiments were repeated in an electrical setup. To this aim, transfer curves were recorded in a PBS solution containing increasing concentrations of mtDNA. For the electrical measurements, the same concentration range as for the optical measurements was evaluated, i.e., from 1 pM to 10 nM, but several intermediate concentrations were added. The typical response of the biosensor upon exposure to solutions containing the complementary ss-mtDNA sequence, illustrated in Figure 7.3 (panel B), was characterized by an increase in the drain current, concomitant to an increase of the transconductance.

The increase in the drain current upon DNA hybridization is not surprising, and it has been previously observed in similar studies[17]. This increase in the drain current resulting from DNA hybridization has been ascribed to the negative charge of the DNA, attributed mostly to the phosphate groups of the nucleotides. The negative charge of the ss-DNA would contribute to a significant voltage drop at the gate-electrolyte interface[17].

As it can be observed in the transfer graph (Figure 7.3, panel A), the increase in I_{DS} exhibits a monotonic trend that seems to saturate for the highest concentrations tested (i.e., in the nM concentration range). Moreover, as it can be presumed from the transfer curve, the DNA hybridization had a significant impact on g_m. In fact, after assessing quantitatively the observed changes, in terms of ΔI_{DS}, Δg_m, ΔV_{th}, transconductance proved to be the more accurate parameter for monitoring DNA hybridization. The normalized change in g_m, calculated as $\Delta g_m/\Delta g_{m,0}$, is reported in Figure 7.3 (panel B).

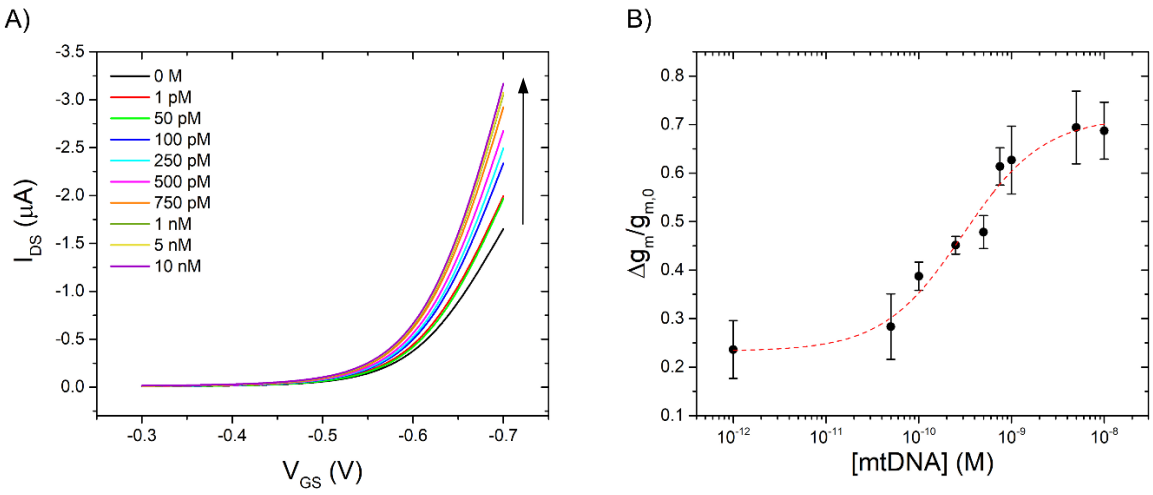

Figure 7.3. Representative response of the biosensor upon exposure to increasing concentrations of mtDNA: A) monotonical increase of the drain current, and B) concomitant increase of transconductance. Δg_m was calculated at V_{GS} = -0.6 V. Data is shown as the mean ± SE of 3 independent experiments, except for [mtDNA] = 5 nM, for which the result illustrated corresponds to the mean ± SD of 2 experiments. The red line is the fit to the Langmuir model (Eq. 7.3).

It is apparent that the major variation in g_m, i.e., the maximum sensitivity, is observed in the intermediate pM range, while in the low pM range a minor change is perceived. Moreover, in the highest pM and nM range, the variation in g_m is rather minor, suggesting the saturation of the system. This trend is in line with the observations of I_{DS}, and, furthermore, it resembles the trend observed during the optical SPFS measurements. Therefore, the obtained data was fitted to the Langmuir isotherm (Eq. 7.3). The determined K_a value from the Langmuir fitting was $K_a = (3.3 \pm 0.8) \times 10^9\ M^{-1}$.

The difference observed in the estimated K_a values for the optical and the electrical measurements might be considered non-significant, as the variation is in the range of 1 magnitude, which is in the variation range observed upon the comparison of different studies[29,30]. The observed K_a values indicate that both assays, optical and electrical, operate successfully as biosensors in the same concentration range ([mtDNA] ~100 pM – 1 nM).

7.4. Evaluation of the biosensor selectivity

Once the successful operation of the biosensor was assessed, a series of control experiments were performed with the aim of confirming whether the observed response could be safely ascribed to the interaction of the mtDNA sequence (C-DNA) present in solution and the

corresponding complementary probe (P-DNA), immobilized on the gate surface. Therefore, the response of the biosensor was evaluated in the presence of a non-complementary mt-DNA sequence (NC-DNA), which could potentially interact with the immobilized mtDNA probe on the gate surface. The NC-DNA sequence was tested at the highest concentration used in the experiments. As witnessed in Figure 7.4, even such high concentration did not cause a significant response. In fact, an opposite trend in the response was observed, which, when compared to the smallest concentration of C-DNA tested (1 pM), might be considered negligible.

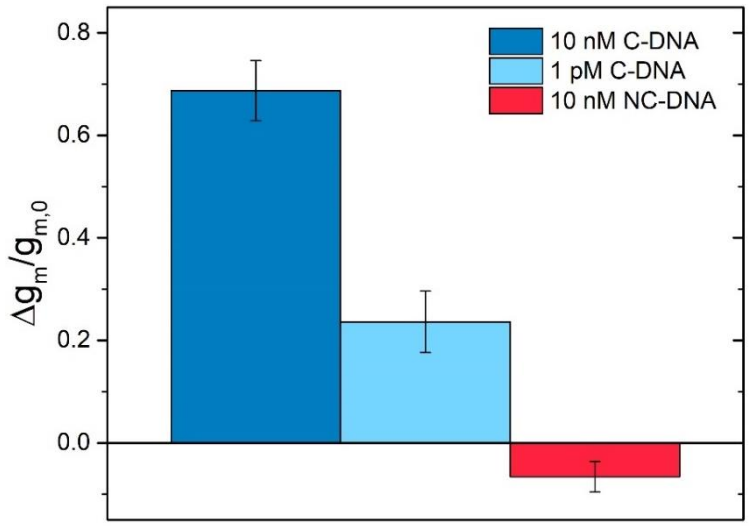

Figure 7.4. Evaluation of the biosensor selectivity in the presence of a non-complementary mtDNA probe (red), compared to the specific response (blue). Data is presented as the mean ± SE of 3 independent experiments.

7.5. Conclusions

In conclusion, the work presented in this chapter has demonstrated the successful application of an EGOT-based biosensor for the monitoring of mtDNA hybridization. The functionalization strategy was evaluated using a combined optical SPR-SPFS setup, yielding satisfactory results. In addition, the SPFS setup allowed the monitoring in real time of the mtDNA hybridization by using an additional, fluorescently labelled mtDNA sequence. Then, the capability of the device to serve as a biosensor for monitoring mtDNA hybridization in an electrical setup was evaluated. The obtained results, together with the negligible non-specific binding resulted from the control experiments, proved the effective operation of the biosensor. Moreover, the obtained data from the optical and electrical measurements was fitted to the

Langmuir isotherm, allowing the evaluation of the binding process. The estimated equilibrium constant was similar in both assays, indicating that both setups can be employed to successfully monitor mtDNA hybridization in the selected concentration range. Although further optimization work is required, the reported data suggest the potential implementation of the developed label-free EGOT-based biosensor as a promising platform for monitoring biomarkers of multiple sclerosis, such as mtDNA, with a performance comparable to an optical assay.

7.6. References

1. Mao, P. & Reddy, P. H. Is multiple sclerosis a mitochondrial disease? *Biochimica et Biophysica Acta (BBA) - Molecular Basis of Disease* **1802**, 66–79 (2010).

2. Barcelos, I. P. de, Troxell, R. M. & Graves, J. S. Mitochondrial Dysfunction and Multiple Sclerosis. *Biology (Basel)* **8**, 37 (2019).

3. Varhaug, K. N. *et al.* Increased levels of cell-free mitochondrial DNA in the cerebrospinal fluid of patients with multiple sclerosis. *Mitochondrion* **34**, 32–35 (2017).

4. Nasi, M. *et al.* Increased plasma levels of mitochondrial DNA and pro-inflammatory cytokines in patients with progressive multiple sclerosis. *J Neuroimmunol* **338**, 577107 (2020).

5. Palazzo, G. *et al.* Detection Beyond Debye's Length with an Electrolyte-Gated Organic Field-Effect Transistor. *Advanced Materials* **27**, 911–916 (2015).

6. Kasry, A., Nicol, A. & Knoll, W. Grating-coupled surface-plasmon fluorescence DNA sensor. *Applied Physics B* **127**, 68 (2021).

7. Seherler, S., Bozdogan, A., Ozal Ildeniz, T. A., Kok, F. N. & Anac Sakir, I. Detection of cholera toxin with surface plasmon field-enhanced fluorescent spectroscopy. *Biotechnol Appl Biochem* **69**, 1557–1566 (2022).

8. Hasler, R. *et al.* Field-Effect Transistor with a Plasmonic Fiber Optic Gate Electrode as a Multivariable Biosensor Device. *ACS Sens* **7**, 504–512 (2022).

9. Kotlarek, D. *et al.* Surface plasmon resonance-based aptasensor for direct monitoring of thrombin in a minimally processed human blood. *Sens Actuators B Chem* **320**, 128380 (2020).

10. Kraemer, M. *et al.* Aptamers as Novel Binding Molecules on an Antimicrobial Peptide-Armored Composite Hydrogel Wound Dressing for Specific Removal and Efficient Eradication of Pseudomonas aeruginosa. *Int J Mol Sci* **24**, 4800 (2023).

11. D'Agata, R., Giuffrida, M. & Spoto, G. Peptide Nucleic Acid-Based Biosensors for Cancer Diagnosis. *Molecules* **22**, 1951 (2017).

12. Zanoli, L. M., D'Agata, R. & Spoto, G. Functionalized gold nanoparticles for ultrasensitive DNA detection. *Anal Bioanal Chem* **402**, 1759–1771 (2012).

13. Aktas, G. B., Ribera, A., Skouridou, V. & Masip, L. DNA immobilization and detection using DNA binding proteins. *Anal Bioanal Chem* **413**, 1929–1939 (2021).

14. Lin, P., Luo, X., Hsing, I.-M. & Yan, F. Organic Electrochemical Transistors Integrated in Flexible Microfluidic Systems and Used for Label-Free DNA Sensing. *Advanced Materials* **23**, 4035–4040 (2011).

15. Chen, C. *et al.* A sensitive platform for DNA detection based on organic electrochemical transistor and nucleic acid self-assembly signal amplification. *RSC Adv* **11**, 37917–37922 (2021).

16. Selvaraj, M. *et al.* Label free detection of miRNA-21 with electrolyte gated organic field effect transistors (EGOFETs). *Biosens Bioelectron* **182**, 113144 (2021).

17. Sensi, M. *et al.* Monitoring DNA Hybridization with Organic Electrochemical Transistors Functionalized with Polydopamine. *Macromol Mater Eng* **307**, 2100880 (2022).

18. Sarcina, L. *et al.* A large-area organic transistor with 3D-printed sensing gate for noninvasive single-molecule detection of pancreatic mucinous cyst markers. *Anal Bioanal Chem* **414**, 5657–5669 (2022).

19. De Feijter, J. A., Benjamins, J. & Veer, F. A. Ellipsometry as a tool to study the adsorption behavior of synthetic and biopolymers at the air-water interface. *Biopolymers* **17**, 1759–1772 (1978).

20. Tumolo, T., Angnes, L. & Baptista, M. S. Determination of the refractive index increment (dn/dc) of molecule and macromolecule solutions by surface plasmon resonance. *Anal Biochem* **333**, 273–279 (2004).

21. Su, X., Wu, Y.-J., Robelek, R. & Knoll, W. Surface Plasmon Resonance Spectroscopy and Quartz Crystal Microbalance Study of Streptavidin Film Structure Effects on Biotinylated DNA Assembly and Target DNA Hybridization. *Langmuir* **21**, 348–353 (2005).

22. Blasi, D. *et al.* Enhancing the Sensitivity of Biotinylated Surfaces by Tailoring the Design of the Mixed Self-Assembled Monolayer Synthesis. *ACS Omega* **5**, 16762–16771 (2020).

23. Lechner, B. *et al. In Situ* Monitoring of Rolling Circle Amplification on a Solid Support by Surface Plasmon Resonance and Optical Waveguide Spectroscopy. *ACS Appl Mater Interfaces* **13**, 32352–32362 (2021).

24. Park, H. *et al.* Kinetic and affinity analyses of hybridization reactions between peptide nucleic acid probes and DNA targets using surface plasmon field-enhanced fluorescence spectroscopy. *Biointerphases* **1**, 113–122 (2006).

25. Su, X., Wu, Y.-J. & Knoll, W. Comparison of surface plasmon resonance spectroscopy and quartz crystal microbalance techniques for studying DNA assembly and hybridization. *Biosens Bioelectron* **21**, 719–726 (2005).

26. Höök, F., Ray, A., Nordén, B. & Kasemo, B. Characterization of PNA and DNA Immobilization and Subsequent Hybridization with DNA Using Acoustic-Shear-Wave Attenuation Measurements. *Langmuir* **17**, 8305–8312 (2001).

27. Larsson, C., Rodahl, M. & Höök, F. Characterization of DNA Immobilization and Subsequent Hybridization on a 2D Arrangement of Streptavidin on a Biotin-Modified Lipid Bilayer Supported on SiO_2. *Anal Chem* **75**, 5080–5087 (2003).

28. Kasry, A., Nicol, A. & Knoll, W. Grating-coupled surface-plasmon fluorescence DNA sensor. *Applied Physics B* **127**, 68 (2021).

29. Su, X., Robelek, R., Wu, Y., Wang, G. & Knoll, W. Detection of Point Mutation and Insertion Mutations in DNA Using a Quartz Crystal Microbalance and MutS, a Mismatch Binding Protein. *Anal Chem* **76**, 489–494 (2004).

30. Chen, Q., Förch, R. & Knoll, W. Characterization of Pulsed Plasma Polymerization Allylamine as an Adhesion Layer for DNA Adsorption/Hybridization. *Chemistry of Materials* **16**, 614–620 (2004).

Chapter 8.

Detection of neurofilament light chain with an EGOT-based biosensor in blood plasma

This chapter describes the development of an electrolyte-gated organic transistor-based immunosensor for the detection of neurofilament light chain, a potential biomarker of multiple sclerosis, in plasma samples. The gate functionalization protocol is thoroughly validated and optimized using optical techniques. The capability of the biosensor to selectively detect the target protein is assessed in a buffer solution and in plasma samples. Finally, the selectivity of the biosensor in plasma is evaluated. The collected results are discussed.

8.1. Introduction

In the last years, there has been an increasing interest in the integration of organic electronics within the clinical field. In particular, major advances have been achieved in the development of organic electronic-based devices for healthcare applications, including cell monitoring[1–4], electrophysiology[5–8], and biosensing[9–11]. Biosensors based on organic electronics have been reported for a broad number of applications, such as gas, pH, metabolite, or biomolecule sensing[12–14]. Currently, the development of ultra-sensitive biosensors, based on organic electronics, is a fast-growing field. The final goal is to provide highly sensitive and specific biosensors, capable of detecting the target analyte in a biological fluid, such as sweat, saliva, urine, or blood, for point-of-care testing. The secreted body fluids, e.g., sweat, urine and saliva, are readily available and, in addition, their relative simplicity, in terms of composition, is considered an advantage for biosensing assays. However, for the same reason, limited information can be obtained from the examination of samples derived from these fluids, as they are composed mainly by salts, with a limited protein content. Therefore, samples from cerebrospinal and intravascular fluids are generally preferred. The analysis of the CSF is of great importance especially in neurodegenerative diseases, such as MS, as it provides a closer look of the ongoing damage. However, as already mentioned in previous chapters, CSF cannot be used in routinary testing. Hence, the current methods are focusing on the analysis of blood-derived samples such as plasma or serum, for MS biomarkers detection.

In this context, highly sensitive methods for the detection of analytes of interest in blood-derived samples have been developed in recent years. For instance, SiMoA technology allows the ultrasensitive biomarker detection in plasma or serum, even below the limit of quantification[15]. This method is the current gold standard for the quantitative determination of the MS biomarker NF-L. Despite its remarkable sensitivity, this assay presents strong limitations to be applied in routinary testing, as it is extremely expensive and requires specific equipment, as well as dedicated laboratory and trained personnel; moreover, it is time-consuming, and requires labelling.

The aim of this thesis was to develop an organic electronic-based biosensor for the detection of biomarkers of MS to be used as a tool for routinary testing. In this chapter, the development of a NF-L biosensor, validated in plasma samples containing the target protein, is described. This platform is presented as a promising tool to overcome the above-mentioned limitations.

8.2. Gate functionalization and characterization

The proposed biosensor was fabricated using an electrochemical organic transistor architecture, exploiting the gate electrode as the sensing part of the device. The gate functionalization protocol was based on a variation of the functionalization strategy described in chapter 7. Following the same approach, the Au gate electrodes were incubated in a mixed biotin-OEG SAM solution. The use of this mixed SAM had a twofold intention: to immobilize the antibodies on the gate surface, using the biotin moieties exposed on the SAM layer, and to reduce the non-specific adsorption of plasma components, exploiting the antifouling properties of the SAM. In this regard, a final incubation step in a mixed solution of BSA-Tween 20 was done in order to increase the passivation of the gate electrode.

Prior to the electrical characterization, the immobilization of the antibody was monitored in real time using FO-SPR. Since the geometry of the FO resembles that of the Au wires employed during the experiments, the functionalization process was reproduced on FO and monitored optically. After the first step, i.e., the formation of the SAM layer on the Au surface, the FO were connected to the optical setup, and the functionalization process was continued while recording the signal. A representative optical redout, corresponding to the biotin-neutravidin conjugation and the consecutive binding of the anti-NF-L antibodies on the FO surface, is illustrated in Figure 8.1. After recording the baseline optical signal in PBS (green), the FO was immersed in a neutravidin solution (blue). As observed, the conjugation of neutravidin with the exposed biotin moieties at the SAM surface led to a significant change in the SPR signal. The FO was incubated with the neutravidin solution for 1 h, however, as it can be inferred from the plot, after approximately 30 minutes of incubation the SPR signal becomes stable. Therefore, in the further electrical measurements, the incubation time of the Au gate electrode with neutravidin was reduced to 30 minutes. After the incubation, the FO was washed using the previous PBS solution, in order to remove the unbound protein. This new baseline was then used to calculate the normalized change in the SPR response. Following, the buffer was changed by a fresh PBS solution, in order to avoid alterations in the SPR response due to changes in the RI of the buffer. The FO was then incubated with the specific anti-NF-L antibody (red), which led to a noticeable change in the SPR signal. Finally, the FO was washed again with PBS. The obtained SPR signal is represented as the shift in the resonance wavelength (λ_{SPR}), which was calibrated using sucrose calibration and, therefore, divided by the bulk sensitivity (S_B).

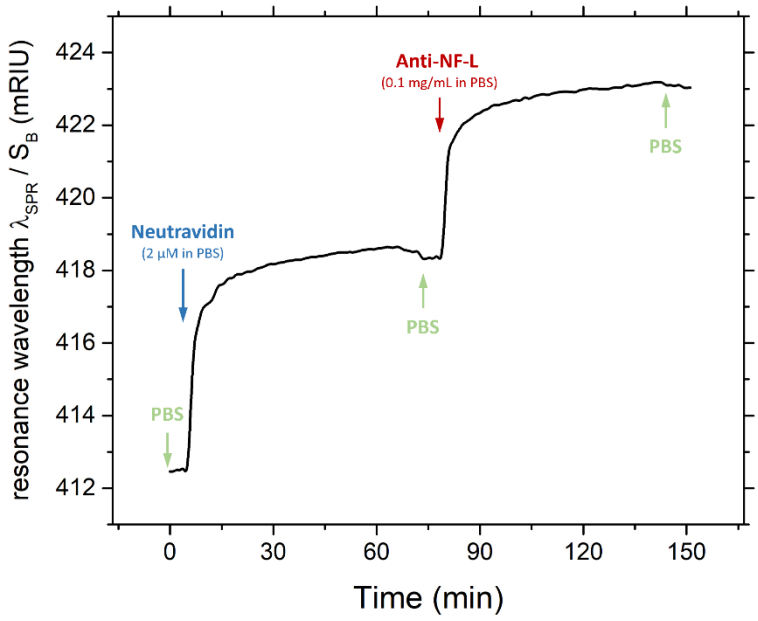

Figure 8.1. Optical signal corresponding to the successful immobilization of anti-NF-L antibodies on the Au FO surface via biotin-neutravidin conjugation.

From the obtained signal, the functionalization process can be quantitatively evaluated in terms of surface mass density and the number of attached biorecognition elements, using the Feijter's equation, described in chapter 7 (Eq. 7.1). The thickness of the layer was calculated from the shift in the resonance wavelength, using a simulated calibration curve[16]. The obtained results are shown in Table 8.1.

Table 8.1. Optical response of the sensor and the derived surface mass for the surface functionalization with neutravidin and anti-NF-L antibody. Data is presented as the mean ± SD of 3 independent experiments.

	Calibrated optical signal, $\Delta\lambda_{SPR}/S_B$ (mRIU)	**Surface mass density, Γ** (ng/cm^2)	**Number of molecules/cm^2**
Neutravidin	7.0 ± 0.9	389 ± 48	$3.9\times10^{13} \pm 4.8\times10^{12}$
Anti-NF-L	4.5 ± 0.2	252 ± 12	$1.0\times10^{12} \pm 4.8\times10^{10}$

The estimated values for neutravidin coupling are well in line with the values reported in similar studies, using SPR or quartz crystal microbalance[17,18]. As well, the resulting values for antibody immobilization are in perfect agreement with previous studies, indicating the formation of a densely-packed antibody layer[19–22].

After successfully demonstrating the antibody immobilization on the Au surface by FO SPR, the electrical performance of the fabricated transistors gated by the functionalized Au electrodes was assessed. The transistors were fabricated using the organic semiconductor DPP-DTT as channel material, that was deposited by spin-coating on FBK quartz substrates. First, the Au electrodes were electrically characterized in PBS, and the impact of the functionalization process was evaluated. Then, the device performance in a complex biological fluid was evaluated by using blood plasma as the electrolyte (plasma was diluted in PBS in a 1/50 ratio). The electrical characterization was performed by recording continuous transfer characteristics, until stabilization. As witnessed in Figure 8.2, the gate functionalization process led to a drastic decrease in the drain current, as well as a decrease in $g_{m,max}$ and a shift of V_{th} to more negative potentials. This behaviour was even more pronounced when, instead of a buffer, plasma was used as the electrolyte.

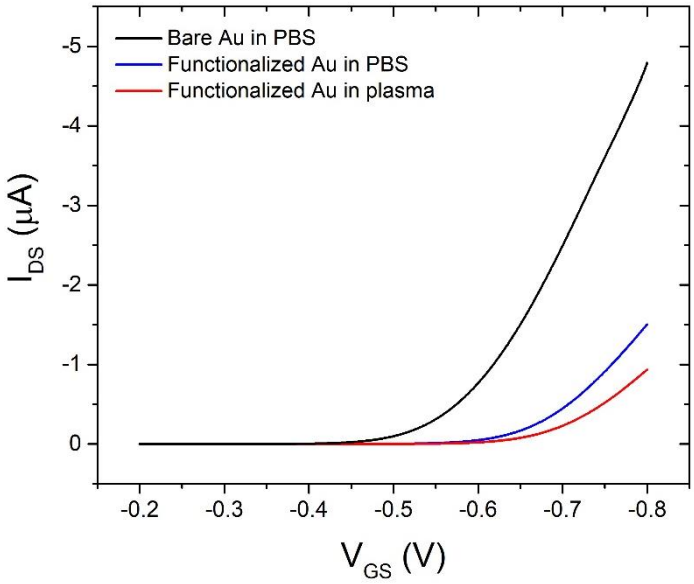

Figure 8.2. Transfer characteristics recorded before and after the Au functionalization. Black transfer curve represents the bare Au gate electrode recorded in PBS, while blue and red transfer curves correspond to the Au electrode after functionalization recorded in PBS or plasma, respectively.

In order to evaluate quantitatively the electrical performance of the transistors, several figures of merit, including $g_{m,max}$, V_{th}, and the I_{on}/I_{off} current ratio, were extracted from the transfer curves. The obtained results are summarized in Table 8.2. In accordance with the observations described earlier in this thesis, the gate functionalization led to a decrease in the drain current and in $g_{m,max}$, together with a shift of V_{th} towards more negative potentials. The former observation was even more marked when the device was exposed to plasma. In this case, no

significant change in $g_{m,max}$ was observed when compared to the functionalized electrode characterized in PBS. This is in total agreement with the results reported in chapter 5. Interestingly, no significant change in the I_{on}/I_{off} ratio was observed upon functionalization. In chapter 6, an increase in the I_{on}/I_{off} ratio was observed following the SAM formation, which was ascribed to a decrease in the I_{off}. In this case, a decrease in the I_{off} was observed as well, however, the concomitant decrease in I_{on} was more pronounced, balancing the I_{on}/I_{off} ratio. Similarly, in plasma, compared to the functionalized gate tested in PBS, the decrease in I_{on} was even bigger, while no changes were observed in I_{off}, leading to a decrease in the I_{on}/I_{off} ratio. Although a higher I_{on}/I_{off} ratio was reported in chapter 6 for devices characterized in plasma in comparison to PBS, both situations are difficult to compare, as different gate electrodes (bare Au and functionalized Au) and electrolytes (whole and diluted plasma) were employed.

Table 8.2. Electrical performance of the EGOT-based immunosensors before and after the gate functionalization. The results shown are the mean ± SD of 3 data sets.

	PBS		**Plasma**
	Bare Au	*Functionalized Au*	*Functionalized Au*
g_m (S)	$1.9\text{x}10^{-5} \pm 0.3\text{x}10^{-5}$	$9\text{x}10^{-6} \pm 3\text{x}10^{-6}$	$7\text{x}10^{-6} \pm 2\text{x}10^{-6}$
V_{th} (V)	-0.54 ± 0.06	-0.67 ± 0.02	-0.73 ± 0.01
I_{on}/I_{off}	$\sim 3\text{x}10^{4}$	$\sim 1.5\text{x}10^{4}$	$\sim 3\text{x}10^{3}$

In spite of this, after the gate functionalization, the transistors showed optimal electrical performance, even in such a complex fluid as it is blood plasma. Furthermore, the devices showed good stability in both, PBS and plasma, presenting a minimal variability of 4 and 3%, respectively.

8.3. Dose curve analysis

After successfully assessing the gate functionalization strategy and the device performance in a complex biological fluid, the biosensing capability of the transistors was tested. In a preliminary verification, dose curve experiments were performed in PBS, and, after obtaining satisfactory results, the experiments were repeated in plasma samples. The sensing experiments

were performed by recording transfer characteristics in the -0.2 to -0.8 V potential window, using PBS or plasma as electrolyte, spiked with increasing concentrations of NF-L, ranging from 50 pM to 10 nM. Note that plasma solutions were prepared using plasma samples from healthy controls that were diluted in PBS to a factor of 1/50. The typical response of the biosensor, depicted in Figure 8.3, was characterized by a continuous decrease in the drain current following increasing concentrations of the target protein. Interestingly, although different in magnitude, the response observed followed the same trend in both solutions tested, PBS and plasma, suggesting that the biosensor is capable of detecting the binding of NF-L proteins even in such a complex fluid as it is blood plasma.

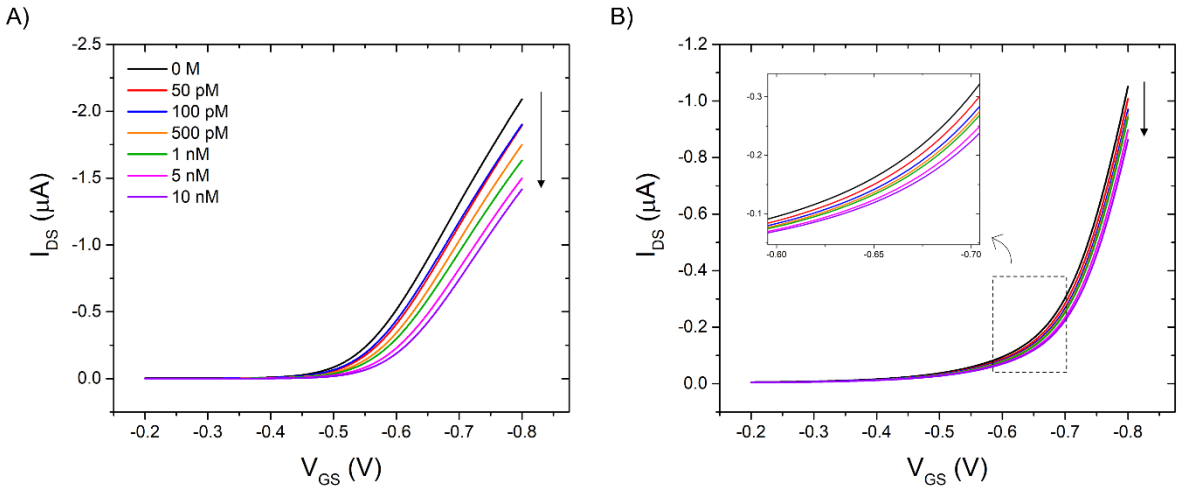

Figure 8.3. Transfer curves of the biosensor upon exposure to increasing concentrations of NF-L recorded in PBS (A) or plasma (B).

The response of the biosensor was quantitatively assessed, as previously described, by plotting $\Delta I/I_0$ as a function of [NF-L]. In line with previous reports, $\Delta I/I_0$ was calculated in the subthreshold regime, which was defined as $V_{GS} = V_{th} - 50\ mV$. The normalized response is depicted in Figure 8.4. As hinted by the transfer curves, the magnitude in the response of the biosensor exposed to plasma is lower than in PBS. Nevertheless, the capability of the biosensor to effectively discriminate NF-L in the concentration range tested is retained.

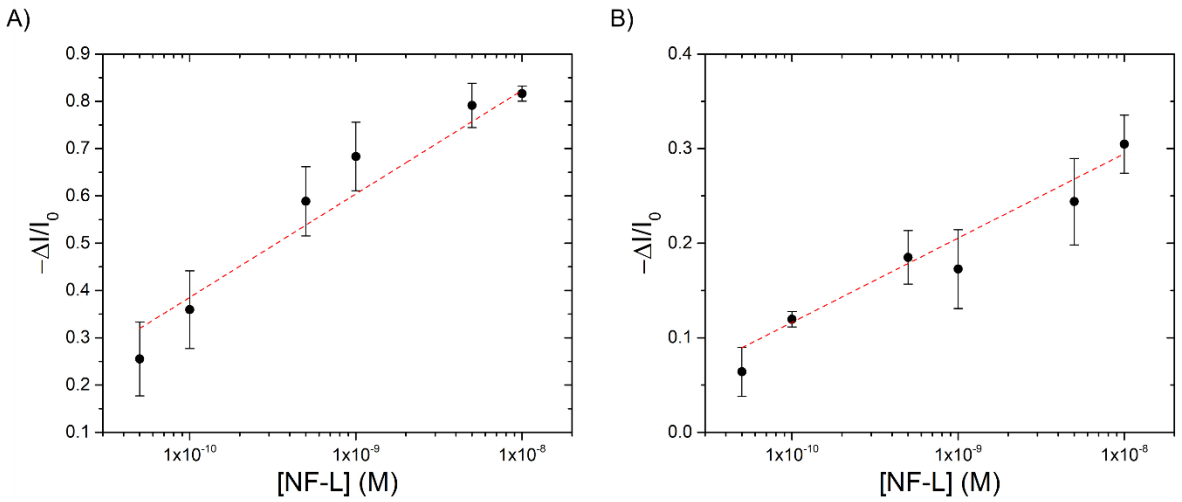

Figure 8.4. Biosensor dose curve, represented as $\Delta I/I_0$ vs Log[NF-L], in PBS (A) and plasma (B), fitted to a linear fit (red line). $\Delta I/I_0$ is determined at the subthreshold regime, calculated as $V_{GS} = V_{th} - 50\ mV$. Data is reported as the mean ± SE of 3 independent experiments.

The response of the device upon exposure to plasma solutions containing NF-L was further evaluated in terms of changes in transconductance and threshold voltage. The normalized results are presented in Figure 8.5. Specifically, as the concentration of the target protein increases, the transconductance decreases (panel A), while the threshold voltage shifts slightly to more negative values (panel B). Although the shift in V_{th} might be considered negligible, especially when if taking into account the error bars, the observed trend in g_m, similar to the signal $\Delta I/I_0$, and its magnitude, indicate that *gm* could be used as a complementary parameter for the evaluation of NF-L binding in plasma.

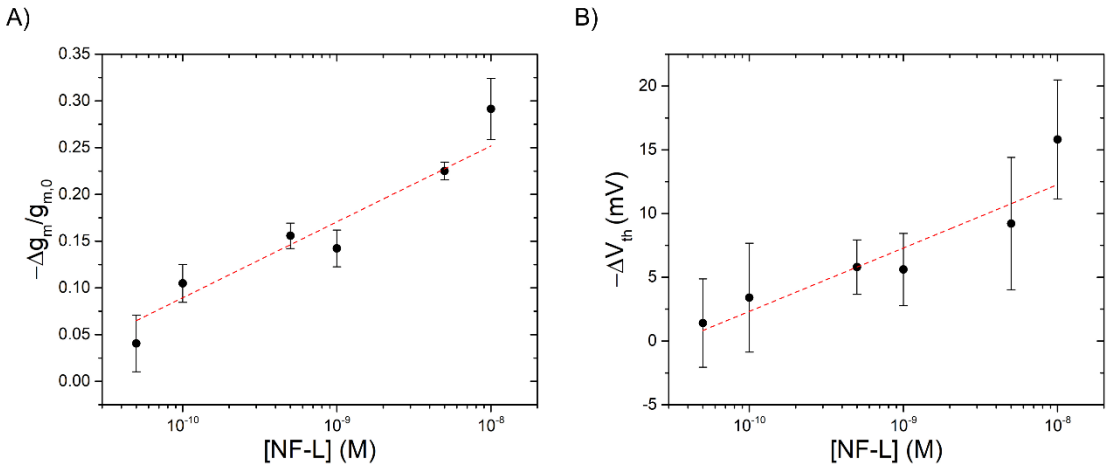

Figure 8.5. Normalized variation in g_m (A) and V_{th} (B) of the biosensor upon exposure to increasing [NF-L] in plasma. $\Delta g_m/g_{m,0}$ was calculated at the same V_{GS} as $\Delta I/I_0$. The results are shown as the mean ± SE of 3 independent experiments.

8.4. Evaluation of the biosensor selectivity in plasma

Once the successful operation of the biosensor in plasma was demonstrated, a set of control experiments was performed in order to evaluate whether the observed response of the biosensor in plasma resulted from the specific interactions between NF-L proteins and their corresponding antibody immobilized on the gate surface. In a first set of control experiments, the evaluation of the biosensor's selectivity was performed by exposing the biosensor, deprived of the recognition element, to plasma samples. In this approach, the dose curve experiments were repeated, using plasma samples spiked with NF-L, and gate electrodes functionalized as described, but lacking anti-NF-L antibodies. The results, shown in Figure 8.6 (panel A), are expressed as $\Delta I/I_0$, and compared to the response obtained in the presence of the specific recognition unit. As expected, no specific response was detected, and only minor variations were observed, as suggested by the nearly flat fitting curve. Although the highest concentration tested, i.e., [NF-L] = 10 nM, generated a considerable response, its meaning might be discarded, as such high concentration of NF-L is well above the pathological range in multiple sclerosis.

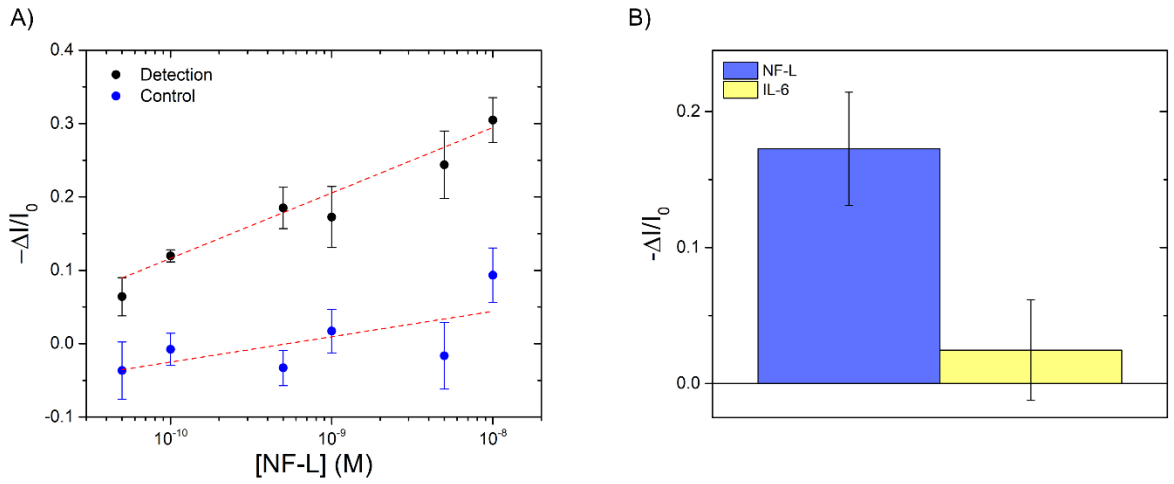

Figure 8.6. Evaluation of the sensitivity of the NF-L biosensor in plasma. A) Response of the biosensor to increasing concentrations of NF-L plasma in the presence (black) or absence (blue) of specific anti-NF-L antibodies at the gate surface. B) Response of the biosensor to the exposure of a plasma solution containing 1 nM IL-6 (yellow), compared to the specific NF-L response and the same concentration (blue). $\Delta I/I_0$ is determined at the subthreshold regime, calculated as $V_{GS} = V_{th} - 50\ mV$. Data is shown as the mean ± SE of 3 independent experiments. The red line represents a linear fit.

In a second round, control experiments were performed to evaluate the non-specific response of the biosensor to interfering proteins present in the sample. IL-6 is a well-known inflammatory mediator, highly expressed in response to environmental stress[23]. The dysregulation of IL-6 signalling, and regulation pathways has been associated with several pathologies, including diabetes, cancer, and atherosclerosis[24,25]. Moreover, increasing levels of IL-6 have been reported as well in multiple sclerosis[26,27]. Therefore, control experiments were performed to monitor the response of the biosensor to IL-6. In the described setup, the biosensors were exposed to plasma solutions containing a high concentration of IL-6, namely 1 nM. The response of the biosensor is shown in Figure 8.6 (panel B), compared to the specific response corresponding to NF-L. It is apparent that the resulting response is minimal, and might be even considered negligible when compared to the specific response obtained with NF-L. As mentioned previously in chapter 6, the IL-6 concentration used in these experiments is much higher than the concentration present at pathological levels. In addition, it has to be considered that IL-6 might have been already present in the initial plasma sample, increasing in this way the final concentration of IL-6 in the tested solution.

8.5. Conclusions

In conclusion, the successful development of an EGOT-based biosensor operated directly in plasma samples was demonstrated. For comparison, the performance and stability of the device was evaluated in buffer solutions and plasma samples, yielding satisfactory results in both scenarios. Furthermore, the biosensor proved to selectively detect NF-L in a buffer solution in a wide concentration range. Remarkably, upon the exposure of the biosensor to plasma samples containing NF-L, the capability to provide a specific response, triggered by the selective interaction between the target protein and its corresponding antibody, was retained. Moreover, the control experiments performed demonstrated the high selectivity of the system.

The obtained results demonstrate that the presented biosensor is capable of detecting NF-L in plasma samples spiked with the protein, providing a label-free and highly selective response, even in the presence of other potentially interfering molecules present in plasma. It is evident that further optimization of the device is required; a larger number of experiments should be conducted, the capability of the biosensor to measure *in vivo* produced NF-L has to be tested and, finally, the biosensor should be compared with other standard NF-L detection methods.

Nonetheless, the reported findings support the implementation of the NF-L biosensor as a promising accessible platform for clinical analysis in the MS pathology.

8.6. References

1. Hess, L. H. *et al.* Graphene Transistor Arrays for Recording Action Potentials from Electrogenic Cells. *Advanced Materials* **23**, 5045–5049 (2011).

2. Yao, C. *et al.* Organic Electrochemical Transistor Array for Recording Transepithelial Ion Transport of Human Airway Epithelial Cells. *Advanced Materials* **25**, 6575–6580 (2013).

3. Lingstedt, L. v. *et al.* Monitoring of Cell Layer Integrity with a Current-Driven Organic Electrochemical Transistor. *Adv Healthc Mater* **8**, 1900128 (2019).

4. Jimison, L. H. *et al.* Measurement of Barrier Tissue Integrity with an Organic Electrochemical Transistor. *Advanced Materials* **24**, 5919–5923 (2012).

5. Campana, A., Cramer, T., Simon, D. T., Berggren, M. & Biscarini, F. Electrocardiographic Recording with Conformable Organic Electrochemical Transistor Fabricated on Resorbable Bioscaffold. *Advanced Materials* **26**, 3874–3878 (2014).

6. Williamson, A. *et al.* Localized Neuron Stimulation with Organic Electrochemical Transistors on Delaminating Depth Probes. *Advanced Materials* **27**, 4405–4410 (2015).

7. Kyndiah, A. *et al.* Bioelectronic Recordings of Cardiomyocytes with Accumulation Mode Electrolyte Gated Organic Field Effect Transistors. *Biosens Bioelectron* **150**, 111844 (2020).

8. Spanu, A. *et al.* An organic transistor-based system for reference-less electrophysiological monitoring of excitable cells. *Sci Rep* **5**, 8807 (2015).

9. Bortolotti, C. A., Berto, M., Sensi, M., di Lauro, M. & Biscarini, F. Biosensing with Electrolyte Gated Organic Field Effect Transistors. in *Organic Bioelectronics for Life Science and Healthcare* vol. 56 71–96 (2019).

10. Torsi, L., Magliulo, M., Manoli, K. & Palazzo, G. Organic field-effect transistor sensors: a tutorial review. *Chem Soc Rev* **42**, 8612 (2013).

11. Luo, L. & Liu, Z. Recent progress in organic field-effect transistor-based chem/bio-sensors. *VIEW* **3**, 20200115 (2022).

12. Torricelli, F. *et al.* Electrolyte-gated transistors for enhanced performance bioelectronics. *Nature Reviews Methods Primers* **1**, 66 (2021).

13. Burtscher, B. *et al.* Sensing Inflammation Biomarkers with Electrolyte-Gated Organic Electronic Transistors. *Adv Healthc Mater* **10**, 2100955 (2021).

14. Sophocleous, M., Contat-Rodrigo, L., Garcia-Breijo, E. & Georgiou, J. Organic Electrochemical Transistors as an Emerging Platform for Bio-Sensing Applications: A Review. *IEEE Sens J* **21**, 3977–4006 (2021).

15. Simoa® Technology. Available at: https://www.quanterix.com/simoa-technology/ (Accessed: February 2023).

16. Hasler, R. *et al.* Field-Effect Transistor with a Plasmonic Fiber Optic Gate Electrode as a Multivariable Biosensor Device. *ACS Sens* **7**, 504–512 (2022).

17. Cui, X. *et al.* Layer-by-layer assembly of multilayer films composed of avidin and biotin-labeled antibody for immunosensing. *Biosens Bioelectron* **18**, 59–67 (2003).

18. MacDonald, H. *et al.* Influence of Aptamer Surface Coverage on Small Target Recognition: A SPR and QCM-D Comparative Study. *The Journal of Physical Chemistry C* **123**, 13561–13568 (2019).

19. Toma, M. & Tawa, K. Polydopamine Thin Films as Protein Linker Layer for Sensitive Detection of Interleukin-6 by Surface Plasmon Enhanced Fluorescence Spectroscopy. *ACS Appl Mater Interfaces* **8**, 22032–22038 (2016).

20. Huang, C.-J., Dostalek, J., Sessitsch, A. & Knoll, W. Long-Range Surface Plasmon-Enhanced Fluorescence Spectroscopy Biosensor for Ultrasensitive Detection of *E. coli* O157:H7. *Anal Chem* **83**, 674–677 (2011).

21. Wang, Y. *et al.* Biosensor based on hydrogel optical waveguide spectroscopy. *Biosens Bioelectron* **25**, 1663–1668 (2010).

22. Macchia, E. *et al.* Single-molecule detection with a millimetre-sized transistor. *Nat Commun* **9**, 3223 (2018).

23. Tanaka, T., Narazaki, M. & Kishimoto, T. IL-6 in Inflammation, Immunity, and Disease. *Cold Spring Harb Perspect Biol* **6**, a016295–a016295 (2014).

24. Villar-Fincheira, P. *et al.* Role of Interleukin-6 in Vascular Health and Disease. *Front Mol Biosci* **8**, (2021).

25. Hirano, T. IL-6 in inflammation, autoimmunity and cancer. *Int Immunol* **33**, 127–148 (2021).

26. Nasi, M. *et al.* Increased plasma levels of mitochondrial DNA and pro-inflammatory cytokines in patients with progressive multiple sclerosis. *J Neuroimmunol* **338**, 577107 (2020).

27. Magliozzi, R. *et al.* Inflammatory intrathecal profiles and cortical damage in multiple sclerosis. *Ann Neurol* **83**, 739–755 (2018).

Chapter 9.

Summary and conclusions

The main purpose of this thesis was to develop an organic electronic-based biosensor for the detection of potential biomarkers of multiple sclerosis (MS) in plasma. To date, no ideal marker of MS has been identified, therefore, in this work, potential molecular MS biomarkers were investigated. The ideal biomarker should be highly sensitive and specific, as well as easily measurable and accessible. However, the current biomarkers proposed for MS do not meet most of these criteria, as they are not specific for MS, the sensitivity is variable, the detection methods present several limitations, and their accessibility is limited, as the preferred sample for analysis is cerebrospinal fluid.

In the approach described in this work, a fast and sensitive detection of MS biomarkers in plasma samples is proposed. The high sensitivity is achieved by developing electrolyte-gated organic transistor (EGOT)-based biosensor, endowed with biorecognition capacity towards the target molecule. The biosensors are easy to operate and provide a fast response. In addition, the measurement is performed directly in plasma, allowing the implementation of the biosensor for routinary testing.

In particular, EGOT biosensors were developed for two candidate MS biomarkers: neurofilament light chain (NF-L) and mitochondrial DNA (mtDNA). During the fabrication process, different EGOT architectures and semiconducting materials were investigated. Then, the Au gate electrode was used as the sensing part of the device, and several functionalization strategies were exploited in order to optimize the biosensors.

First, an EGOT-based biosensor was developed for detection of NF-L. In this approach, specific anti-NF-L antibodies were immobilized in the gate surface with a potentially uniform orientation, increasing the probability of binding events. The recognition capability of the

biosensor was tested in buffer solutions containing increasing concentrations of the target protein, obtaining successful results. Further investigations of the binding process allowed the determination of the limit of detection, with an estimated value as low as 30 fM.

In a similar approach, an EGOT-based biosensor was developed for monitoring the hybridization of mtDNA. The functionalization strategy, together with the hybridization assay, were investigated in real time using optical techniques. Further, the device was successfully tested as biosensor in an electrical setup. The resulting binding kinetics from both, optical and electrical experiments, hinted to the fact that the binding is not dependent on the transduction mechanisms. Moreover, no significant differences were observed in kinetics, indicating that the electrical setup provides good response, similar to the one obtained in the optical measurements, in a label-free setup.

Recently, EGOT-based sensors have experienced a drastic growth, and biosensors for biological analytes, environmentally relevant molecules, or chemicals, have been reported. However, the application of these biosensors in complex, clinical samples, such as plasma, is still very limited. To overcome this limitation, an important part of this thesis was focused on the development of an EGOT device to be operated as biosensor in plasma samples. The fabricated biosensor presented good electrical performance, even in plasma. Then, the developed device was tested as biosensor for NF-L, in a buffer solution and in plasma. The results obtained proved that the biosensor is capable of selectively detecting NF-L in a wide range of concentrations, even in a fluid as complex as plasma.

In summary, this work demonstrated the potential of organic electronics for biosensing applications in the clinical field. It is notable that further optimization of the biosensors is required in order to generate a platform comparable to the current gold standards. In particular, the sensitivity of the biosensors should be improved, especially when operating the devices in complex biological samples. However, the presented data supports the implementation of EGOT-based biosensor as a promising platform for the monitoring of MS. The characteristics of the proposed biosensors, such as fast response, low cost, easy to operate, and disposability, among others, make it a promising tool for the routinary testing of MS patients.

List of abbreviations

AD	Alzheimer’s disease
AFM	Atomic force microscopy
BSA	Bovine serum albumin
C-DNA	Complementary mtDNA probe
CE	Counter electrode
CIS	Clinically isolated syndrome
CNS	Central nervous system
COVID-19	Coronavirus disease 19
CSF	Cerebrospinal fluid
CV	Cyclic voltammetry
DIS	Dissemination in space
DIT	Dissemination in time
ECL	Electrochemiluminescence assay
EDL	Electrical double layer
EGOFET	Electrolyte-gated organic field-effect transistor
EGOT	Electrolyte-gated organic transistor
ELISA	Enzyme-linked immunosorbent assay
Fc	Fragment crystallizable region
FO	Fiber optic
GAB	Guggenheim-Anderson-De Boer adsorption model
g_m	Transconductance
I	Current
IDE	Interdigitated electrode
Ig	Immunoglobulin

IL	Interleukin
L-DNA	Labelled mtDNA probe
LOD	Limit of detection
MRI	Magnetic resonance imaging
MS	Multiple sclerosis
mtDNA	Mitochondrial DNA
MUA	Mercaptoundecanoic acid
NC-DNA	Non-complementary mtDNA probe
NF	Neurofilament
NF-H	Neurofilament heavy chain
NF-L	Neurofilament light chain
NF-M	Neurofilament medium chain
OCB	Oligoclonal bands
OECT	Organic electrochemical transistor
OEG	Oligoethylene glycol
OFET	Organic field-effect transistor
OLED	Organic light-emitting diode
OPV	Organic photovoltaic cell
OSC	Organic semiconductor
P-DNA	Capturing mtDNA probe
PB	Phosphate buffer
PBS	Phosphate buffer saline
PBS-T	Phosphate buffer saline + Tween 20
PCR	Polymerase chain reaction
PD	Parkinson’s disease
PPMS	Primary progressive multiple sclerosis

RE	Reference electrode
RI	Refractive index
RIS	Radiologically isolated syndrome
RRMS	Relapsing remitting multiple sclerosis
SAM	Self-assembled monolayer
SD	Standard deviation
SE	Standard error
SEM	Scanning electron microscopy
SiMoA	Single molecule array
SiMoT	Single molecule transistor
SP	Surface plasmon
SPFS	Surface plasmon-enhanced fluorescent spectroscopy
SPMS	Secondary progressive multiple sclerosis
SPR	Surface plasmon resonance
SVA	Solvent vapour annealing
TP	Test pattern
V	Voltage
V_{th}	Threshold voltage
WE	Working electrode

List of figures

List of tables